

NG4-10113

Space Programs Summary No. 37-23, Volume III

for the period July 1, 1963 to August 31, 1963

The Deep Space Instrumentation Facility

OTS PRICE

XEROX	\$	<u>7.60</u>
MICROFILM	\$	<u>2.27</u>

jpl

JET PROPULSION LABORATORY
CALIFORNIA INSTITUTE OF TECHNOLOGY
PASADENA, CALIFORNIA

September 30, 1963

Space Programs Summary No. 37-23, Volume III

for the period July 1, 1963 to August 31, 1963

The Deep Space Instrumentation Facility

JET PROPULSION LABORATORY
CALIFORNIA INSTITUTE OF TECHNOLOGY
PASADENA, CALIFORNIA

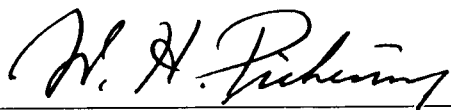
September 30, 1963

Preface

The *Space Programs Summary* is a six volume, bimonthly publication designed to report on JPL space exploration programs, and related supporting research and advanced development projects. The subtitles of all volumes of the *Space Programs Summary* are:

- Vol. I. The Lunar Program (Confidential)
- Vol. II. The Planetary-Interplanetary Program (Confidential)
- Vol. III. The Deep Space Instrumentation Facility (Unclassified)
- Vol. IV. Supporting Research and Advanced Development (Unclassified)
- Vol. V. Supporting Research and Advanced Development (Confidential)
- Vol. VI. Space Exploration Programs and Space Sciences (Unclassified)

The *Space Programs Summary*, Volume VI is an unclassified digest of appropriate material from Volumes I through V, plus the space science instrumentation studies of the JPL Space Sciences Division.



W. H. Pickering, Director
Jet Propulsion Laboratory

Space Programs Summary No. 37-23, Volume III

Copyright © 1963, Jet Propulsion Laboratory, California Institute of Technology

Prepared under Contract No. NAS 7-100, National Aeronautics & Space Administration

Contents

I. Résumé	1
II. Goldstone Operations	5
III. Engineering Development	8
A. L-Band Acquisition Aid	8
B. Mark I Ranging Subsystem	11
C. GSDS Telemetry Data Encoder	14
D. Computer Controlled Antenna Pointing System	17
E. AAS Wind Data Gathering System	20
F. High-Power Test Laboratory	20
G. Systems Engineering	22
H. Computer Programs	23
References	26
IV. Research and Development	28
A. Ground Antennas	28
B. Planetary Radar Project	38
C. Lunar Radar Project	51
D. Ranging System Development	55
E. S-Band Implementation for DSIF	58
References	61
V. Advanced Antenna System	62
A. Synopsis	62
B. Supporting Studies	62
References	73

I. Résumé

The DSIF is a precision tracking and data acquisition network which is designed to track, command, and receive data from deep space probes. It utilizes large antennas, low-noise phase-lock receiving systems, and high-power transmitters at stations positioned approximately 120 deg around the Earth. Its policy is to continuously conduct research and development of new components and systems and to engineer them into the DSIF so as to continually maintain a state-of-the-art capability.

Goldstone operations. Equipment installation and tests at both Pioneer and Echo have been conducted in preparation for *Ranger 6*. A hydromechanical building is under construction at Pioneer as is a stores building at Echo. Core sample drillings and topographic surveys have been made at the Mars site in preparation for the erection of the 210-ft Advanced Antenna System.

Engineering development. An L-band acquisition aid antenna has been tested at Woomera. This antenna consists of four helices, in a simultaneous lobing configuration, has a gain of 18 db at 960 Mc, and has a beamwidth of 22 deg. Acquisition tests were made using an aircraft to simulate a spacecraft with the acquisition antenna

mounted in two locations: on the rim of the 85-ft antenna and at the end point of the quadripod. Acquisition was always satisfactory at elevations of 10 deg or higher, but was not certain at elevations from 10 to 5 deg. The rim location appears to be better than the quadripod mount. Ground reflections seriously affect the S-curves but are considered to be usable at 10-deg elevation or higher.

Construction of the prototype model of the Mark I ranging subsystem is almost completed. A program unit which controls the sequential operation of the ranging subsystem and an acquisition unit which completes the acquisition of a given component of the received ranging code have been designed. The Mark I subsystem provides the capability of ranging on passive satellites or "turn-around" transponders to a distance of 800,000 km.

A telemetry data encoder, which will be a general purpose instrument for use on all projects, is under development for use at all DSIF Stations. As planned, it will be capable of accepting either parallel or serial data of variable word lengths up to 5,000 bits/sec and of providing coded wide-band data outputs at 600, 1200, 2400, or 4800 bits/sec plus either 30- or 50-bit/sec 5-bit parallel teletype signals. Error detecting/correcting codes will be used.

Automatically driving an antenna from precomputed drive tapes has the advantages of rapid acquisition, freedom from dependence of signal strength, and the use of more sensitive listening feeds. A study is being made of a system which will use a small general purpose computer to provide servo drive voltages which have been generated from interpolations between discrete computed ephemeris data or from a sidereal clock. Position and rate offsets and angle presets will be available.

The wind data recording system at the Advanced Antenna (Mars) site is about 75% checked out. The tape recorder has been modified to a bit density of 556 bits/in.; the IBM 7090 computer program has been extensively modified, the drag spheres have been calibrated, and plans have been made to make wind tunnel tests of the 8-cps resonance. Some analog wind force data has been recorded.

The high-power test laboratory has been used to test S-band feeds at high power to determine the increase in noise temperature in a parametric and maser amplifier low-noise system during diplexing at 10 kw of power, and to evaluate high-power S-band klystrons. No arc occurred in the feeds when up to 14 kw of power was used. The Eimac klystron was recommended as being the most versatile of the klystrons which were tested.

A *Fortran II* program has been written for an IBM 1620 computer to compute the angular hour angle and declination velocity and acceleration of a polar mount antenna as it tracks an Earth satellite. Inputs consist of Earth constants, satellite trajectory constants, station latitude and time.

The SDS 920 computer at Goldstone is being used to compare predicted with actual tracking data and to compute doppler variance for each DSIF Station in order to maintain a continuous check on the station equipment capabilities. Direct rectilinear plots are made from teletyped data.

In order to reduce the time consuming task of manually producing the originals of the stereographic station projections, a *Fortran* program has been written for the SDS 920 computer to generate the *xy* coordinates of the hour angle-declination and the azimuth-elevation intersections for an arbitrary station location.

Ground antennas. In order to check the boresight and gain calibrations of large antennas, a method of using

radio stars has been developed. The antenna is set in a fixed position and a radio star is allowed to drift through the beam. Using automatic noise calibration methods with both ambient and liquid nitrogen cooled loads and a Dicke radiometer, the resultant signals are synchronously chopped with a square wave audio frequency and synchronously detected. Two computer programs are used to reduce the data.

A program to calibrate the precision 30-ft antenna at the Venus site using radio-astronomical techniques makes use of an X-band radiometer with a resolution of 0.5 to 1°K in a system temperature of about 700°K. Special attention has been given to supplying the IF amplifiers with stable plate and filament voltages to reduce gain fluctuations.

Two computer programs are being used to evaluate the scalar far field radiation pattern integral and the aperture efficiency of paraboloid reflector antennas. Actual measurements on the 30-ft antenna at X-band compare favorably with the computed results when blockage by the subreflector and the quadripod is included.

Planetary radar. Using a 100-kw monostatic radar system with a system noise temperature of 37°K, radar measurements were made of Mars during the period January 31 to March 2, 1963. A frequency spectrogram, representing 65 hr of signal integration, indicates that most of the power was reflected from a disc 350 mi wide on the surface of Mars. Using total power measurements a radar brightness map of Mars was made and compared with visual maps. The region of Systis Major appears light to radar but dark to visual observations.

The 100-kw transmitter protective circuit was improved by reducing the output impedance and high-frequency response of the crowbar logic chassis, by adding a 60- and 400-cps filter to the crowbar input, by rerouting the output of the current probe directly to the input of the crowbar logic chassis, by adding shielded wires and by shielding the complete crowbar logic chassis.

A set of high-voltage rectifier tubes from a second manufacturer had no internal or external arcs during a 3½-hr testing period at greater than full load. Attenuation measurements of a waveguide switch at high power confirmed similar measurements made in the laboratory with a low power oscillator.

The exciter for the 100-kw transmitter has been rebuilt to incorporate low leakage modules, cold plate water

cooling, more reliable power supplies and improved metering, protective and data readout circuits. The 3-db bandwidth is 6 Mc and the rms phase deviation at 2388 Mc in a 5-cycle loop is 2.7 deg (both receiver and exciter).

After installation of the "front end" of the Mod IV planetary radar receiver in the antenna feed cone, the AGC performance of the synchronous receiver was measured. Although the AGC operates only on the second mixer and the 455-kc IF amplifier of each channel, the output level was held to within 3 db for inputs from -160 to -87 dbm. A leakage at 30 Mc from the VTVM monitor lead was found by the AM spectrum analysis equipment and eliminated by filtering.

The total time delays in the transmitter and receiver of a ranging system amount to a ranging error of about 2500 mi and these delays must be precisely determined before the actual range can be measured. Due to system drifts it is generally desirable to do this as often as possible and as close to the measurement as possible. For this purpose a phase coherent 30-Mc monitor system has been added to the ranging system. The 30-Mc monitor receives its input at the face of the antenna and feeds its input directly into the receiver during the transmit cycle. A second set of ranging equipment measures the time delays. The monitor can also be used to check the transmitted spectrum.

The new water rotary joint design was dynamically tested at JPL and, after some slight modifications, it operated for an equivalent of 20 yr of life without leakage. It has been installed on the 85-ft antenna at Venus where further tests will be conducted.

Lunar radar. A Lunar Radar Project with objectives similar to the Planetary Radar Project is being planned. Because of the relatively short distance to the Moon and the small doppler changes, neither the bistatic or monostatic planetary radar systems can be used. However, by using a small auxiliary antenna, shielded by a "tunnel" and mounted at the quadripod apex, it appears possible to obtain sufficient signal-to-noise ratio to use an electronically switched system. The use of the auxiliary antenna depends upon the isolation between the antenna used for receiving and the 85-ft antenna used for transmitting. An isolation of 90 db has been measured. A calculated analysis of the system has been made showing optimum signal-to-noise ratios and transmitter powers for various degrees of isolation and system noise temperatures.

Ranging system development. Recent data on the ability to key off a transmitter to a level below the receiver threshold in an X-band monostatic radar has confirmed the extrapolation of previous data. Leakage between the signal source and the receiver prevents making measurements beyond the present 140-db capability until a very low-noise narrow bandwidth receiver is available. A synchronous sideband detector is being analyzed for its capability to prevent receiver locks on sidebands.

A keyer control unit for a monostatic radar has been developed which automatically switches the receiver on and the transmitter off, and vice versa, in response to a signal which is dependent upon the estimated or actual range. It also provides a variable delay signal to the special anti-sideband locking device in the receiver. The laboratory model of the delay unit generates phase shifts up to 180 deg by utilizing a counter to give selectable delays from 0 to 25.6 msec in 50- μ sec steps.

S-band implementation for DSIF. Traveling wave masers with closed-cycle helium refrigerators will be used in the DSIF at S-band. This maser uses a comb structure made up of active ruby material and passive ferrite material, a permanent magnet and trim coil kept at a constant temperature for stabilization purposes, and a pretuned 12.7-Gc Varian VA 246 klystron pump. The microwave head uses gold plated stainless steel for high electrical and low thermal conductivity. Its noise contribution will be 3 to 4°K. Standard receiver components will be used in the monitor receiver.

An S-band acquisition aid antenna is being developed for use with the 85-ft antennas to facilitate early acquisition of a spacecraft whose trajectory is unknown or uncertain. The antenna will be a multimode single horn with simultaneous lobing similar to the feed horn used with the 85-ft cassegrain system. It will be mounted with its aperture near the surface of the 85-ft antenna approximately half-way between the rim and the center and will utilize a complete three-channel receiver system, separate from the main antenna receiver system, so as to minimize the difficulties in transferring control from the acquisition aid antenna to the 85-ft antenna.

Advanced Antenna System. The Advanced Antenna System will be a 210-ft fully steerable paraboloid with the first one to be constructed at Goldstone, California. Engineering design on all phases is underway at the contractor, Rohr Corporation, and at several subcontractors. Design and engineering of site facilities, utilities, roads, and power equipment is being completed.

The computer program (RMS), which was developed to calculate the rms error in mean path length of a ray reflected from an imperfect reflector, shows that displacement of the apparent feed in a direction parallel to the axis of revolution yields greater errors than displacements perpendicular to the axis. Because of this the program is being modified to calculate a rms of half the path length errors as seen from the apparent feed.

The STAIR computer program which was developed to calculate joint deflections and bar stresses, in an antenna structure, caused by wind loads parallel and at right angles to the elevation axis has been modified to include wind loads in any direction.

The computer program developed to analyze hydrostatic bearings has been revised to increase the number of iterations from 300 to 1,000 and to include a term representing the velocity of the bearing along the runner.

The revised program is being used in the design of the 210-ft antenna. Several approaches are being tried to simplify the calculation of deflections of the runner on an elastic foundation. Good correlation has been obtained in the vicinity of the load between calculations made by Biot and the JPL-Franklin Institute computer program.

The techniques for analyzing the dynamics of large antennas are continually being improved. The dynamics of a large antenna are important to the design of the servo system and the structural configuration. The structure must be stiff enough to maintain accuracy in operational winds from any direction and to have the lowest natural resonant frequency compatible with the required pointing accuracy. It also must be reasonably economical. For the purposes of analysis the structure is represented by a lumped mass system for the pedestal, alidade, and drives, and by generalized masses and stiffnesses for all parts that move in elevation. By taking advantage of symmetry the labor of making the calculations can be simplified.

II. Goldstone Operations

Preparation for *Ranger 6* is continuing at Goldstone. All systems which will be involved in this *Ranger* series are being thoroughly inspected, modified, and repaired as required. Updating of equipment and training of personnel on new procedures in preparation for installation and operation has first priority.

1. Equipment

a. Echo site. The precision doppler bias loop response tests have been completed. The telemetry-to-teletype encoder has been installed and checked out. The *Ranger 6* decommutator equipment is being installed, and personnel from the DSIF overseas stations are being trained in its use.

Checkout of the new digital instrumentation system, including a new control panel, is nearing completion. DSIF personnel from Woomera and Johannesburg have received instruction in this new system. The *Ranger* data system was checked out and shipped to the overseas sites.

The transmitter group completed all modifications to the L-band system. Work continued on the transmitter L- and S-band exciter system for Woomera, Johannesburg, and Echo. The installation should be operational at Echo in early September. A testing program of reduced transmitter power was conducted in preparation for the *Ranger* shots. Under reduced power, the transmitter was tested for operating stability in an unmodulated condition at power levels under 200 w. The results obtained indicate a stable performance.

Control panels UD30-1 and UD70 for the Varian 7010B transmitter were modified and sent to Woomera. Modification kits for the parametric amplifier in the receiver system were sent to Woomera and Johannesburg.

Installation of the 50-w transmitter began on August 1, with the completion date tentatively set for September 1. This transmitter is backup for the Goldstone Duplicate Standard transmitter for *Ranger* Block III.

The coaxial line installation on the Echo antenna is being updated by the replacement of existing critical RG9 lines with a more stable semi-flexible coaxial cable. The lines are being rerouted and resecured to the structure where necessary. All test lines have been recalibrated. Defective cables and connectors are being replaced. The 3/8-in. rigid transmitter line installation has been modified to include a coaxial switch for use with the 50-w transmitter, and a double stub tuner has been included in the line for improved transmitter operation.

b. Pioneer site. Data equipment racks are being rewired to conform to Goldstone Duplicate Standard. The digital comparator was moved to the Echo site for updating, modification and checkout.

Preliminary work on the installation of the S-band transmitter, including a new hydromechanical building is in progress. Completion of the transmitter installation will provide the Pioneer site with both a receive and transmit capability. Data and instrumentation equipment are being modified to provide service for this dual capability.

c. Venus site. Equipment, previously housed in trailers, has been relocated and installed in the new control building. New hard surface road, permanent buildings, and improved communications facilities have been completed.

Gain measurements of the 85-ft antenna have been made using the Tiefert Peak collimation tower. Pattern measurements have been made using the 30-ft antenna and the Tiefert Peak collimation tower. The 30-ft antenna has been modified to operate in the slave mode in preparation for optical and radio star tracks.

d. Mars site. The Advanced Antenna System Program is progressing. Core sample drillings to a depth of 100 ft have been made for analysis in preparation for antenna foundation construction. Topographic surveys of the site have been completed for use by the architects and engineers. A site survey was conducted for a location of the time-lapse camera which will be used to record the construction of the antenna. A preliminary interval of 60 sec has been set for the regular sequence with an adjustable telephoto lens arrangement and interval-adjust for specific item or area recording.

2. Net Integration Tests

Five net integration tests are scheduled to begin October 15 and run through December 1. The prepara-

tion for these tests has included a complete in-house check of equipment. Along with this, JPL/RCA compatibility tests have been conducted on the video equipment.

3. Canberra-Madrid Project

Goldstone is providing preliminary logistics, refinement, and training support to the Canberra-Madrid Projects. Currently, this involves equipment refinement and documentation, and contractual purchase of some equipment. Equipment is received at Goldstone to be checked and then forwarded overseas. Spare parts are documented, ordered, and handled in the same manner as assemblies and subsystems. Training of some Canberra personnel is scheduled to begin during the month of September.

4. Building Construction

Two buildings are being erected: a hydromechanical building (Fig. 1) at the Pioneer site and a stores building (Fig. 2) at the Echo site. The floor in the hydromechanical building has been poured and construction is progressing with completion scheduled for October 1. The walls are up and the roof is in place on the stores building at Echo.

The control building at Pioneer is being repainted inside, new floor tile is being laid, and equipment is ready for reinstallation.

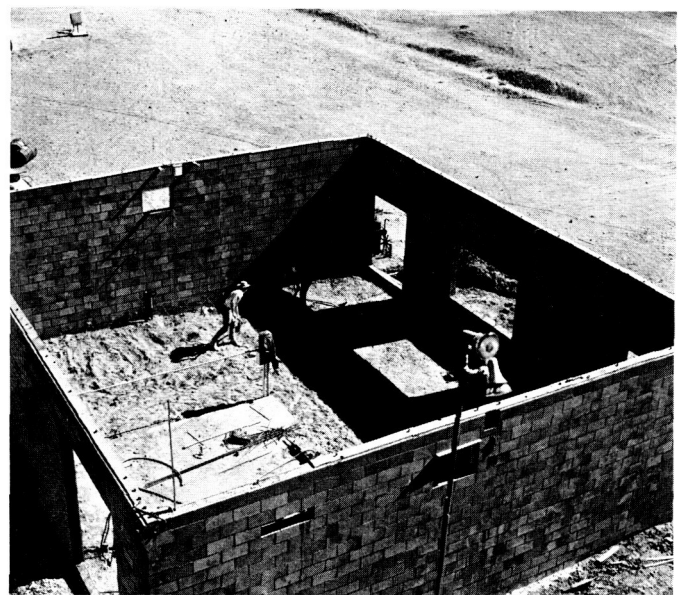


Fig. 1. Hydromechanical building at Pioneer site

The 85-ft antenna at Venus was tested with a sample of the resurface holding clips. New clips were ordered as a result of the test, and resurfacing has been completed. Fig. 3 illustrates the test surfacing installation.



Fig. 2. Stores building at Echo site

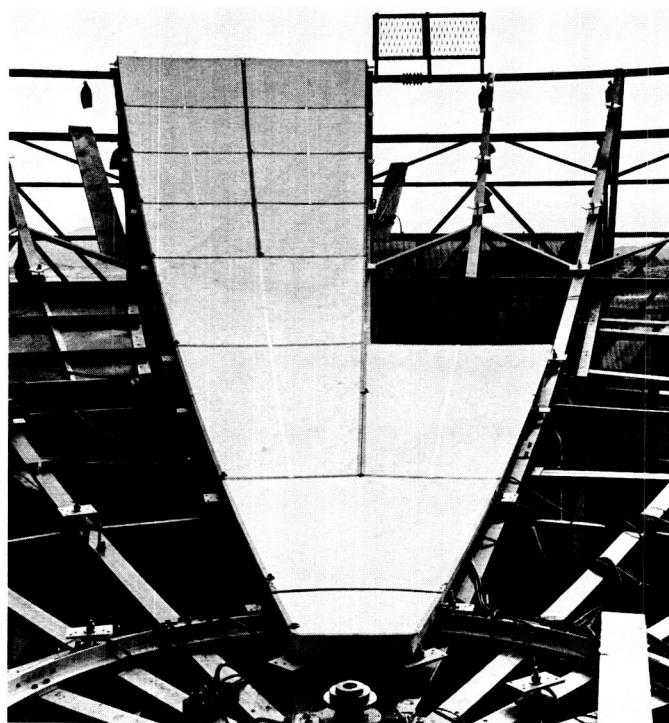


Fig. 3. Test surfacing installation at Venus site

III. Engineering Development

A. L-Band Acquisition Aid

1. General

The Woomera DSIF Station has carried out a program, under the direction of the Australian station manager, of evaluating the existing L-band acquisition aid antenna. The L-band acquisition aid at the Woomera DSIF consists of an array of four helices connected in a monopulse configuration. It is carried on the 85-ft diameter dish structure, and coaxial relays are used to select the signals (which are either from the dish or from the acquisition aid) fed to the phase-lock-loop three-channel receiver. Performance specifications as supplied in the manufacturer's handbook are as follows:

Frequency, 960 Mc

Gain, 18 db

Half power beamwidth, 22 deg

Sidelobe level, -12 db

Difference channel null, 30 db

Polarization, right circular

Ellipticity, 2 db

VSWR (comparator outputs), 1.5 to 1

Total weight, 50 lb

The main advantages of this type of acquisition aid lie in its simplicity and low cost. The disadvantages are the limitation in angular rate capability to that of the 85-ft diameter dish structure and the multipath or ground reflection problem.

The configuration of the acquisition system is shown in Fig. 1.

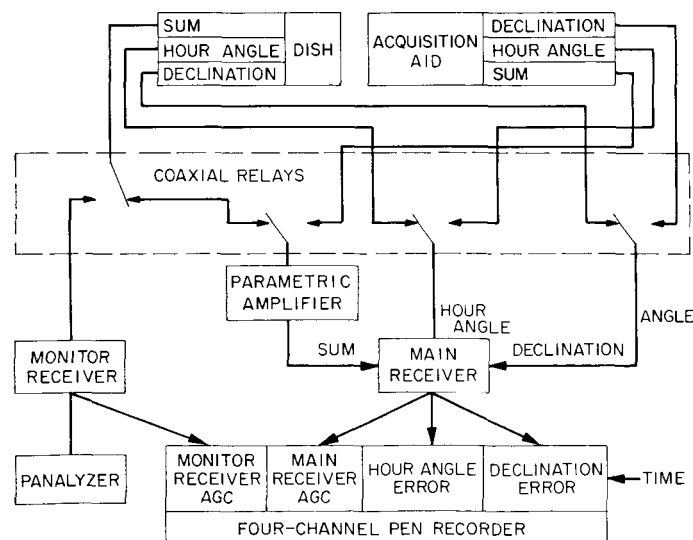


Fig. 1. Block diagram of acquisition system

2. Spacecraft Behavior

Launches from Cape Canaveral on lunar or planetary missions involve spacecraft that rise on Woomera's western horizon over an azimuth range from 220 to 300 deg. There are restricted zones in which the antenna does not have coverage down to the horizon. The elevation rate for such spacecraft can vary from almost 0 to 0.1 deg/sec. Power levels are such that signal strength through the dish main beam is about -100 dbm.

As the spacecraft recedes into space the effect of the Earth's rotation becomes increasingly significant and, eventually, the direction of motion, as observed by the station, reverses; ultimately, the spacecraft sets on the western horizon at a declination determined by the particular mission.

3. Location

It is possible to locate the acquisition aid at the quadri-pod tip looking outward from the dish or at the dish rim (Fig. 2). Both locations have the disadvantage that, as the antenna angle is changed, the position of the phase centre of the acquisition aid moves with respect to the ground in a fairly complex manner because of the hour angle-declination axes system employed. The quad tip location has the additional disadvantage that mutual coupling between the acquisition aid and the dish can

be troublesome. The dish rim location has the disadvantage that its height about the ground will change considerably for any given elevation less than, say, 20 deg with change in azimuth, again a feature of the system of axes. Thus, the dish rim location will be at the bottom of the dish for some azimuths, at intermediate positions for some, and at the top of the dish for others.

An important factor affecting choice of location is the ease with which the acquisition aid can be connected into the three-channel phase-lock-loop receiver. This can be easily accomplished by locating the coaxial relays in the drum assembly which houses the rat races for the tracking feed at the quad tip. By providing three low-loss coaxial lines from the dish rim to the quad tip, the acquisition aid can be located either at the quad tip or at the dish rim without changing the configuration of the associated hardware.

4. Boresight Measurements

The regular DSIF boresight tower of 3-deg elevation was not usable for checkout because multiple lock points and severe cross talk make it impossible to establish whether the acquisition aid is functioning properly. To achieve greater elevation angles the 80-ft high "Cherry Picker" truck stationed about 180 ft from the dish proved to be adequate. However, the close location introduced rather complicated geometric problems in the reduction

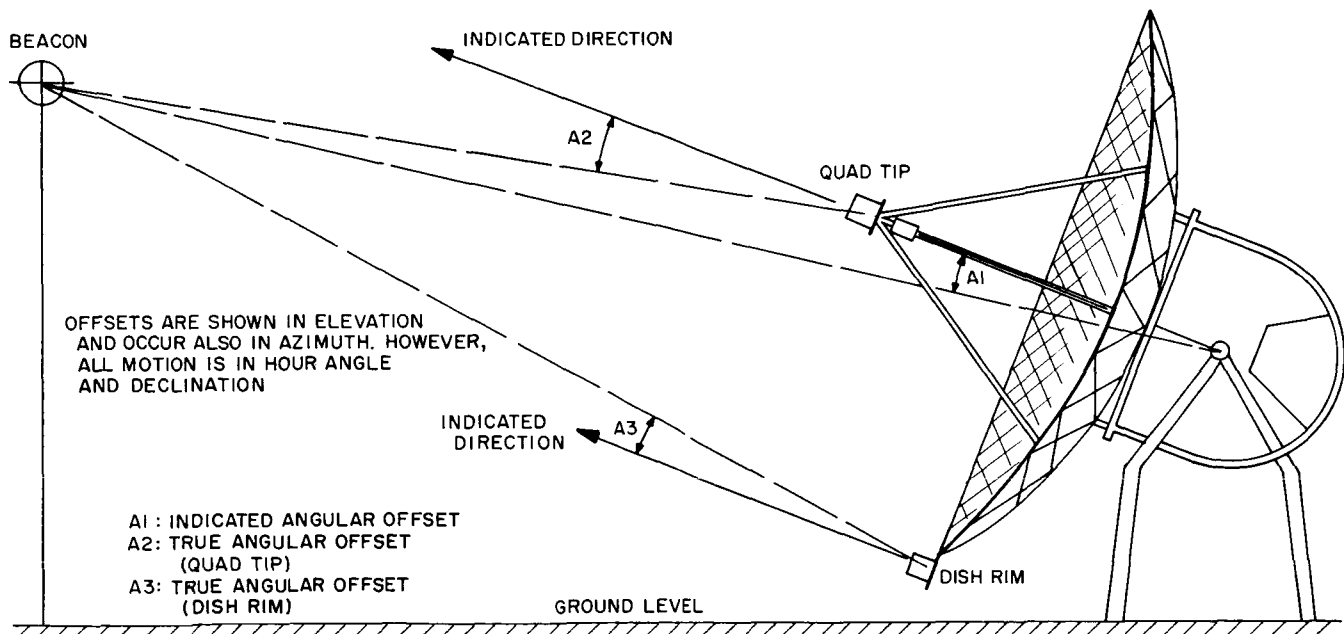


Fig. 2. Location of acquisition aid (diagram)

of the data due to the phase centre movement with angle referred to above. These problems will be apparent from inspection of Fig. 2 and were solved using the IBM 7090 computer.

Antenna patterns and angle error curves were taken in hour angle and declination for both horizontal and vertical polarization with the acquisition aid at the quadri-pod tip and at the dish rim. The dish rim location was chosen so that it was near the ground at low elevations when the antenna pointed in the azimuth of the boresight tower. Its precise location is defined in Fig. 3. Two sets of quad tip patterns were taken, with and without a ground plane extension, so that the effect of acquisition aid dish coupling could be observed.

In addition, the signal strength and angle errors were digitized (using instrumentation section VCO's and data section doppler counters) and punched out on paper tape together with antenna pointing angle, thus facilitating automatic data processing.

5. Aircraft Tracks

The measurements taken using aircraft tracks provide evidence of performance under more realistic conditions than the boresight tower. The signal source is distant and, in addition, is moving in a manner not too unlike a spacecraft.

The flight plan is shown in Fig. 4; the portion of interest is the straight run along the 300-deg azimuth. This azimuth was chosen because it gave a full range of elevations down to the horizon and was a possible acquisition direc-

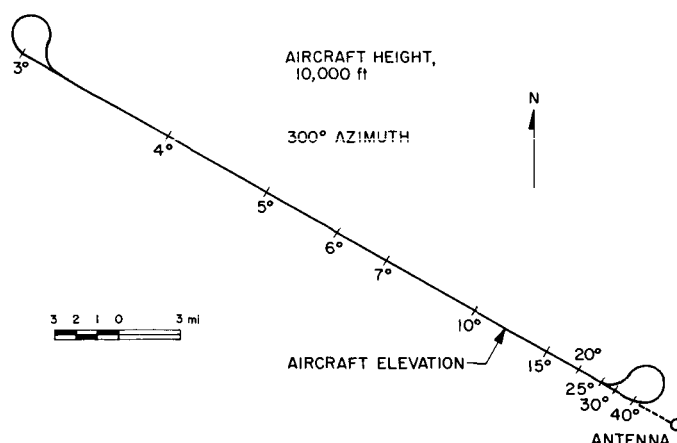


Fig. 4. Flight plan for aircraft track

tion. The dish rim acquisition aid location was near the bottom of the dish for this azimuth (Fig. 3).

The aircraft was tracked along the straight portion of the flight plan in the track mode. Then, at a predetermined elevation, the antenna was stopped and the acquisition aid switched in allowing the aircraft to fly out of the acquisition-aid beam. When the aircraft elevation had changed by a reasonable amount (where possible, 10 deg) the antenna was switched to automatic and the aircraft reacquired. Usually this occurred without difficulty. This procedure was carried out for elevations of 5, 10, 15 and 20 deg on both incoming and outgoing legs of the flight plan. In addition, a few runs were taken on azimuth 60 deg, which gave some comparative records with the acquisition aid at the top of the dish.

Throughout the flight, signal strength and angle errors were recorded on the Midwestern ultraviolet-light oscillograph recorder together with the usual station parameters such as time and antenna switch position. The angle errors were also digitized (using instrumentation section VCO's and data section doppler counters), sampled every 2 sec together with time and antenna pointing angle, and punched out on paper tape.

The data was reduced using IBM 7090 computer programs. The aircraft position when the antenna was stopped was deduced by extrapolation of the tracking data assuming a constant aircraft course at the known constant height. Further assumptions were that the aircraft was flying on a constant bearing with respect to the antenna and that, while tracking, the data readouts always showed the true line of sight to the aircraft. It is estimated that the data reduction and extrapolation are accu-

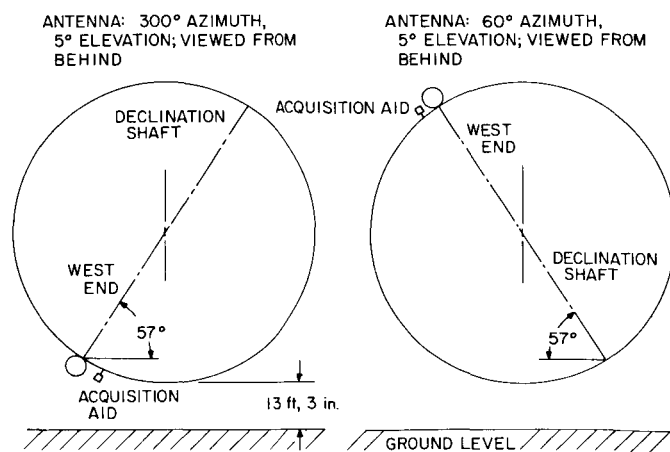


Fig. 3. Location of acquisition aid (dish rim)

rate to about 1 deg which is considered quite adequate for the type of investigation being conducted.

6. Evaluation

a. Boresight measurements. One type of perturbation is due to the presence of a small amount of ground reflection aggravated by movement of the phase centre of the acquisition aid with respect to the ground as the angles were varied.

A more serious type of perturbation is due to coupling between the acquisition aid and dish and is significant only in the quad tip location. The reduction in coupling when a larger ground plane is fitted to the acquisition aid in this location is very marked, although the curves are still not as smooth as using the dish rim location. However, further reduction in coupling is to be expected with a distant source since the energy concentrated by the dish would be focused further away from the acquisition aid.

The higher elevation S-curves are progressively better and the dish rim low location continues to show slightly better performance. There is some smoothing of the S-curves above 20-deg aircraft elevation due to the 2-sec sampling rate, but this is not excessive.

It was found that in both locations, in spite of the large ground reflection effects, the system always acquired from misalignments of 10 deg in elevation up or down at aircraft elevations above 15 deg. At the lower aircraft elevations, down to 5 deg, acquisition was usual although not certain. Not enough information was collected to establish which location gave the better performance in this respect, although it is believed that the dish rim low location is slightly superior.

B. Mark I Ranging Subsystem

The DSIF Mark I ranging subsystem is being designed and built to equip the DSIF with the capability of ranging on passive satellites and spacecraft "turnaround" transponders to distances of 800,000 km. Earlier installments of the description of this subsystem have been given in Volumes III of *Space Programs Summaries* Nos. 37-20, 37-21, and 37-22. In this summary the design and operation of the final two functional units are described.

1. Program Unit

(Note: This unit was referred to as the "Control Unit" in SPS 37-20. It has since been renamed.)

The program unit (Fig. 5) controls the sequential operation of the ranging subsystem. In that this subsystem is a special-purpose machine, the program is permanently wired and is not readily subject to change as, for instance, from one mission to another.

The program unit provides a "reset" state and seven sequential program states, numbered $p1, p2, \dots, p7$. In connection with the program unit there are two operational push buttons on the control panel, viz., RESET and START. Actuation of the reset button causes the program unit to enter the reset state, in which the unit is cleared and readout from the subsystem is disabled. Actuation of the start button is required for entry into state $p1$, with the additional provision that the selected S-band receiver and the ranging clock loop be in lock. Fig. 5 shows a functional block diagram of the program unit. It shows the various program states, the condition for entry into each state, and the activities which the various portions of the ranging complex are called upon to perform in each state.

Once the start button has been pushed and the subsystem enters state $p1$, it goes through the other program states sequentially and automatically as the respective state-entry conditions are fulfilled. Finally, the program unit enters state $p7$, which is the tracking and ranging state. In this state the readout register is enabled, since valid range numbers are then available. If, at any time during acquisition or tracking, RF lock is lost, the program unit immediately returns into the reset state.

Time synchronization of the program states is provided by a "step" pulse which, in the automatic mode of operation, is generated once each major machine cycle, or every 124 μ sec. Only at that time is it possible to step from one program state to the next.

A manual mode of operation is also provided for checkout, test, and troubleshooting purposes. In this mode the start button must be pushed not only to step from the reset state into state $p1$, but also to step from any other program state into the next in sequence.

Upon entry into states $p3, p4, p5$, and $p6$, an "acquire" pulse is generated which serves to initiate the acquisition subroutine for acquiring code components x, a, b , and c , respectively. This subroutine is under the control of the

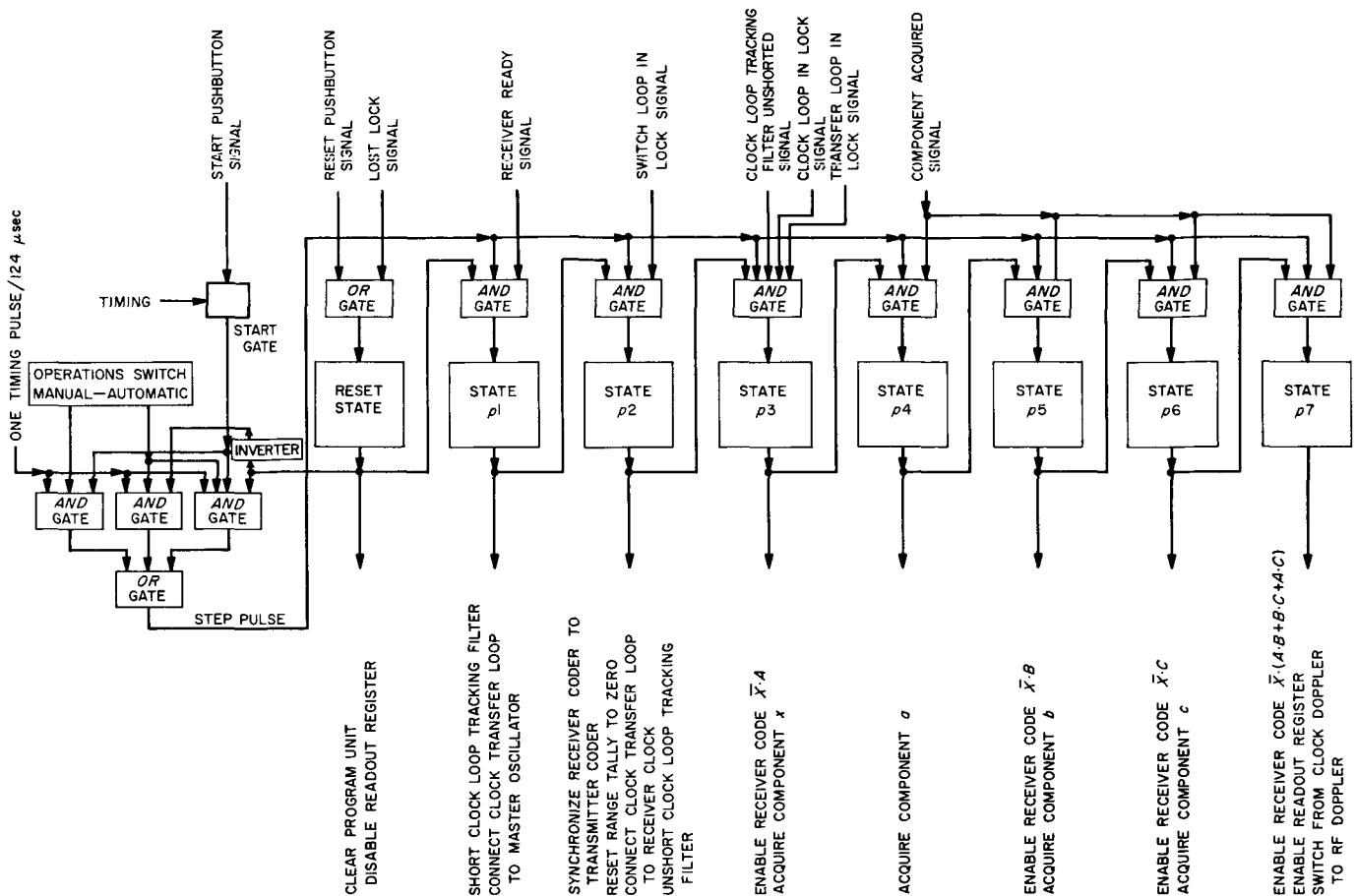


Fig. 5. DSIF Mark I ranging subsystem program unit

acquisition unit. At the end of each component acquisition, a "component acquired" signal is received from the acquisition unit; this returns control to the program unit and permits it to advance into the next successive program state.

Once every major machine cycle ($124 \mu\text{sec}$) the program unit generates a "convert command" which is transmitted to the voltage digitizer. It causes the voltage digitizer to generate a digital sampling of the receiver code correlation voltage as of that moment.

2. Acquisition Unit

The acquisition unit (Fig. 6) performs, without assistance from any other unit of the subsystem, the complete acquisition of a given component of the received code. A particular component acquisition is initiated by the program unit, as mentioned above.

The acquisition unit causes the receiver coder to shift the receiver code component 1 bit at a time, until all

shift positions have been examined. After each shift the correlation voltage from the receiver is sampled and digitized a predetermined number of times. These samples are summed, yielding a finite time integral of the correlation voltage which, in turn, is an analog measure of the degree of correlation in phase between the received code component and the receiver code component. The shift position that yields the largest time integral is determined, and the receiver code component in question is then again shifted into that relative position. The particular code component has then been acquired, and control is returned to the program unit.

The digitizing of the correlation voltage is performed, on periodic command (every $124 \mu\text{sec}$) from the program unit, by a commercial analog-to-digital converter, "Voldicon" VR-10-AB, the output of which is 10 binary bits plus sign bit.

The number of samples to be taken is a function of the received signal strength, i.e., signal-to-noise ratio. This must be determined by the operator prior to ranging

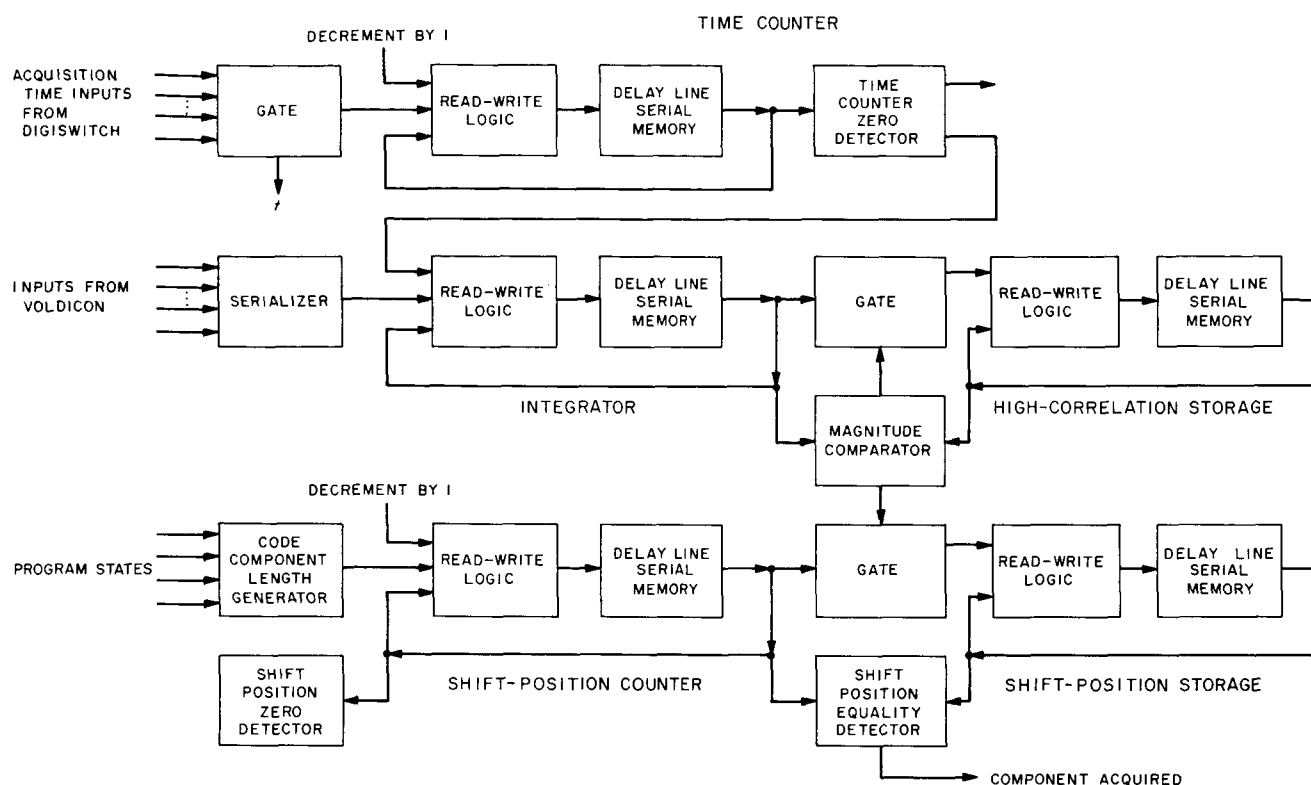


Fig. 6. DSIF Mark I ranging subsystem acquisition unit

acquisition. A multi-position "Digiswitch" on the control panel is then set to a suitable number of samplings. The switch settings permit a choice of from 1 to 2^{19} samplings per shift position.

The particular code component to be acquired is determined by the program state. Thus, components x , a , b , and c are acquired in program states $p3$, $p4$, $p5$, and $p6$, respectively. The binary number equivalent to the bit length of the component is initially gated into the shift-position counter. This number is then decremented by one each time the receiver code component is shifted. Thus, when this counter is in its zero state, the code component has been shifted through all positions and is back to its original position.

The number of samples to be taken for each shift position is, as mentioned above, determined by the manual setting of the Digiswitch. The binary number corresponding to the setting is stored in the time counter. For every sampling, i.e., once per $124\text{-}\mu\text{sec}$ major machine cycle, this number is decremented by one. A zero detector senses when the counter reaches zero and initiates the next receiver-code-component shift command. After any

code-component shift a certain amount of time must be allowed before the new RF steady-state condition can be reliably determined. The time counter is again used to provide this alternative function, being pre-set with a number corresponding to the necessary time. Again this counter is decremented by one every major machine cycle. The zero detector in this case initiates the start of the correlation-voltage integration.

The integrator sums the digitized correlation-voltage samples by adding each new sample to the previous content of the circulating register. When all the samples have been added, the register holds the correlation integral for that particular shift position.

The high-correlation storage is loaded with the first correlation integral obtained for a given code component. Each succeeding correlation integral is compared with the one currently in the high-correlation storage. If the new value is the larger of the two, it is made to replace the old one in the high-correlation storage and, simultaneously, the number currently in the shift-position counter is copied into the shift-position storage. Thus, when the integration has been performed in all shift

positions of the code component, the number in the shift-position storage corresponds to the shift position which produced the largest correlation integral.

The shift-position counter is then loaded with the code-length number for the second time, the code component is shifted, and the position count decremented until the count is equal to the number in the shift-position storage. The code component has then been acquired, and the output of the equality detector signals the program unit to proceed into the next program state.

3. Project Progress

A surplus cabinet has been obtained and is being utilized to contain a laboratory prototype of the ranging subsystem. Except for a few minor peripheral items, the system design is complete. Construction of the laboratory prototype is close to completion, lacking only certain interconnections and control wiring. More than half of the digital modules for the DSIF unit Serial No. 1 have been wired. A specially modified DSIF rack has been obtained to contain Serial No. 1, and additional racks for Serial Nos. 2, 3, and 4 are on order.

C. GSDS Telemetry Data Encoder

1. Concept of Design

The present development of a telemetry data encoder is the result of reviewing the costs and needs of previous missions. It is felt that much can be gained from a device that is not program oriented and will extend its useful life beyond a single mission or small block of missions. These studies have shown that, while the initial cost of development would be higher than that of program oriented equipment, this cost would be quickly regained as its functional role spanned more than one program.

Another result of looking back over previous missions is the current study being conducted to determine the feasibility of using error detection/correction codes to provide better utilization of the channels available. This article presents the guidelines being used in the encoder development and the work that has been completed in testing channels using parity codes.

2. System Design Characteristics

The following is a listing of the characteristics and parameters to be utilized as guidelines for the encoder design.

a. Data input characteristics.

- (1) Data input rates corresponding to a maximum of 5,000 bits/sec are planned. Lower bit rates will be acceptable.
- (2) Parallel or serial binary data input will be acceptable.
- (3) Variable word lengths with a maximum fixed for particular mode of operation. Data having several different word lengths in one data frame will have to be processed as if it had a single word length. (i.e., *Mariner C* scientific data has three word lengths of 6, 8, and 10 bits. This data would have to be processed as if all words contained 10 bits.)
- (4) The data input source can be either from a data modulator or a data decommutator.

Data originating from a data demodulator (not decommutated) will not be edited within the encoder and the incoming data rate cannot exceed 75% of the transmission capability of the ground communication link.

Data originating from a data decommutator will be capable of being edited within the encoder and the incoming bit rate can be up to 5,000 bits/sec. (Data identification information or frame sync information will be required also.)

b. Data output capability.

- (1) The encoder will be capable of outputting data for transmission to any of the following links singly, or to several, but not all, in combination (i.e., one 4800-bit/sec wideband data link and two teletype lines at 30 or 50 bits/sec).

4800-bit/sec serial wideband data link
 2400-bit/sec serial wideband data link
 1200-bit/sec serial wideband data link
 600-bit/sec serial wideband data link
 50-bit/sec 5-bit parallel teletype
 30-bit/sec 5-bit parallel teletype

- (2) Only simple data editing techniques will be provided (removal of unwanted data words corresponding to a predetermined program).

- (3) Editing schemes will be governed by input data rates, output data rates, and format requirements. Unlimited editing capability will not exist.
- (4) Sufficient storage capacity and editing capability will exist such that all communication circuits can be operated at the maximum capacity, subject to the constraints to be established for editing schemes.

c. Error detecting codes.

- (1) Error detecting codes will be used to minimize the number of undetected errors in the data.
- (2) Error detecting codes will be optimized for a given data block length and the anticipated maximum number of errors per block of data, for most operating conditions. Operation during extremely adverse communication periods is not anticipated.
- (3) The error detecting codes will contain limited error correcting capability. The error correcting capability will be primarily suited for correcting errors encountered during normal communication circuit operation.
- (4) Several error detecting codes may be utilized for different modes of operation in order to maintain optimum transmission capability.

d. Encoder interface modules.

- (1) Interface modules will be required, in some cases, for mating with various demodulators and demodulators.
- (2) Interface modules for the communication circuits will be provided for those circuits defined in Paragraph b (1). Interface with other types of communication circuits will require different modules.

e. Concept of operation. Fig. 7 outlines the operation of the system as it is presently proposed. Data will enter the input serial/parallel converter at rates of 5,000 bits/sec or less. If it arrives in serial form, it will be converted into words of 10 bits or less depending on the word length format of the mission. Initially these words are transferred into input buffer A. The length of the input buffer will vary according to the frame length of the incoming data, being long enough to contain one frame of data. When input buffer A is filled, the incoming data is then transferred to input buffer B. While the data is entering the second input buffer, the data in input buffer A is trans-

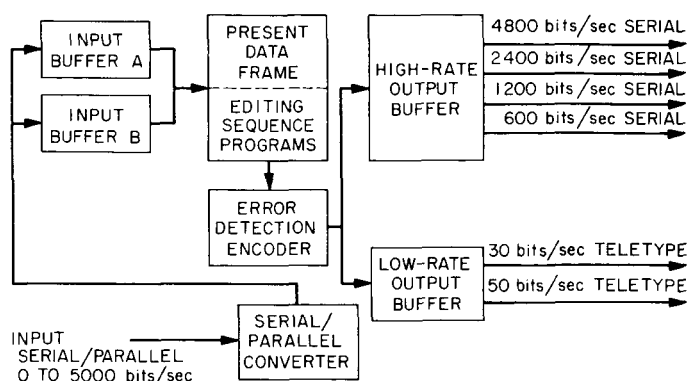


Figure 7. Telemetry data encoder system

ferred into the central memory of the system. This central memory contains both the frame of data to be operated on at the present time and the sequential editing programs that have been entered at some previous time. Depending on which output combination is selected, the correct editing sequence is chosen. The sequence of words stored in memory is then selected from the frame of data stored in the central memory. This data is then encoded or transferred directly, if desired, to the selected output buffer. At this time, the control system interrogates the various input and output buffers. If input buffer B is still in the process of being filled, the editing control then encodes and loads the next highest priority output buffer with a block of data to be transmitted. The interrogation continues in this fashion until input buffer B is filled. If input buffer B fills before the control center is able to unload it into the central memory and update the present frame of data, the new incoming data frame is switched back to input buffer A, which has previously been unloaded. Each of the output buffers is divided into two sections similar to the input buffer with one of the sections transmitting and the other either filled and ready for transmission or immediately available for filling when the control network senses the proper conditions. In this manner, there is a continual flow of data in an asynchronous manner both into the encoder and out to the transmission links. The limitations on the number of transmission lines that may be used at one time are dependent on the time required to transfer and encode each word of data.

In actual usage if either the 4800-bit/sec or the 2400-bit/sec high-rate transmission lines are used, none of the other high-rate lines will be able to be used. Two 1200-bit/sec or one 1200-bit/sec and one 600-bit/sec may be used simultaneously.

3. Data Encoding Study

After examining available data (Refs. 1 through 12) regarding the statistics on errors of the communication lines available, it was considered worthwhile to make a study of the feasibility of error detection/correction encoding and its possible application in future DSIF telemetry transmission. Since the information on the error patterns indicated nonindependent errors with the majority of the bursts being in groups of 3 or fewer bits, three codes were selected and implemented. One of these codes is derived from a characteristic equation of the form:

$$(1 + T) M(kT) = 0 \quad (1)$$

where $M(kT) = 0$ is a characteristic equation that produces a maximum length cycle of length $2^k - 1$. This provides us with a double adjacent error correcting code. It is derived from a characteristic equation of the form:

$$(T^p + 1) M(kT) = 0 \quad (2)$$

where p is prime to $2^k - 1$. This gives rise to codes of length $p(2^k - 1)$ with $p + k$ check digits. This type of code is called a Fire Code. It will correct all errors within a burst length $(p + 1)/2$, p odd; $p/2$, p even, as well as many more. Due to the fact that this is not an optimum code the remaining redundancy that the code contains can be used for the detection of other errors. This is done by examining the shift register at the end of the correction procedure to see whether it is zero. Ref. 4 provided the form for the third code. It is a generalization of codes discovered by Abramson and Melas, and has a characteristic equation of the form:

$$(T^2 + T + 1) M(kT) = 0 \quad (3)$$

and will correct burst lengths equal to, or less than, 3. This is an optimum code and the redundancies available in the Fire Code which are utilized for additional error detection will not be found here.

In deriving the characteristic equations, $M(kT)$ was selected from the tables in Ref. 11, with the following results.

Case (1).

$$M(kT) = T^9 + T^4 + 1$$

$$(1 + T)(T^9 + T^4 + 1) = T^{12} + T^8 + T^7 + T^5 + T^3 + 1$$

Case (2).

$$M(kT) = T^7 + T^3 + 1$$

$$\text{Burst} = 3$$

$$(p + 1)/2 = 3$$

$$p = 5$$

$$(T^5 + 1)(T^7 + T^3 + 1) = T^{12} + T^8 + T^7 + T^5 + T^3 + 1$$

Case (3).

$$M(kT) = T^{10} + T^4 + T^3 + T + 1$$

$$(1 + T + T^2)(T^{10} + T^4 + T^3 + T + 1) = T^{12} + T^{11} + T^{10} + T^6 + 1$$

The implementation of the characteristic equations for use in encoding and decoding was derived from Ref. 1. These equations have been implemented by simulating feedback registers in the SDS 920 computer. The resulting sequences have been generated and a decoding program has verified their validity. The characteristics in each case are listed below.

The correctable error patterns are binary representations of the burst patterns that, when detected, may be corrected. A "1" indicates a single error while a "101" indicates that the 2 outside bits of a 3-bit block are in error.

Case I	
Total length of code	511 bits
Total information block	501 bits
Total parity block	10 bits
Frame sync	18 bits
Word sync (31 words)	31 bits
Total transmission frame	560 bits
Transmission efficiency = $\frac{\text{Total information block}}{\text{Total transmission frame}}$	
	$= \frac{501}{560} = 0.894$
Correctable error patterns	1 11

Frame sync and word sync format were derived from information available in Ref. 12. Their size and the total length of the code were arranged so the total transmission frame would result in multiples of five for transmission over the five levels in a teletype channel.

Case II	
Total length of code	635 bits
Total information block	623 bits
Total parity block	12 bits
Frame sync	11 bits
Word sync (64 words)	64 bits
Total transmission frame	710 bits
$\text{Transmission efficiency} = \frac{\text{Total information block}}{\text{Total transmission frame}}$ $= \frac{623}{710} = 0.877$	
Correctable error patterns	1
	11
	101
	111
Case III	
Total length of code	1023 bits
Total information block	1011 bits
Total parity block	12 bits
Frame sync	27 bits
Word sync (40 words)	40 bits
Total transmission frame	1090 bits
$\text{Transmission efficiency} = \frac{\text{Total information block}}{\text{Total transmission frame}}$ $= \frac{1023}{1090} = 0.939$	
Correctable error patterns	1
	11
	101
	111

D. Computer Controlled Antenna Pointing System

The value of having an automatic antenna positioning system was proved at the Goldstone Tracking Station during the *Mariner 2* mission. Precomputed drive tapes for tracking during visibility periods were used almost exclusively during the 109 days of *Mariner's* trip to Venus. The automatic tape drive system offers as advantages:

- (1) Rapid acquisition time.
- (2) Freedom of dependence on signal strength required in automatic tracking modes.

- (3) Use of listening feeds on the antenna for greater received signal strength.

A study has been launched to define a tape drive system with expanded and more flexible capabilities for use throughout the DSIF and the Advanced Antenna System. The results of this investigation are described later in this article. The existing positioning system at Goldstone was built for a special application and the cost involved in modification or expansion of its capabilities is prohibitive. The heart of the proposed new system will be a general purpose digital computer. The reasons for selecting a general purpose computer are listed below.

- (1) *High reliability.* A high degree of reliability has been demonstrated in today's general purpose computers. Relatively long mean time to failure data has been shown by computer manufacturers. Ease of maintenance is obtained by use of diagnostic routines, which localize faults to a few circuit modules. Modules of most computers are of plug-in type and can be easily replaced. In addition, many self checking methods are available on digital computers. Errors on inputting and outputting information to and from the computer can be detected by use of parity bits. Many computers also use parity error detection when words are entered or withdrawn from memory. Another useful feature of a general purpose computer is that errors in the handling of information within the computer can be checked by the use of program control. For example, a calculation is to be performed where the result is known to fall in a certain range of values. The computer can be programmed to detect an answer outside this range, give notification that an error has occurred, and go to an alternate routine for obtaining the desired result.
- (2) *Increased versatility.* Most system changes would only involve programming changes, which require no additional hardware or engineering design costs. The flexibility of the general purpose computer would allow other jobs to be undertaken, apart from the original intent, on a time sharing basis. During nontracking periods the computer could perform other tasks on a full time basis.
- (3) *Low cost.* Today, the price of the small general purpose computer has decreased due to increased competition and high volume production. The cost of engineering and hardware for special purpose logic systems, much of the time, exceeds the total cost of a computer and lacks the versatility.

- (4) *Easy integration.* As the DSIF moves to complete computer controlled station automation, a general purpose computer can be integrated into a total system of this type. Not only can one computer be easily controlled by another, but in the case of failure of a computer one can be programmed to serve as a backup and perform some of the functions of others, while continuing on its primary mission.

Basically, the system (Fig. 8) when in operation will be closed in the servo drive loop of the antenna. The input to the system will be the binary representation of the antenna position (hour angle and declination) from the angle encoding equipment. The output of the system will be an analog voltage proportional to the antenna position error. The computer compares the present antenna position from the encoding system to the desired reference position and outputs a positive or negative digital representation of the difference between the two angles. This digital number is then converted to a plus or minus voltage equivalent to the pointing error. This error voltage will command the servo system to drive the antenna to the correct position. The desired reference position will be derived from three sources:

- (1) Ephemeris drive tape input containing samples of angle position for a given time.

- (2) Sidereal clock located in the computer.
- (3) Manually selected coordinates inputted from the system control panel.

Rate and position offsets may be used to modify the tape and sidereal drive positions. A system control panel located on the servo console will be used to select the mode of operation of the computer. Programs are being written for system simulation planned for Goldstone this Fall.

1. Tape Drive Mode

The program for positioning the antenna by an ephemeris drive tape is nearly completed. In this mode, the computer will position the antenna to the angles on the tape and perform linear interpolation between samples. Some of the features that are being incorporated in this program are:

- (1) The time interval between tape samples may be varied from 2 sec to 10 min in 1-sec steps.
- (2) An error in the drive tape format or unallowable characters on a sample will be detected and the reading will be disregarded.
- (3) A tape time offset may be introduced from the control panel.

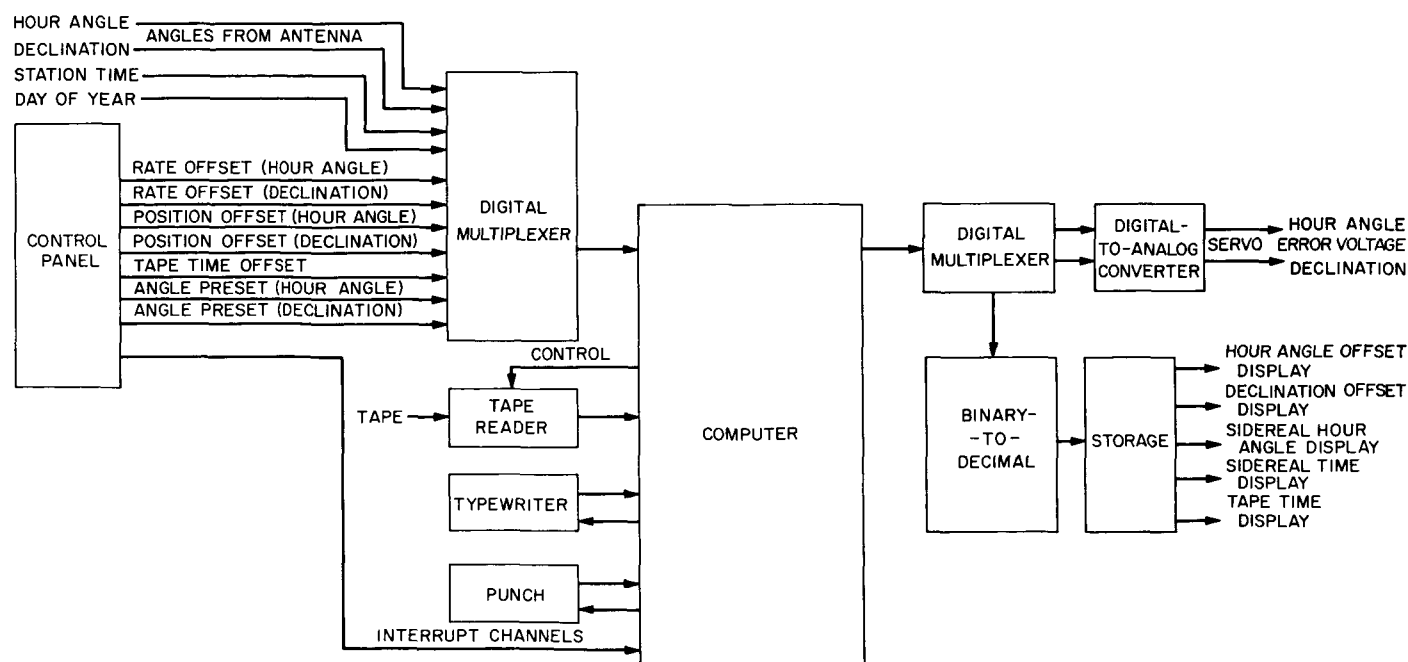


Fig. 8. Automatic tape drive system block diagram

2. Sidereal Clock

While the computer is performing other functions it also incorporates a sidereal clock which will read out the Greenwich hour angle of Aries in degrees from 000.000 to 359.999 deg in 0.001-deg steps. A startup routine is required to preset the clock to the proper value. The equation for determining the Greenwich hour angle of Aries at any desired time was taken from Ref. 13. This equation was written for 1950 and it has been corrected for any desired time in 1963. The new equation is as follows:

$$\theta = 98,939816655 + 0.985647346D \quad (1)$$

where

θ = required Greenwich hour angle of Aries.

D = day of year + fraction of day elapsed past 0 hr January 1, 1963.

The initializing program will automatically be executed as a part of the computer power-on startup routine. This assures that the clock will be preset to the correct value every time power is applied to the computer.

Once the clock is initialized to the Greenwich hour angle of Aries, the sidereal time is updated by using interrupts from the station time standard. The clock will be checked periodically by the initializing routine to determine if any malfunction has occurred.

When the value of the Greenwich hour angle of Aries is obtained by the initializing routine, the angle of the west longitude of the station is subtracted. The net result is that the sidereal clock reads out in local sidereal time. The local sidereal time is then displayed in six decimal digits. The interrupts used for the sidereal clock have the highest priority of all the operations performed by the computer.

The sidereal clock is used when it is desired to move the antenna at Earth rates. The relationship used to drive the antenna is denoted by the equation:

$$SHA = LHA - (GHA - W. Longitude) \quad (2)$$

where

SHA = the required sidereal hour angle of a star or spacecraft to be tracked.

LHA = local hour angle of the antenna as inputted to the computer from the antenna angle encoding system.

GHA = Greenwich hour angle of Aries.

W. Longitude = west longitude location of the station.

$(GHA - W. Longitude) =$ local sidereal time.

The desired value of SHA is entered in the computer by a single reading inputted by the tape reader or from a reading selected by digital switches on the angle preset portion of the control panel. Declination readings are inputted with the SHA. Since SHA is a constant, as local sidereal time increases, there is a corresponding increase in LHA. Any discrepancy in the equality of Eq. (2) will send to antenna servo system as an error signal to drive the antenna to the proper position. Declination will remain constant at the value inputted to the computer. If it is necessary to have either SHA or declination change linearly with time, rate offsets may be placed in the computer.

3. Position and Rate Offset

When the computer is in the sidereal or tape drive modes, it will be possible to introduce either a position or rate offset from the control panel. The offsets are added or subtracted from the encoder input from the antenna. The result of the arithmetic operation is compared to the reference angle to derive the servo error signal. Offsets are selected by means of digital switches on the control panel and entered into the computer when interrupt occurs by pushing an initiate button. The position offset ranges from 0.999 to 0.001 deg with 0.001-deg resolution.

Rate offset information will be inputted in degrees per second varying from 0.9999999 to 0.0000001 deg with 0.0000001-deg/sec resolution. Offsets may be either positive or negative and the accumulated offset in hour angle and declination will be displayed on the control console. Provision is made for push button interrupt to clear the accumulated offset on either axis on command.

4. Angle Preset

Digital switches located on the control console may be used to enter any hour angle-declination coordinates.

The angles are selected in six digit decimals. Pushing an angle preset initiate button interrupts the computer to a program that inputs the selected coordinates and drives the antenna to the desired position. The angle preset selector switches may also be used in the sidereal mode to enter in SHA and declination coordinates.

The previous description covers the primary objectives of the computer controlled antenna positioning system. Numerous options to what has been discussed are available by modifying the program of the computer. Some of the jobs that could be assumed by this system as additional features are:

- (1) Computing pointing information from given trajectory equation.
- (2) Computing the trajectory equation from angle information gathered during a tracking period.
- (3) Programming the antenna to search patterns for spacecraft acquisition during nonstandard missions.
- (4) Processing (on-site) of real-time telemetry and tracking data.

The computer controlled antenna pointing system will be orientated in its design philosophy for eventual integration with an automatic acquisition system and computer controlled station operation system.

E. AAS Wind Data Gathering System

During this reporting period, the Advanced Antenna System Wind Study (*SPS 37-13*, Vol. I; *SPS 37-16*, Vol. III; *SPS 37-21*, Vol. III) data recording instrumentation final checkout was started. At present writing, the checkout is 75% complete.

The Potter tape recorder bit density was converted to 556 bits/in.; and the IBM 7090 computer program which had been written to dump the raw data in octal format was extensively modified to facilitate system checkout.

All of the drag spheres (wind force sensors) up to the 20-m level on the main tower were removed from the tower and calibrated using the analog portion of the data

recording instrumentation system. They were subsequently replaced and some analog wind force data was recorded using an eight-channel Sanborn recorder which was also installed in the van during the reporting period.

Further investigation of the 8-cps resonance in the drag sphere output reported in *SPS 37-21*, Vol. III, has led to formulation of a wind tunnel test program to determine the force transfer characteristics of drag sphere plus quadripod pipe stand. Implementation of the program is presently in progress. The tests will be conducted during the next reporting period.

F. High-Power Test Laboratory

The high-power test laboratory discussed in *SPS 37-18* has been moved to a new facility and expanded to S-band capabilities. The test laboratory (Fig. 9) is located at the antenna range at Goldstone. It is a completely independent 10-kw transmitter system with a 20-kv power supply, a heat exchanger, and a klystron dolly. The addition of two 10-kw S-band klystrons and associated magnets has extended the capability of the high-power test laboratory for testing all new high-power waveguide components that are to be used in the DSIF S-band systems.

Diplexing tests into the first and second prototype S-band feeds have been run to determine if they break down under high power. No arcing occurred when the transmitter was operated in excess of 14 kw. In another series of experiments, the transmitter was operated at 10 kw to determine the increase of noise temperature and degradation to threshold of a maser and parametric amplifier operated separately and concurrently as a front end to a phase-lock-loop receiver. A block diagram of the test setup is shown in Fig. 10.

An evaluation test was conducted on each of the two S-band 10-kw klystrons to determine which tube was most acceptable for use in the DSIF S-band transmitters. The Eimac tube was recommended for use in the transmitters because of its wider versatility as compared to the other 10-kw klystron. Other high-power components such as waveguide switches, harmonic filters, isolators, and directional couplers will be tested before being accepted into the new S-band systems.

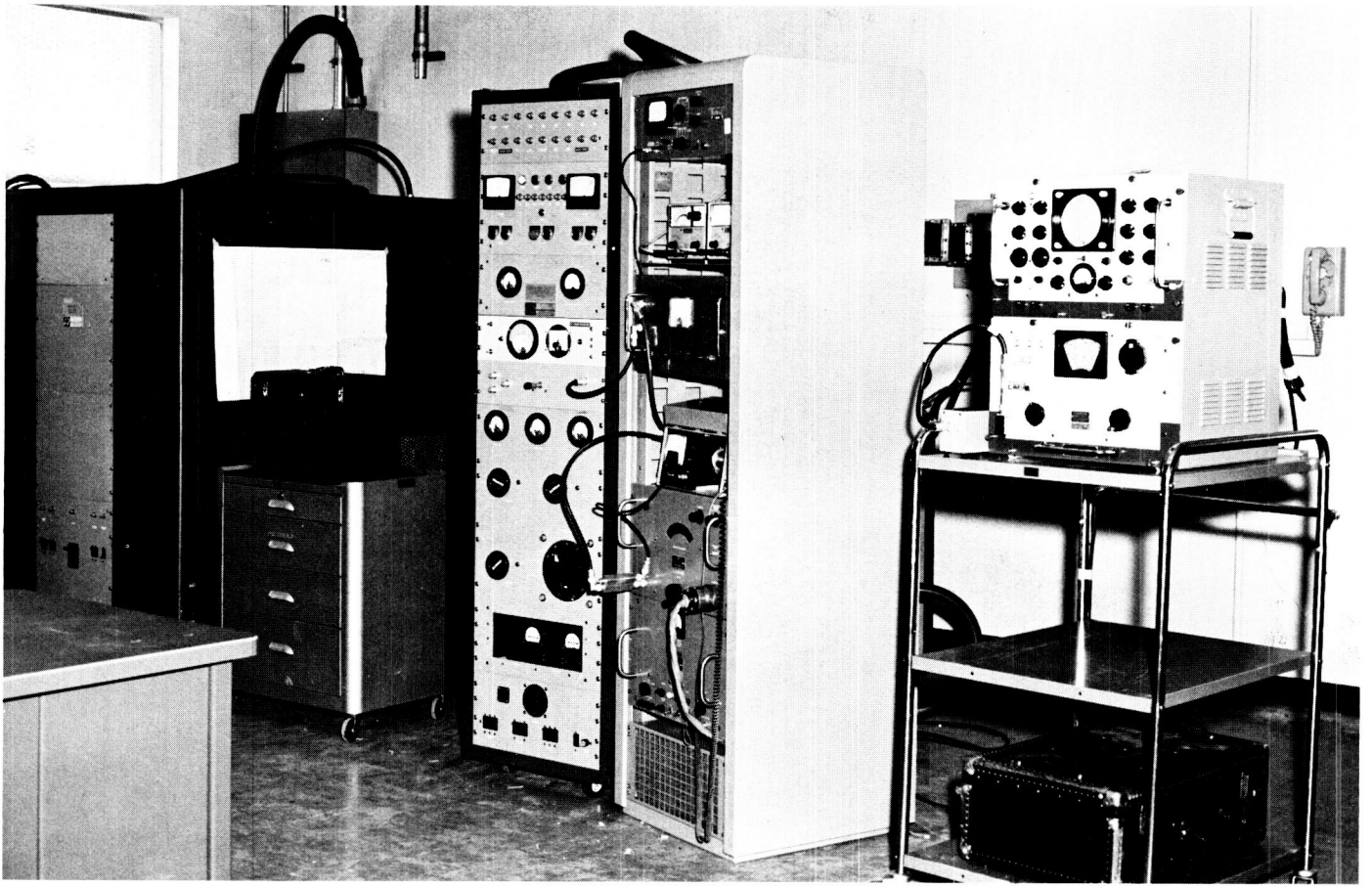


Fig. 9. High-power test lab, 10-kw transmitter

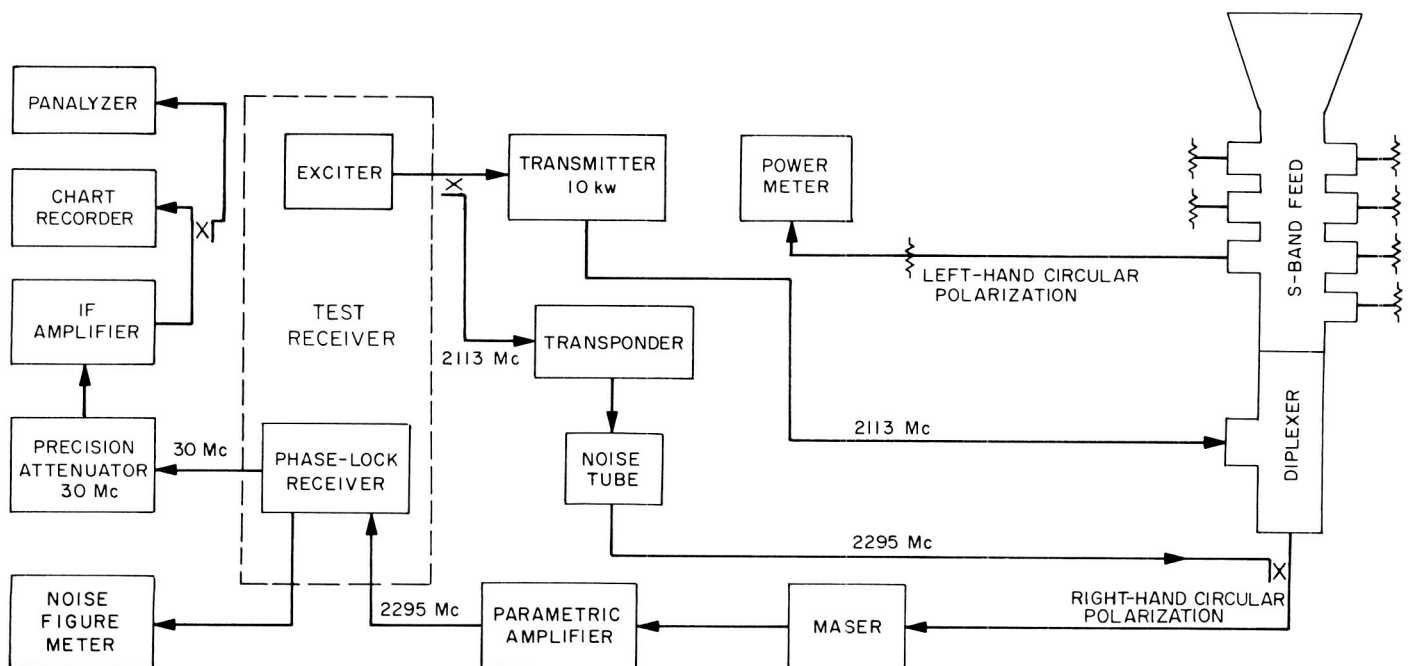


Fig. 10. S-band high-power cassegrain test setup

G. Systems Engineering

The systems engineering function within the DSIF is concerned with three types of activity:

- (1) *DSIF systems engineering* (the definition of the Deep Space Instrumentation Facility and documentation of its capability).
- (2) *DSIF project engineering* (the defining of DSIF requirements and commitments to spacecraft projects such as *Ranger*, *Surveyor*, and *Mariner*).
- (3) *DSIF systems analysis* (the detailed theoretical analysis of circuits, systems, and problems related to DSIF performance).

The status of these activities is as follows:

1. Systems Engineering

Coordination support was provided to the S-band project to establish a final block diagram, functional specifications, and project organization chart.

An Engineering Planning Document was prepared describing the control of radio frequency interference in the DSIF (Ref. 14). This plan outlines the necessary manpower, equipment, and funding necessary to implement the DSIF with a capability to control radio frequency interference.

2. Project Engineering

DSIF support was provided for the following projects:

- (1) *Surveyor*. A revised interface specification was prepared with the latest S-band capability changes (Ref. 15).
- (2) *Voyager*. The final draft of a JPL proposal for the *Voyager* Mission was reviewed and revised in matters relating to the DSIF commitment.
- (3) *Ranger 5*. Several meetings were held with Northrop Space Laboratories personnel to orient them on the DSIF capability.
- (4) *Pioneer*. Meetings were held at both JPL and at Ames Research Center regarding the use of the Deep Space Instrumentation Facility for tracking support of the *Pioneer* probe. Several meetings were held with Space Technology Laboratory, the contractor for *Pioneer*, to orient them on *Surveyor*-type and *Mariner*-type command and telemetry systems.

- (5) *Solar probe*. A presentation was made for Ames Research Center to its study sub-contractors, General Electric, Martin and Philco. The capability of the DSIF was discussed at this meeting.
- (6) *Mariner C*. A study was made and a plan proposed to supplement the existing 100-kw transmitter capability at the Venus site of the Goldstone Tracking Station. It is now planned to provide both command and doppler capability during the final months of the *Mariner C* mission by use of this research capability. The necessary doppler and command equipment will be procured and installed to provide this supplemental capability.

3. System Analysis

The Johannesburg site was reviewed for potential radio frequency interference problems associated with the proposed operation of a range and range-rate station. Site criteria and isolation values were established for this review.

A functional specification for the S-band doppler subsystem was prepared as part of the over-all S-band system documentation. The input and output relationships were specified.

Fig. 11 shows the DSIF interface areas and the types of specifications required. Fig. 12 diagrams the current activity of the systems engineering function.

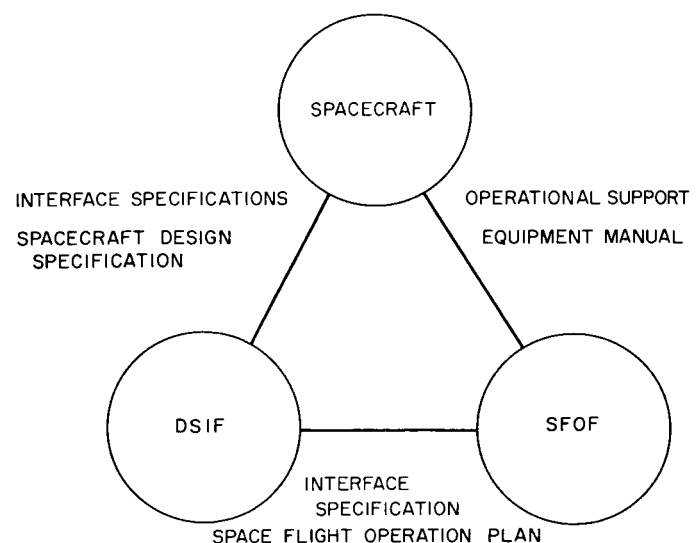


Fig. 11. Typical interface areas

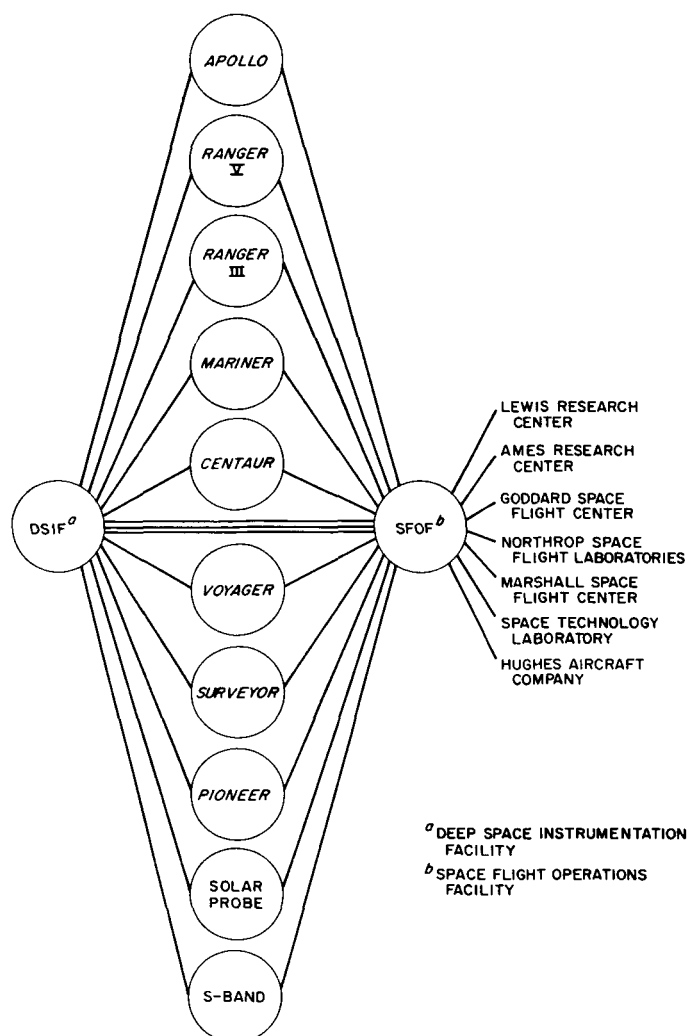


Fig. 12. Existing project activity

acceleration and the hour angle velocity and acceleration necessary to track the satellite at any given time. A program was written which solves the problem in the following manner: Knowing the classical elements, the position of the satellite can be described as a function of the eccentric anomaly, E , in a geocentric, rectangular coordinate system:

$$X = a(\cos E - e)$$

$$Y = a\sqrt{1-e^2} \sin E$$

$$Z = 0$$

where a is the semi-major axis and e the eccentricity. The eccentric anomaly is related to time by Kepler's equation:

$$M(t - T) = E - e \sin E$$

where T = time of perifocal passage has been set equal to zero for the sake of simplicity. $E = E(t)$ is obtained by use of Newton's method for approximating roots of a transcendental equation. This effectively gives the position (and velocity) of the satellite as an explicit function of time in a geocentric rectangular coordinate system. This coordinate system is then successively transformed to a coordinate system centered at the station site and aligned parallel to the coordinate system of the antenna. Once this is accomplished, we are able to describe analytically the angle velocities and accelerations with little difficulty.

A Fortran II program has been written for the IBM 1620 to perform the required computations. The program requires the following inputs:

GM_e = gravitational constant (Earth)

ω = Earth rotation rate

R_e = Earth radius

ϕ = station latitude

a = semi-major axis

e = eccentricity

Ω = longitude of ascending node

ω = argument of perifocus

$i, \Delta i, K$ = orbital inclination

$t, \Delta t, N$ = time

H. Computer Programs

1. Satellite Rate Program

It is sometimes necessary to ascertain whether the angular velocity and acceleration encountered in a ha-dec antenna tracking an Earth satellite in any given orbit will violate the physical limitations placed on the antenna. The orbits to which this study is directed are generally described in terms of the classical elements. The problem then becomes: Given the classical elements of an Earth satellite, what are the declination velocity and

A beginning time (t), an incremental time (Δt), and a number of times incremented (N) is input, thus allowing the user to sample any portion of the orbit with whatever frequency is needed. A beginning inclination (i), an incremental inclination (Δi), and a number of times incremented (K) provide the capability of testing a given orbit at different inclinations, thus finding the maximum inclination for which the angular velocity and acceleration are within given limits for tracking a satellite in an otherwise fixed orbit. Computation is executed as shown in Fig. 13.

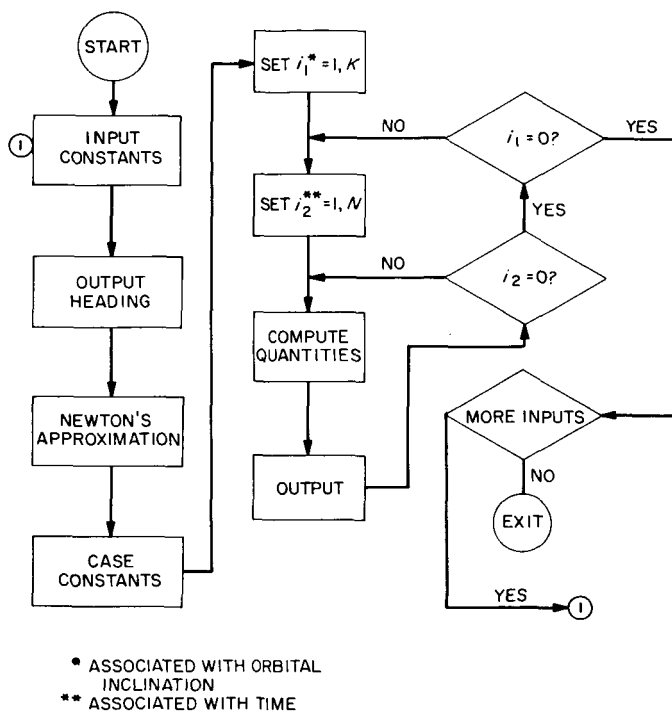


Fig. 13. Flow diagram

The program outputs the following quantities with appropriate headings:

t = time

α = hour angle

$\dot{\alpha}$ = hour angle velocity

$\ddot{\alpha}$ = hour angle acceleration

β = declination

$\dot{\beta}$ = declination velocity

$\ddot{\beta}$ = declination acceleration

ρ = range

$\dot{\rho}$ = range velocity

$\ddot{\rho}$ = range acceleration

2. DSIF Tracking Data Analysis

The TDA facility has recently been updated by the acquisition of a Scientific Data Systems (SDS) 920 digital computer. Interface electronics are presently being built which will allow direct teletype information inputs to the computer and direct outputs to a Benson-Lehner (B-L) Model J point plotter.

a. SDS 920 computer. The SDS 920 is a small, high-speed, general purpose digital computer. Core memory is comprised of 4096 24-bit words. The standard input/output devices consist of a paper tape reader/punch unit, alpha numeric typewriter, and two 15-kc magnetic tape units. Special purpose input/output devices consist of 16 channels of priority interrupt, two channels of direct teletype input, and one channel of direct plotter output.

b. Benson-Lehner plotter. The B-L Model J point plotter has the capability to plot data from paper tape or from the SDS computer. Seven individual graphs may be plotted per pass with variable scale factors and origin offsets available for each graph.

Tracking data is reduced through use of a computer program which utilizes the input/output capabilities of the TDA facility listed above. This program is comprised of three distinct computational areas, which are: (1) comparison of predicted data to actual tracking data received, (2) computation of doppler variance, and (3) data condition code log. Implementation of the program has begun with coding of the basic input, conversion, and executive control subroutines being performed at the present time. The input and conversion subroutines are checked out and operational. The input subroutine (RDTTY) will accept teletype data from paper tape or by direct electronic input. The data will be stored in a core storage input buffer until a carriage return (CR) character is encountered. This CR character initiates a buffer check and conversion subroutine (BCC). The BCC subroutine converts the input buffer storage area into separate data words for use by the computational areas of the program. The executive control subroutine (EXC) exercises (through sense switch control) the required options to be performed.

3. Stereographic Projection Program

In the past, the use of stereographic station projections has proved to be a valuable aid in visualizing tracking problems and analyzing space trajectory-antenna relationships. However, the production of originals for these projections for the older DSIF Stations has always been a laborious and time-consuming task. Previously, parameters were computed and given to a draftsman, who in turn plotted the curves manually. Each plot required approximately a month for completion. With the acquisition of new DSIF antenna sites and the necessity for revisions on the older plots, it became clear that some means of simplifying and expediting the production of stereographic station projections was needed. As a result, a *Fortran* computer program has been written for the SDS 920 system to output $\bar{X}\bar{Y}$ -coordinates for the hour angle-declination intersections superimposed on the corresponding coordinates of the azimuth-elevation system for an arbitrary station location.

A program is now being written as a supplement to punch these X - and Y -values on paper tape to be used in the Benson-Lehner plotter.

Eventually, the computer will be tied into the plotter with no supplement program needed, but at present this describes the system that will be utilized.

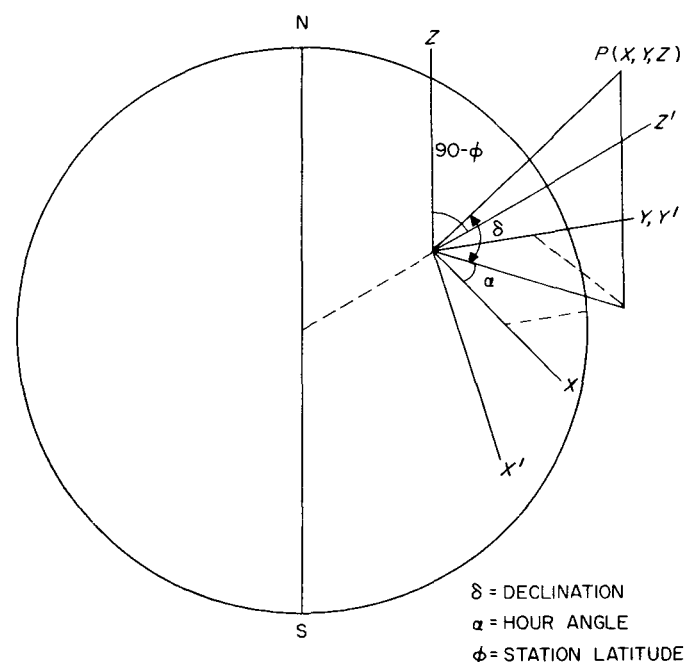


Fig. 14. Celestial coordinate system

The equations were derived by taking a point $P(X, Y, Z)$ in an XYZ -system with the Z -axis parallel to the Earth's rotational axis and the Y -axis pointing positive east.

Rotate the coordinate system $90 - \phi$ deg around the Y -axis where ϕ is the station latitude.

Assuming the line connecting the origin and $P(X, Y, Z)$ to be a unit vector:

$$X = \cos \delta \cos \alpha \quad (1)$$

$$Y = -\cos \delta \sin \alpha \quad (2)$$

$$Z = \sin \delta \quad (3)$$

$$\begin{pmatrix} X' \\ Y' \\ Z' \end{pmatrix} = \begin{pmatrix} \sin \phi & 0 & -\cos \phi \\ 0 & 1 & 0 \\ \cos \phi & 0 & \sin \phi \end{pmatrix} \begin{pmatrix} X = \cos \delta \cos \alpha \\ Y = -\cos \delta \sin \alpha \\ Z = \sin \delta \end{pmatrix} \quad (4)$$

$$= \begin{pmatrix} \cos \delta \cos \alpha \sin \phi - \sin \delta \cos \phi \\ -\cos \delta \sin \alpha \\ \cos \delta \cos \alpha \cos \phi + \sin \delta \sin \phi \end{pmatrix} \quad (\text{Fig. 14})$$

Projection onto the XY plane

$$\sin \gamma = Z' = \cos \bar{\gamma}, \text{ where: } \bar{\gamma} = 90^\circ - \gamma$$

$$R = 2 \tan \frac{\bar{\gamma}}{2} = 2 \left(\frac{1 - \cos \bar{\gamma}}{1 + \cos \bar{\gamma}} \right)^{1/2}$$

$$R = 2 \left(\frac{1 - Z'}{1 + Z'} \right)^{1/2} \quad (5)$$

$$\bar{X} = R \cos \sigma; \quad \cos \sigma = \frac{X'}{(X'^2 + Y'^2)^{1/2}} \quad (\text{Fig. 15})$$

$$\bar{Y} = R \sin \sigma; \quad \sin \sigma = \frac{Y'}{(X'^2 + Y'^2)^{1/2}}$$

$$\text{But } (X'^2 + Y'^2)^{1/2} = \cos \gamma = (1 - Z'^2)^{1/2}$$

$$\bar{X} = R_0 \left(\frac{1 - Z'}{1 + Z'} \right)^{1/2} \cdot \frac{X'}{(1 - Z'^2)^{1/2}} = R_0 \frac{X'}{1 + Z'} \quad (6)$$

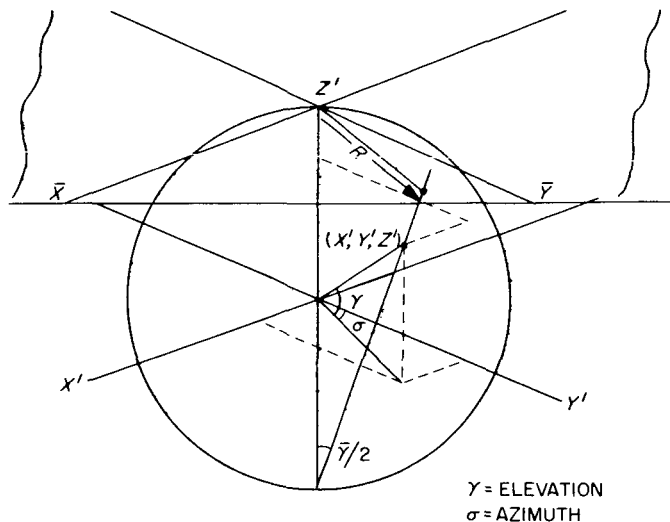


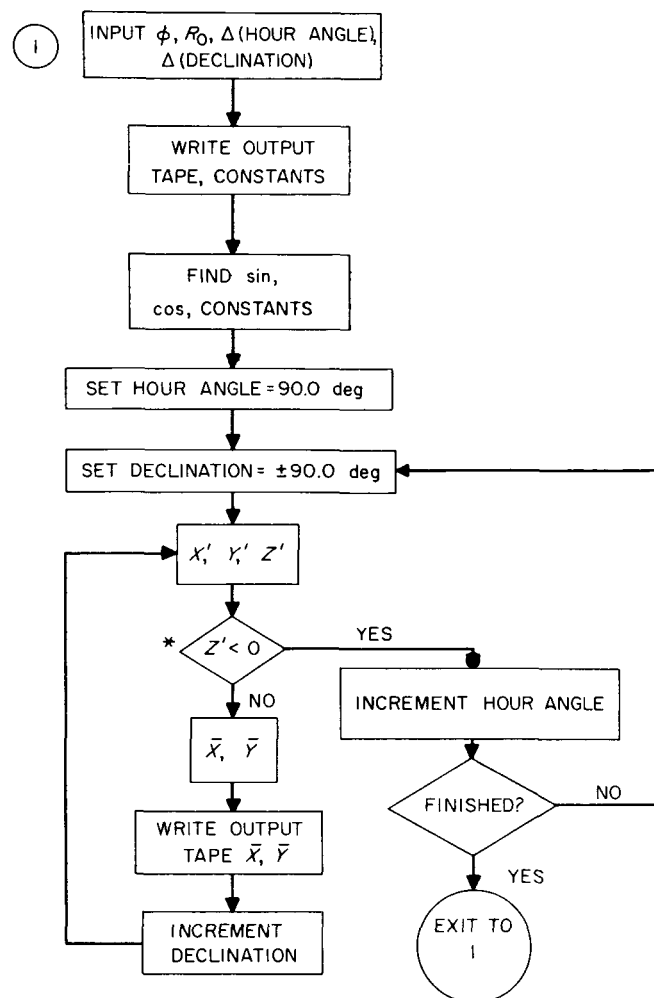
Fig. 15. Stereographic coordinate system

$$\bar{Y} = R_0 \left(\frac{1 - Z'}{1 + Z'} \right)^{1/2} \cdot \frac{Y'}{(1 - Z'^2)^{1/2}} = R_0 \frac{Y'}{1 + Z'} \quad (7)$$

where R_0 is the desired map radius.

The coordinate system was then oriented to coincide with the conventional XY system by letting $\bar{X} = \bar{Y}$ and $\bar{Y} = -\bar{X}$. This had the effect of rotating the system 90 deg in a counter-clockwise direction. This left Y positive north and X positive east.

A flow diagram of the *Fortran* program is shown in Fig. 16. After the input procedure, α is incremented and all values of δ are computed on those values which lie within the prescribed horizon limit. This is done for the α 's ranging from $+90^\circ$ to -90° .



* THE GEOMETRICAL HORIZON LIMITATION TAKES THE FORM $Z' = \sin \gamma \geq 0$

Fig. 16. Fortran program flow diagram

References

1. Meggitt, J. E., "Error Correcting Codes and Their Implementation for Data Transmission Systems," *IRE Transactions on Information Theory*, pp. 234-244, October 1961.
2. Abramson, N. M., "Error Correcting Codes from Linear Sequential Circuits," Technical Report No. 2002-1, Stanford Electronics Laboratories, Stanford University, Stanford, California, June 13, 1960.
3. Fire, P., "A Class of Multiple-Error-Correcting Binary Codes for Non-Independent Errors," Technical Report No. 55, Stanford Electronics Laboratories, Stanford University, Stanford, California, April 24, 1959.

References (Cont'd)

4. Elspas, B., and Short, R. A., "A Note on Optimum Burst-Error-Correcting Codes," *IRE Transactions on Information Theory*, IT-8, pp. 39-42, January 1962.
5. Perlman, M., "Implementation of Error Detection and Correction Using Binary Cyclic Codes (Part 1)," Technical Report No. 32-324, Jet Propulsion Laboratory, Pasadena, California, October 1, 1962.
6. Fontaine, A. B., "Error Statistics and Coding for Digital Data Transmission over Telephone and Teletype Circuits," Report 25G-14, Lincoln Laboratory, Massachusetts Institute of Technology, Lexington, Massachusetts, January 21, 1963.
7. "IRIG Telemetry Standards," IRIG Document No. 106-60, November 1960.
8. Patterson, D. G., "Analysis of Communication Line Failure Data," Technical Memorandum No. 316-31, Jet Propulsion Laboratory, Pasadena, California, July 30, 1962.
9. Johnson, M. S., and Helms, J. F., "Communications Reliability," Technical Memorandum No. 316-85, Jet Propulsion Laboratory, Pasadena, California, April 22, 1963.
10. Helms, J. F., "Communication Reliability," Technical Memorandum No. 316-101, Jet Propulsion Laboratory, Pasadena, California, July 11, 1963.
11. Peterson, W. W., "Error Correcting Codes," MIT Press and John Wiley and Sons, Inc., 1961.
12. Gilbert, E. N., "Synchronization of Binary Messages," *IRE Transactions*, IT-6, pp. 470-477, September 1960.
13. Holdridge, D. B., "Space Trajectories Program for the IBM 7090 Computer," Technical Report No. 32-223, Jet Propulsion Laboratory, Pasadena, California, September 1, 1962.
14. Mudgway, D., "A Radio Frequency Interference Control Plan for the DSIF," Engineering Planning Document No. 169, Jet Propulsion Laboratory, Pasadena, California, June 21, 1963.
15. "Surveyor Spacecraft/DSIF System Interface Requirements," *Surveyor Project Control Document*, Project Document No. 6, July 29, 1963.

IV. Research and Development

A. Ground Antennas

1. Radio Astronomical Techniques for Ground Antenna Calibration

a. Boresight and gain calibrations for DSIF antennas.

Summary. We have been working on techniques for calibrating the gain and pointing of the large ground antennas in the DSIF. In SPS 37-22 a preliminary description of an automatic radio-astronomical drift curve calibration technique was presented. The work on automatic radio star drift curve calibrations has continued. On the night of June 22, 9 hr of drift curve data were obtained using the techniques described in SPS 37-22, Vol. III, pp. 22-25. The data were recorded on punched tape, transcribed onto IBM cards, and then reduced on an IBM 1620 computer. Declination and hour angles errors as well as relative source antenna temperature were obtained as a function of hour angle.

Recent work. The digital computer programs have been completed, and data obtained from the radio source Cygnus A on June 22 were reduced. The Cygnus A data were obtained using the 2295-Mc Dicke radiometer (described in SPS 37-18, Vol. III) installed on the Echo site

85-ft antenna. The DSIF preprototype S-band cassegrain monopulse feed was used for the experiments.

Prior to the actual experiment a schedule of hour angle and declination steps as a function of time was prepared. The antenna was moved from one fixed position to the next every 15 min. The hour angle steps were about $3\frac{1}{4}$ deg, manually controlled; a declination raster scan scheme was employed after initial checkout so that the declination was automatically stepped by 0.1 deg.

Before taking drift curves, it was necessary to calibrate the noise tube. This was done by placing a well matched nitrogen load at the antenna input that gave a frequency from the voltage-to-frequency converter which was a function of the input temperature of the load $86 \pm 2^\circ\text{K}$ (Fig. 1). With the nitrogen load connected to the input circulator, the gas tube relay was switched so that the input temperature was increased and the change in output frequency was measured. The nitrogen load was then replaced by an ambient load and the sequence repeated. Thus, the frequency temperature proportionality constant is obtained and the effective temperature of the noise tube is calculated. The linearity of the system is verified by comparing the change in output produced by the gas tube at liquid nitrogen and ambient input temperatures.

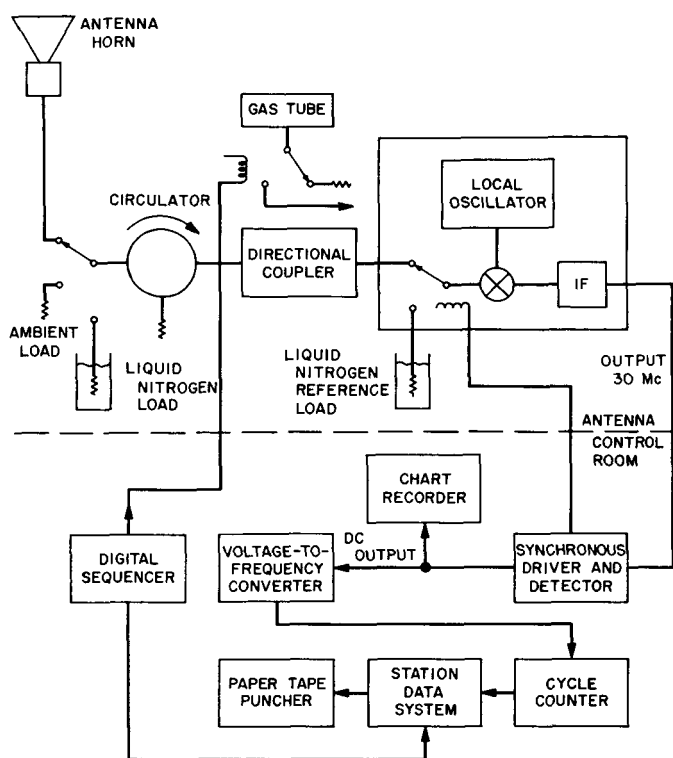


Fig. 1. Digital radio astronomy system

After calibrating the gas tube, the radiometer is reconnected to the antenna transmission line as shown in the block diagram (Fig. 1).

The antenna input and a nitrogen load input are chopped in a synchronous manner so that the signal going into the mixer is a noise signal with a squarewave audio modulation at the chopping frequency. The amplitude of the modulation is a function of the temperature difference between the antenna and the reference load. The noise signal is amplified and then synchronously detected. The output of the synchronous detector is fed to a chart recorder and a voltage-to-frequency converter. The audio frequency produced by the converter is then treated by the standard station data system in the same manner as the doppler frequency is normally handled. A paper tape is prepared containing station ID, data type, time, hour angle, declination, frequency, and day number.

The paper tape is converted to punched cards for later reduction on the IBM 1620. A sequencing device described in SPS 37-20 is used to control the gas tube, the data type number, and a bell which reminds the servo operator when it is antenna hour angle position stepping time. It was found that the scheme of firing the gas tube for each calibration was not sufficiently reliable, so the

system was changed to fire the noise tube continuously and use a coaxial relay to control injection of the noise signal.

Two digital computer programs have been prepared for the reduction of the drift curve data. The first program accepts the station data output in the form of punched cards. In addition to the station data, source ephemeris information is provided.

The computer first calculates the predicted crossing time for the actual hour angle setting taking into consideration refractive errors. Next, the baseline points at the beginning and end of the run are used to make a linear correction for baseline drift. Then, a scale factor in cycles per degree is obtained by comparing the baseline with the gas tube calibrations; the gas tube effective temperature has been entered as one of the program inputs.

The computer then selects those readings which fall within the 3-db beamwidth of the predicted source location. A fourth power polynomial least square fit is made to these points. The standard deviation is examined and all points whose variance is greater than 2.5σ are discarded. The crossing time and relative temperature of the drift curve are computed. The results of this program are then punched out on cards. This first program completely fills a 40,000-bit IBM 1620 so that a second program was necessary to use successive drift curves to obtain declination boresight errors and maximum antenna temperature.

The second program takes the outputs of the first program (declination raster offset, elevation, hour angle, maximum drift curve temperature). The temperature of each curve is corrected for atmospheric extinction by using a table lookup subroutine based on atmospheric attenuation predictions (Ref. 1). The first four temperatures are fitted to a second power polynomial as a function of declination offset. The polynomial maximum gives the antenna temperature and the declination boresight error which are punched out. After the polynomial is obtained, the first point is dropped and a fifth point is used to compute a new polynomial. This procedure is repeated for each successive drift curve. The results are smoothed curves of declination error and temperature as a function of hour angle. Fig. 2 shows the declination raster scan, antenna temperature, declination error, and hour angle error for Cygnus A obtained on June 22. The antenna temperature, and therefore the gain, can be seen to vary as a function of hour angle with a maximum at 0° .

The technique appears to be quite promising and further antenna schedule time will be sought to develop and evaluate the procedures more thoroughly.

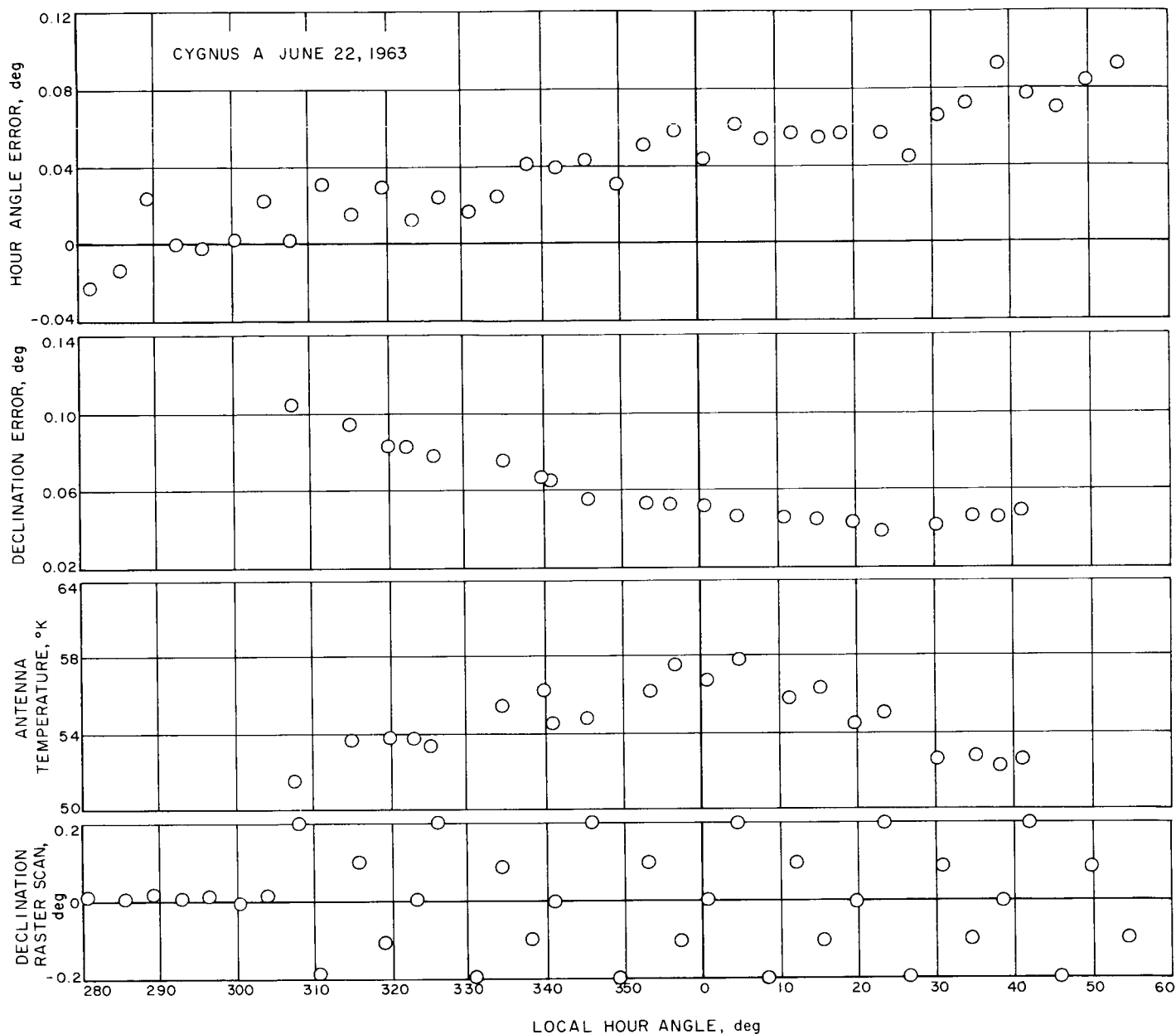


Fig. 2. Declination error, hour angle error, antenna temperature, and raster scan of a function of hour angle (Echo site 85-ft antenna)

b. Experimental antenna radiometric tests.

Summary. A program to calibrate the Goldstone 30-ft az-el antenna by radio-astronomical techniques has been undertaken. The measurements will be made at X-band (8448 Mc). They are complementary to the X-band measurements being made using the Tiefert Mountain antenna range. (See Section IV-A-2 of this report.) An operational X-band radiometer has been constructed and tested; it will be used on the 30-ft antenna to measure the mini-

um antenna temperature and to measure the temperatures of known radio sources, including the Sun and Moon.

In addition to their direct relation to the detailed 30-ft antenna measurement program, the radiometric measurements are expected to provide useful information on the application of X-band frequencies to space communications. When analyzed in conjunction with previous S-band

results from the 85-ft az-el antenna, the X-band measurements will lead to determinations of absolute source flux densities and spectra.

The resolution of the radiometer, as determined by preliminary measurements, is $\frac{1}{2}$ to 1°K in a system temperature of approximately 700°K .

Recent work.

Radiometer and waveguide system. The X-band radiometer, shown in Figs. 3 and 4, is a total-power radiometer having a gain of 115 db and an IF bandwidth of 6.5 Mc. The noise figure of the radiometer, operated double-sideband, is $3.7 \text{ db} \pm 0.5 \text{ db}$, including the circulator loss of 0.1 db. This was measured on a Hewlett-Packard Model 340B noise figure meter with an ambient load on the radiometer input. This corresponds to a total radiometer noise temperature of $680 \pm 80^\circ\text{K}$. The IF center frequency is 10 Mc; thus, the bandwidth requirements of the waveguide system are easier to meet than with a 30-Mc double sideband IF system. The 3-db bandwidth requirement for the waveguide system is 31 Mc; however, the limiting factor is not the guide itself but the dual-mode horn which should be well matched ($\text{VSWR} \leq 1.05$) over this frequency range.

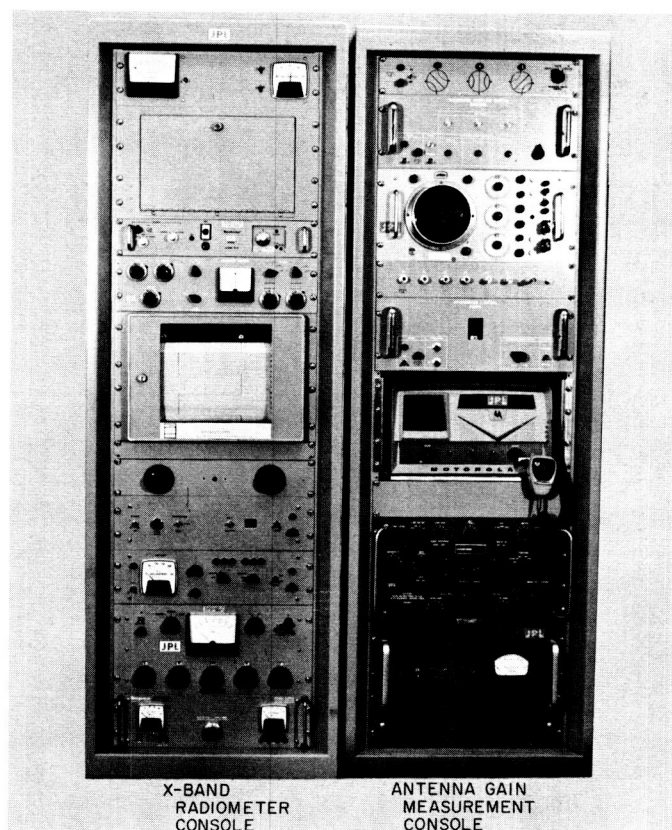


Fig. 3. X-band radiometer console

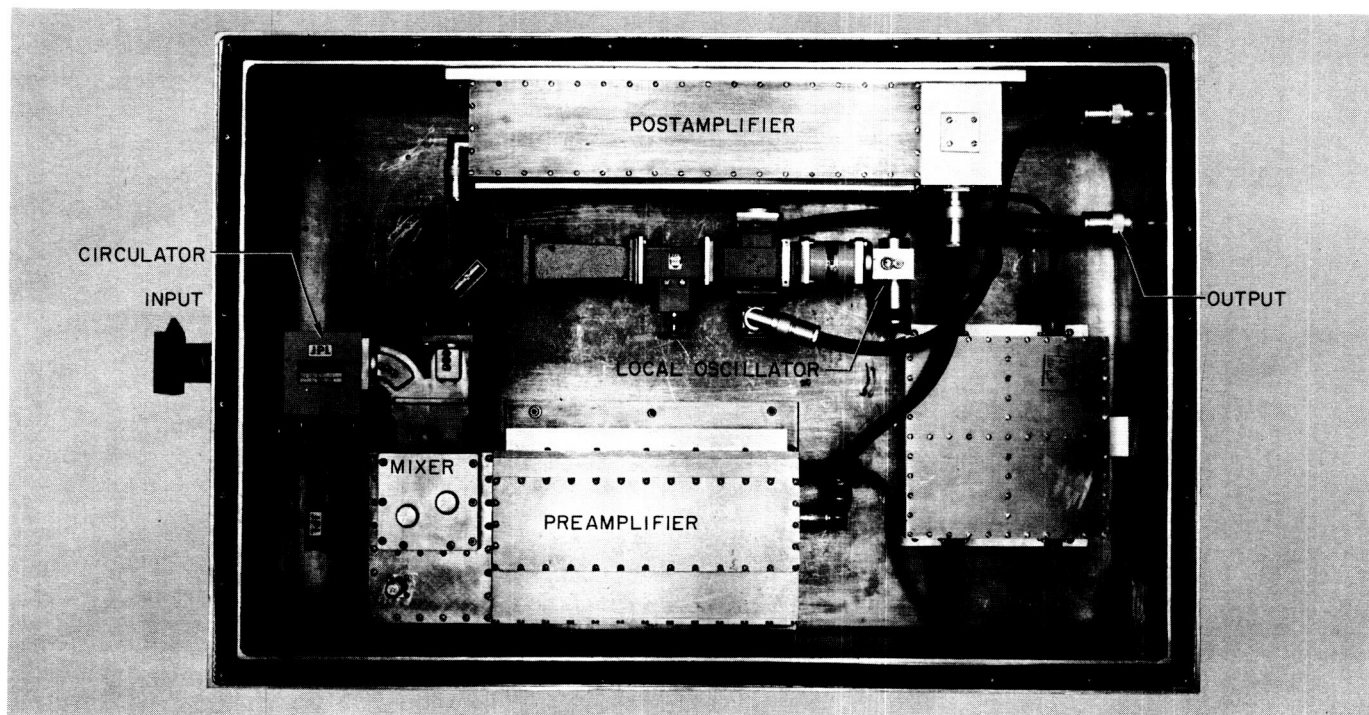


Fig. 4. X-band radiometer box

The waveguide system consists almost exclusively of WR 112 (large X-band) waveguide with carefully lapped straight-through cover flanges (Fig. 5). Milled-back flanges add two more discontinuities to each waveguide joint, and thus increase the insertion loss of the transmission line system. For this reason they are not used.

The X-band dual mode conical horn and the Cassegrain secondary reflector are scale models of the S-band system used on the 85-ft az-el antenna at the Venus site. Fig. 6 shows the horn in the Cassegrain cone. The waveguide system between the horn and the radiometer is mounted in the cone, and the radiometer box is mounted on the transmitter cage behind the reflector backup structure. The small horn has an unmatched VSWR of about 1.3 which must be compensated for with a three-stub tuner (Fig. 5).

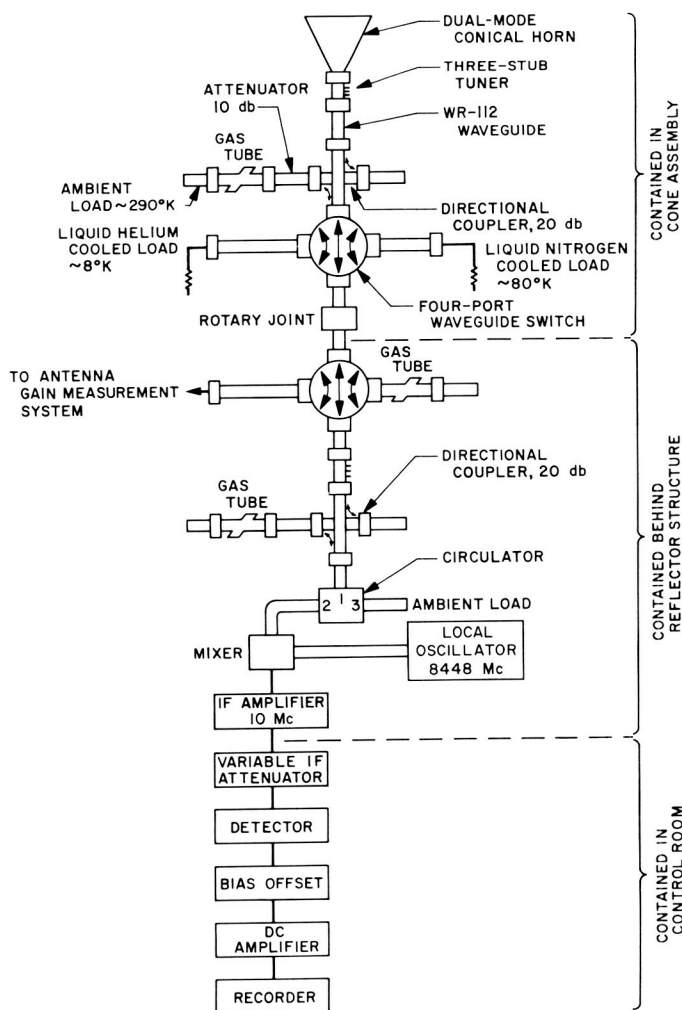


Fig. 5. Block diagram of calibration system and radiometer

The 10-Mc IF contains seven 6688 pentode stages, two 417 cathode followers terminating the preamplifier and postamplifier, and a Wallman Cascode preamplifier consisting of 437 and 417 triodes (Ref. 2).

The IF amplifiers are very sensitive to changes in B+ and filament voltage. A 15-mv change in B+ voltage results in a radiometer gain change of 1°K in a 700°K system, or about 0.006 db. A filament voltage change of only 1 mv will also cause a 1°K gain change. Because

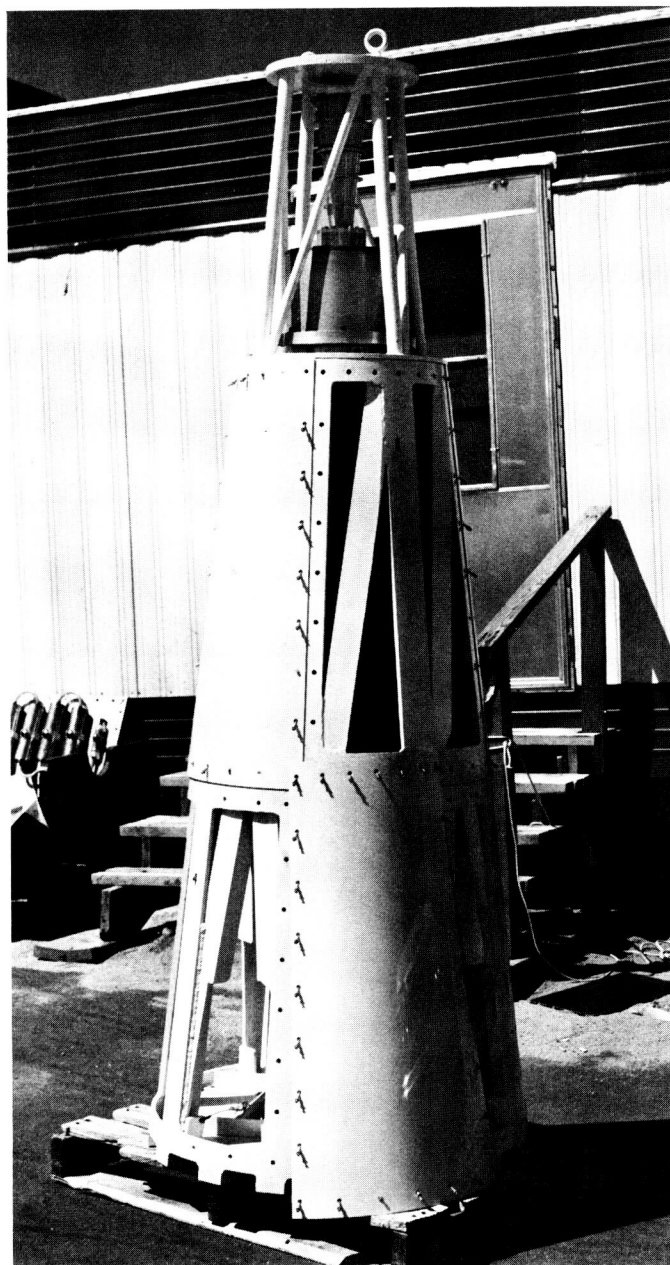


Fig. 6. Cassegrain cone assembly

of this sensitivity we have reworked the filament supply to bypass the built-in reference zener diode; and we have installed a new reference diode in a temperature controlled oven. A remote sensor on the dc filament supply to control the voltage in the radiometer box, rather than in the control room, has been installed on the antenna. This will compensate for changes in voltage in the filament power cable due to changes in cable temperature. For a 10°C temperature change in 1000 ft of the No. 4 copper wire being used, we will experience a filament voltage change of about 30 mv. We are presently still experiencing a gain instability of $\pm 1^\circ\text{K}$, which we attribute to the mixer diodes and local oscillator drive variations. Further selection of mixer crystals and planned improvements in local oscillator performance should reduce the instabilities. Use of a Hewlett-Packard Model 620 signal generator as a local oscillator instead of a Trak Model 9127 microwave oscillator reduces the peak-to-peak noise jitter by about $\frac{1}{4}^\circ\text{K}$ in a 1°K jitter.

The noise temperature fluctuations (ΔT) at the output of the radiometer can be represented as composed of two sources: (1) thermal noise jitter ($T_s/\sqrt{B\tau}$) and (2) radiometer gain instability [$(\Delta G/G)T_s$], where

T_s = system temperature

B = predetection system bandwidth

τ = postdetection integration time

ΔG = gain change of radiometer

G = gain of radiometer

The integrated rms value of fluctuations will be the quadratic sum of the two contributions;

$$\Delta T_{rms} = T_s \left[\frac{1}{B\tau} + \left(\frac{\Delta G}{G} \right)^2 \right]^{1/2}$$

Fig. 7 is a radiometer recorder chart showing the effect of time constant on system noise temperature fluctuations. A change in time constant from 1 to 4 sec only reduces the peak-to-peak noise temperature fluctuations in the recorder output from about $1\frac{1}{2}^\circ\text{K}$ to about 1°K . This indicates that we need to work on reducing both causes of noise temperature fluctuations noted above. The figure shows that the present short term gain instability is about 1°K peak-to-peak in a period of about 15 sec.

Thermal noise jitter of about 1°K does not present a major impediment to data analysis as long as the gain instability is much less than this. The long term baseline

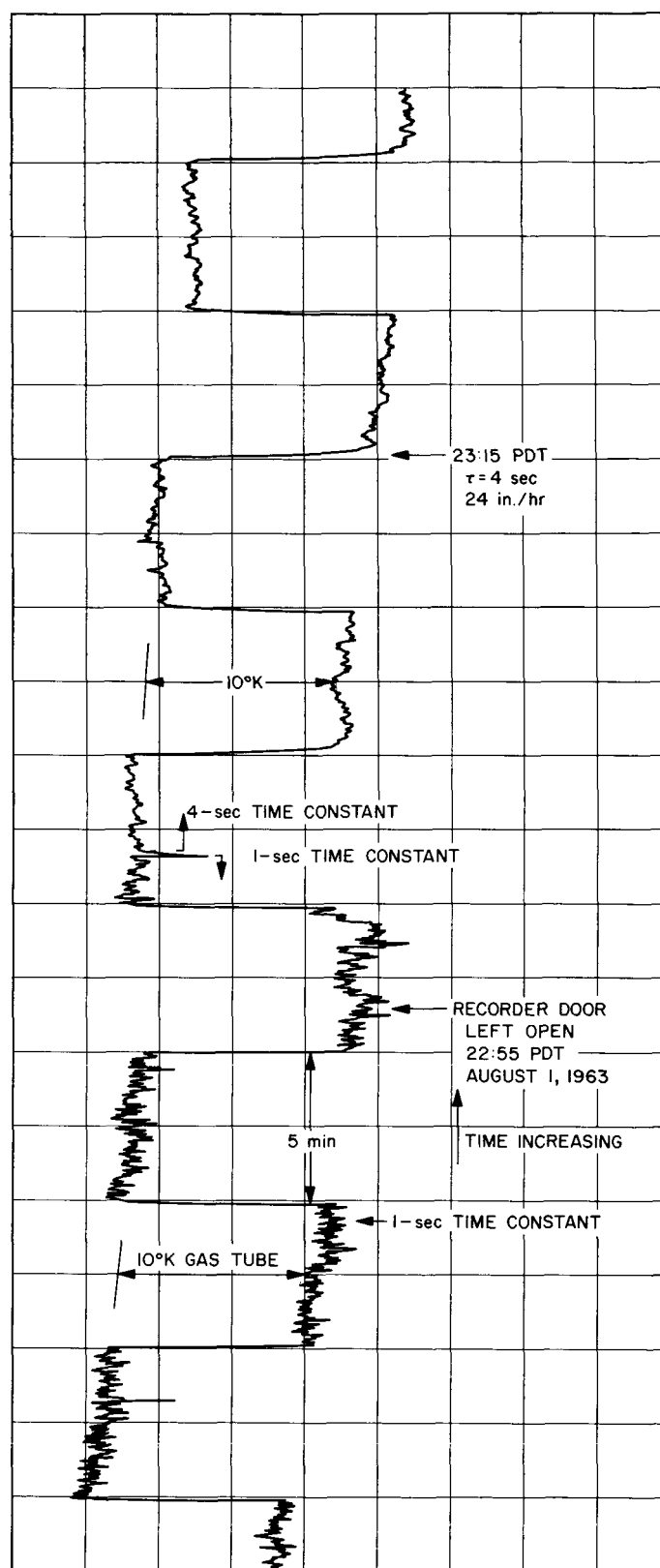


Fig. 7. Recording of X-band radiometer

drift as indicated in this record amounts to about 3°K in $\frac{1}{2}$ hr.

An examination of Fig. 5 will indicate how the noise temperature of the various gas tubes and the antenna temperature may be determined. By switching between ambient, nitrogen, and helium loads, the antenna, and the three gas tubes, and by moving the 10-db attenuator from one gas tube to the other, we can, by a series of simultaneous source contribution equations, solve for the unknowns in several ways. We expect to report on preliminary temperature measurements and their absolute accuracy in the next *Summary*.

2. Radiation Pattern and Antenna Efficiency Computer Studies

a. Summary. Two studies are currently being conducted, using the IBM 7094 computer, to numerically evaluate the scalar far-field radiation pattern integral and aperture efficiency of paraboloid reflector antennas. Both programs are operative and some preliminary studies have been completed.

The radiation pattern program is being initially utilized in connection with present tests on the 30-ft az-el antenna. Computed results including aperture blocking by the subreflector and quadripod are given and are compared with experimental azimuth and elevation patterns.

The antenna efficiency program is described. Results of one test case to evaluate the accuracy of the calculation are given; the spillover and aperture efficiency for the 30-ft az-el are calculated.

b. Recent work.

Radiation pattern computer program. Computer studies are being conducted in an attempt to resolve discrepancies between predicted and experimental pattern results on the 30-ft antenna at 8450 Mc. Two interrelated studies have been performed during the last period:

- (1) Increasing the number of aperture radii of integration and/or the number of aperture azimuthal angles of integration, NR and $N\beta$, respectively, in an attempt to improve the accuracy of the predicted patterns.
- (2) Including the blocking caused by the hyperboloid subreflector and support (quadripod) members.

Previous investigations (SPS 37-21, Vol. III) utilized illumination and surface deviation functions defined for 14 radii of integration (NR) and 16 azimuthal angles of

integration ($N\beta$) resulting in 224 aperture points of integration. Subsequent work has utilized $(NR)(N\beta)$ products ranging from 512 to 4,860, a total range of more than 20:1.

Because these test cases utilized an axially symmetric feed illumination, increasing $N\beta$ for a given NR produced essentially no change in computed patterns with the exception of relatively wide angles ($\theta > 15$ full half power beamwidths). Furthermore, these test cases assumed perfect surface paraboloids. Cases involving distorted reflector surfaces may well show the $N\beta$ dependence more clearly.

Variations in NR for a given $N\beta$ produced significant changes in computed patterns comparatively close in to the main beam ($\theta \geq 4$ full half power beamwidths). In general, predicted levels became more accurate in direct proportion to NR .

Unfortunately, this program nearly saturates the 32K word capacity of the 7094 when arrays of 27×180 size are used; thus, preliminary accuracy limits, without resorting to reprogramming to use magnetic tape storage equipment, appear to be ≈ 1 db ($0 < \theta < 5$ full half power beamwidths), ≈ 5 db ($5 < \theta < 10$ full half power beamwidths), and questionable thereafter for arrays of

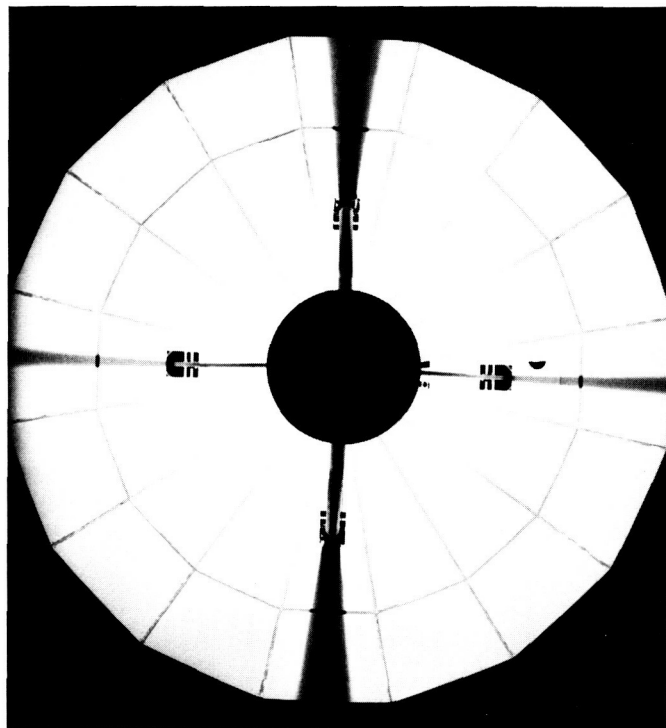


Fig. 8. 30-ft az-el, optical illumination

maximum size with some dependence upon details of the individual case, i.e., absence or presence of unsymmetrical reflector surface, feed phase, and feed amplitude arrays.

Aperture blocking has been handled on an approximate (optical) basis by assigning zero intensity to the appropriate regions of the amplitude array. Fig. 8 shows the 30-ft az-el illuminated with a 500-w floodlight placed near the horn. As can be seen in this figure, the subreflector scattered light optically over the paraboloid surface. Clearly defined is the subreflector (and 6-ft gain standard) and the quadripod legs with their associated shadows. It will be noted from Fig. 8 that two types of structural members are used in this installation. Because the two members represent obstacles having minimum dimensions in the order of 2 and 6 wavelengths, the optical approximation is not totally unreasonable. Furthermore, it is to be expected that this antenna will exhibit secondary patterns having some polarization de-

pendence as well as different azimuth and elevation patterns, especially in the sidelobe region, as a result of the quadripod asymmetry alone.

Figs. 9 and 10 show, respectively, azimuth and elevation patterns for two computed cases and experimental data. The spread in experimental data represents observed polarization dependence as previously discussed. Case A was computed accounting for subreflector blocking only; hence, the azimuth and elevation predictions are identical. Case B was computed accounting for subreflector and quadripod blocking. The azimuth and elevation predictions show some difference as will be noted in the region of $\theta = 1.60$ deg. Both computed cases used experimentally determined feed amplitude and phase input. The reflector surface was assumed perfect ($DZ = 0$) with $NR = 27$, $N\beta = 180$. That the reflector is perfect is somewhat in error as will be seen in SPS 37-20, Vol. III, p. 30, Fig. 7. The experimental patterns shown were taken with the reflector panels set for optimum 5-deg

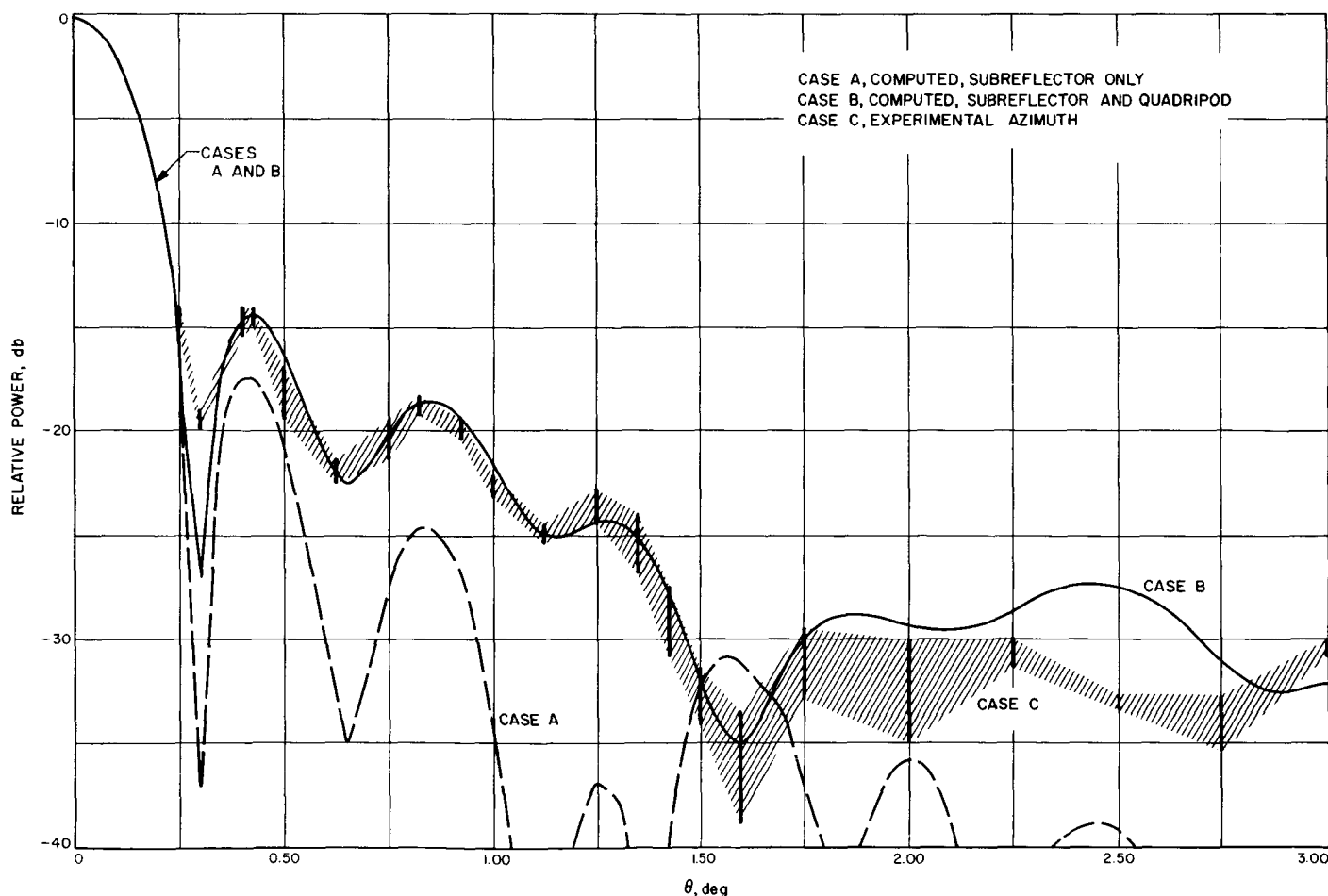


Fig. 9. 30-ft az-el azimuth pattern, 8450 Mc

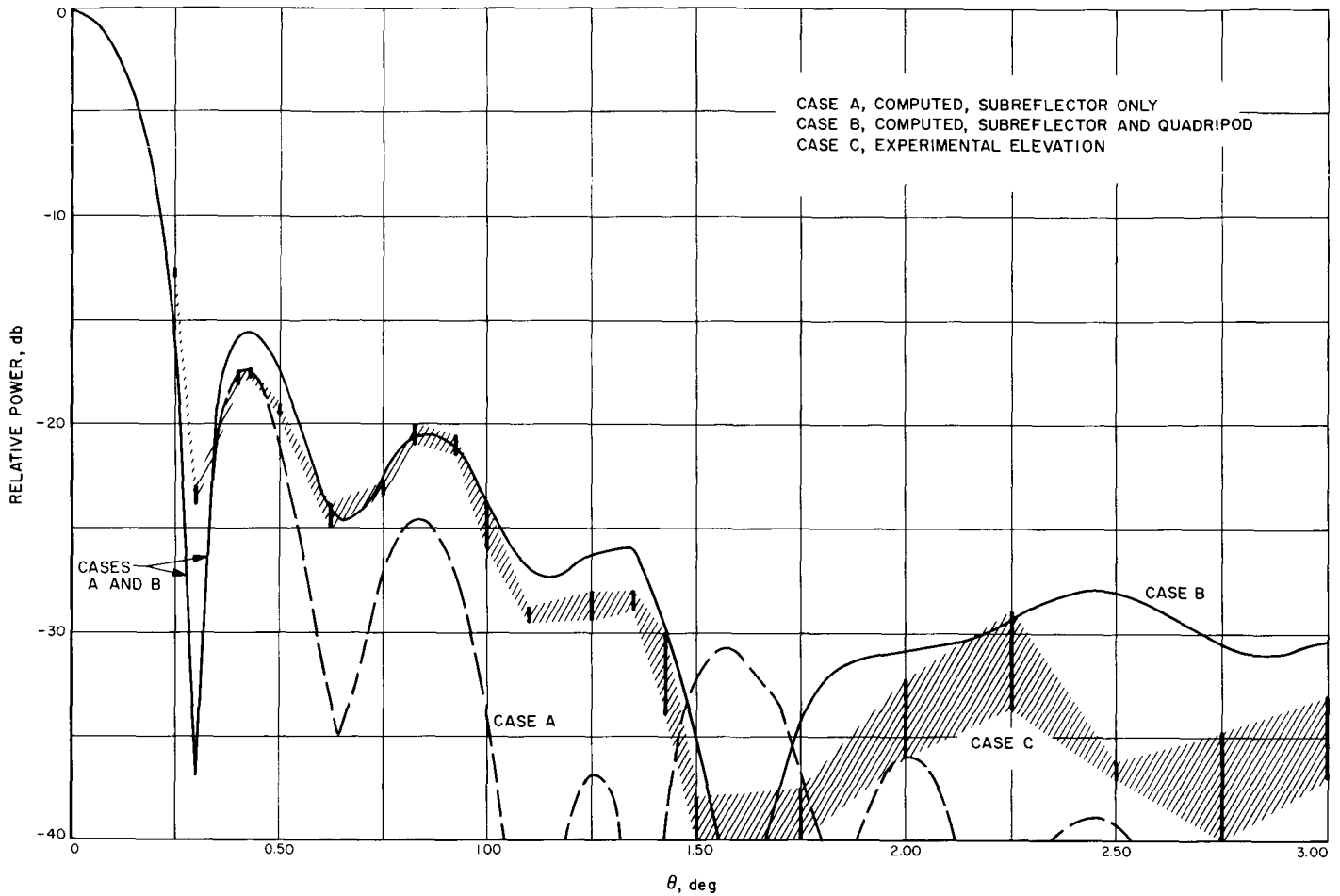


Fig. 10. 30-ft az-el elevation pattern, 8450 Mc

elevation orientation. Additional main beam broadening at low levels, as well as null filling, will be the predicted result if the actual deflections are included in the computations, based on previous work (SPS 37-21, Vol. III).

In general, the computed Case B results compared with the experimental data are considered encouraging evidence of the validity of the program as well as showing the significant role of the quadripod structure upon side-lobe level and distribution. As shown in the following article, the quadripod is also significant in determination of aperture efficiency.

Antenna efficiency computer program. Previous work (SPS 37-15, Vol. III) has shown the desirability of evaluation, by digital computer, of aperture efficiency and some related factors such as spillover, cross-polarization loss, and noise temperature. A new program written for an IBM 7094 includes these effects while accounting for aperture blocking by an approximate (optical) method.

The efficiency with which a feed illuminates an aperture of edge angle Ψ in the absence of cross-polarization loss, phase errors, and blocking has been shown to be (Ref. 3)

$$\eta = \frac{1}{4\pi^2} \cot^2\left(\frac{\Psi}{2}\right) \left| \int_0^{2\pi} \int_0^\Psi [G_f(\psi, \xi)]^{1/2} \tan \frac{\psi}{2} d\psi d\xi \right|^2 \quad (1)$$

where $G_f(\psi, \xi)$ is the illumination gain function defined as the ratio of radiated power in a given direction per unit solid angle, to the average power radiated per unit solid angle, and is related to the field-strength feed pattern as

$$G_f(\psi, \xi) \equiv \frac{P_f(\psi, \xi)}{P_T/4\pi} = \frac{4\pi [E_f(\psi, \xi)]^2}{\int_0^{2\pi} \int_0^\pi [E_f(\psi, \xi)]^2 \sin \psi d\psi d\xi} \quad (2)$$

Assuming the feed patterns to be axially symmetric or, by averaging, Eqs. (1) and (2) give

$$\eta = 2 \cot^2 \left(\frac{\Psi}{2} \right) \frac{\left| \int_0^{\Psi} E_f(\psi) \tan \left(\frac{\psi}{2} \right) d\psi \right|^2}{\int_0^{\pi} [E_f(\psi)]^2 \sin \psi d\psi} \quad (3)$$

The denominator of Eq. (3) can be separated to handle all energy radiated by the feed:

$$\begin{aligned} \int_0^{\pi} [E_f(\psi)]^2 \sin \psi d\psi &= \int_0^{\Psi} [E_f(\psi)]^2 \sin \psi d\psi \\ &+ \int_{\Psi}^{\pi/2} [E_f(\psi)]^2 \sin \psi d\psi + \int_{\pi/2}^{\pi} [E_f(\psi)]^2 \sin \psi d\psi \\ &+ \int_0^{\Psi} [E_{xf}(\psi)]^2 \sin \psi d\psi + \int_{\Psi}^{\pi/2} [E_{xf}(\psi)]^2 \sin \psi d\psi \\ &+ \int_{\pi/2}^{\pi} [E_{xf}(\psi)]^2 \sin \psi d\psi \end{aligned} \quad (4)$$

where $E_{xf}(\psi)$ is the cross-polarized field-strength feed pattern.

Blocking calculations based on geometric optics theory, useful only when the obstacle is large compared with the wavelength, have been formulated for some simple obstructions such as axially symmetric circles and rings, wedges and arbitrary areas (fractional rings). Fig. 11 shows blocked areas typically encountered. Apex blocking is handled by integration over the appropriate region in the numerator of Eq. (3). The unobstructed fractional area in the presence of wedge blocking is taken as

$$K = 1 - \frac{\beta_1 + \dots + \beta_n}{2\pi} \quad (5)$$

Axially symmetric rings and fractional rings are included by writing $E_f(\psi)$ with appropriately placed regions of partial or total blocking by writing

$$K_1(\psi) = 1 - \frac{\alpha_1(\psi) + \dots + \alpha_n(\psi)}{2\pi} \quad (6)$$

The denominator of Eq. (3) is unaffected by the obstructions and Eq. (3) can be written to include the blocking as

$$\eta_B = \frac{2 \cot^2 \left(\frac{\Psi}{2} \right) \left| \left(1 - \frac{\beta_1 + \dots + \beta_n}{2\pi} \right) \int_{\Psi_1}^{\Psi} K_1(\psi) E_f(\psi) \tan \left(\frac{\psi}{2} \right) d\psi \right|^2}{\int_0^{\Psi} [E_f(\psi)]^2 \sin \psi d\psi + \int_{\Psi}^{\pi/2} [E_f(\psi)]^2 \sin \psi d\psi + \int_{\pi/2}^{\pi} [E_f(\psi)]^2 \sin \psi d\psi + \int_0^{\Psi} [E_{xf}(\psi)]^2 \sin \psi d\psi + \int_{\Psi}^{\pi/2} [E_{xf}(\psi)]^2 \sin \psi d\psi + \int_{\pi/2}^{\pi} [E_{xf}(\psi)]^2 \sin \psi d\psi} \quad (7)$$

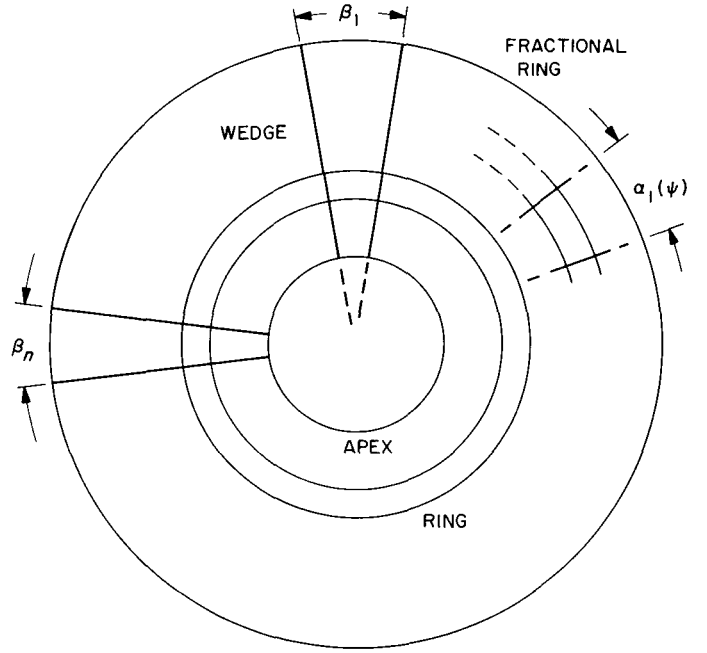


Fig. 11. Blocked areas, efficiency computation

where Ψ_1 represents the apex blocking extremity. As mentioned above, a computer program has been written to numerically evaluate Eq. (7). Because system optimization includes a trade-off between gain and noise temperature, as a function of spillover, this program continuously evaluates Eq. (7) with Ψ as an independent variable, thus computing $\eta_B(\Psi)$ for $0 < \Psi < \pi/2$. Six energy distributions representing the denominator of Eq. (7) are output:

- (A) $0 < \psi < \Psi$, dominant and cross-polarized, referred to total energy.
- (B) $\Psi < \psi < \pi/2$, dominant and cross-polarized, referred to total energy.
- (C) $\pi/2 < \psi < \pi$, dominant and cross-polarized, referred to total energy.

It will be noted that distributions (B) represent the rear, or ground, spillover for the zenith look orientation of the antenna.

To operate the program the following parameters are input:

- (1) $E_f(\psi)$ or $20 \log_{10} E_f(\psi)$ defined for $0 < \psi < \pi$.
- (2) $E_{xf}(\psi)$ or $20 \log_{10} E_{xf}(\psi)$ defined for $0 < \psi < \pi$.
- (3) $K_1(\psi)$ or $K_1(\psi) = \text{CONSK}$, if no ring blocking exists.
- (4) Ψ_1 , apex blocking extremity, deg.
- (5) K , if wedge blocking exists.
- (6) PSIONE, starting value of continuous integration, deg.
- (7) DELPNT, print increment for ψ during continuous integration, deg.
- (8) Interpolation, linear, in either field-strength or \log_{10} power independent of the input form.
- (9) Additionally, several machine control parameters are input affording operational convenience.

Aperture efficiency, as defined, is referred to that obtained with uniform illumination, accounting for space loss, that is,

$$E_f(\psi) = \sec^2\left(\frac{\psi}{2}\right), \quad 0 < \psi < \Psi$$

$$E_f(\psi) = 0, \quad \Psi < \psi < \pi$$

A test case using the above dominant polarized input, no cross-polarized component, and no blocking gave results accurate to $+0.2$, -0.1% for $0 < \psi < \pi/2$, interpolating between 1-deg data points. Thus, the program is considered sufficiently accurate to be a valuable tool for optimizing the ratio of aperture efficiency to system noise temperature, as well as yielding highly accurate absolute efficiency values in the absence of phase errors.

Preliminary results, based upon averaging the Cassegrain feed patterns used on the 30-ft az-el at 8450 Mc, indicate the following aperture efficiencies in the absence of phase errors and cross-polarization:

Case A. No blocking; η (62 deg) = 0.826.

Case B. Subreflector blocking; η_β (62 deg) = 0.760.

Case C. Subreflector and quadripod blocking; η_β (62 deg) = 0.647.

The advantage of continuous evaluation of $\eta_\beta(\Psi)$ and the energy distributions is evident in Fig. 12 which represents Case C, above. In Fig. 12, peak efficiency is seen to occur with an edge angle of 59.0 deg, accompanied with spillover of nearly 3%. The 30-ft antenna has an

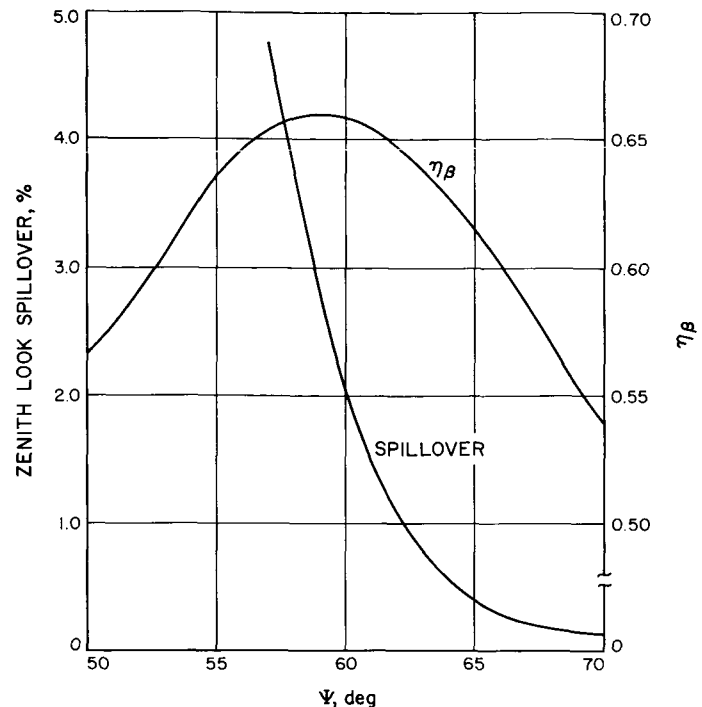


Fig. 12. Efficiency and spillover: 30-ft az-el feed system, 8450 Mc

edge angle of 62.0 deg, yielding somewhat less efficiency; but zenith look spillover is 1.09%. Case C computed results also show a forward spillover of 2.42%.

Future studies will include cross-polarization, and the radiation pattern program will be utilized to obtain a representative figure for gain loss due to feed phase and surface deformation losses. Availability of the above two efficiencies will allow an accurate prediction of over-all antenna efficiency.

B. Planetary Radar Project

1. Radar Observations of Mars

a. Introduction. During the recent opposition of Mars, a series of radar observations was made at the DSIF's Goldstone radar station. These measurements were run during the several weeks from January 31, 1963 to March 2, 1963, with essentially the same radar which was used

(SPS 37-19, Vol. III, pp. 23-27; 37-20, Vol. III, pp. 39-42; 37-21, Vol. III, pp. 47-49) and the system noise temperature has been lowered to 37°K (SPS 37-17, Vol. III, pp. 18-21; 37-20, Vol. III, pp. 38-39; 37-21, Vol. III, pp. 40-41). Two types of experiments were performed. One was the measurement, using radiometer techniques, of the total power contained in the echo. The other was an analysis of this power, using the autocorrelation approach, into its frequency spectrum. The equipment which was used to accomplish this is described in detail in a separate report (SPS 37-14, Vol. I, pp. 111-116 and Ref. 4).

b. Spectrogram. Fig. 13 is a sample spectrogram averaged over several weeks of data. It represents over 65 hr of signal integration, covering echos from a full 360 deg of Martian longitude. A pure sine wave is transmitted but, due to the doppler effect resulting from the planet's rotation, the echo spans a frequency interval of 7.6 kc. As can be seen from Fig. 13, most of the power is contained in a band of only 450 cps. This corresponds to reflections from a disk about 250 mi wide on the surface of Mars. Thus, the sub-Earth point stands out as a small highlight area. Venus shows a similar but larger highlight in proportion to its size so that Mars is somewhat smoother than Venus, in this sense.

c. Total power measurements. Each transmit cycle lasted about 11 min, which was the radar round-trip time to Mars. This was followed by a receive cycle of the same length. In this manner each successive transmit cycle illuminated an area about 200 mi farther westward at about 13 deg North latitude on Mars. Throughout the

nights of the experiment, each 250-mi disk was illuminated about 12 times. The average signal power from each of these areas defines a radar brightness map for the 13-deg parallel on our neighbor planet.

Fig. 14 shows this radar map. Since echo power was measured through a 400-cps predetection filter, dark areas may be due either to lower reflectivity or to rougher areas which spread the signal beyond the filter passband. A map of some of the visible features on the Martian surface serves as a background. It is interesting that the region of Syrtis Major appears light to radar but dark to visual observations. Error flags on the curve were determined experimentally by measuring the standard deviation of the observations with only noise applied to the receiver. A reflectance of 3.2% is obtained by averaging all of this data together.

Mars is a very difficult radar target because of its great distance from the Earth, rapid rotation rate, and poor reflectivity. During future oppositions, when the state of the radar art is advanced and Mars comes much closer to us than the 62,400,000 mi this year, it will be possible to obtain data for much more detailed maps.

2. Mod III Transmitting System

As reported in SPS 37-22, Vol. III, p. 17, the period since the termination of the radar exploration of Mars, Mercury, and Venus experiment has been used to correct a number of transmitter deficiencies that have been contributing to reduced reliability. The major effort has been

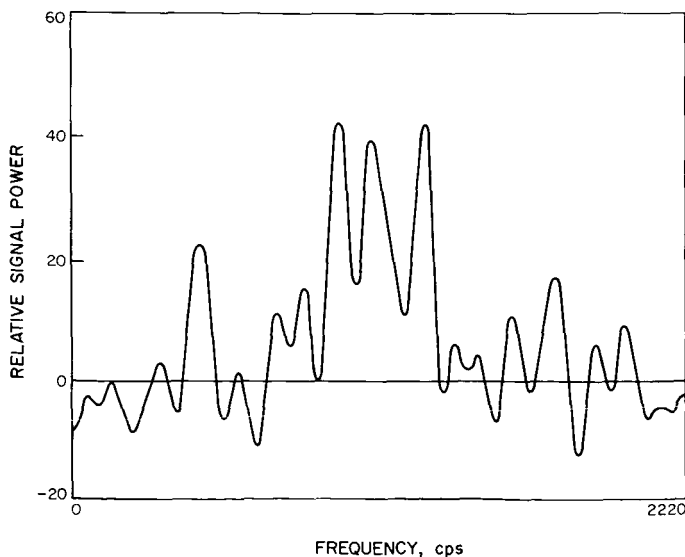


Fig. 13. Echo spectrogram

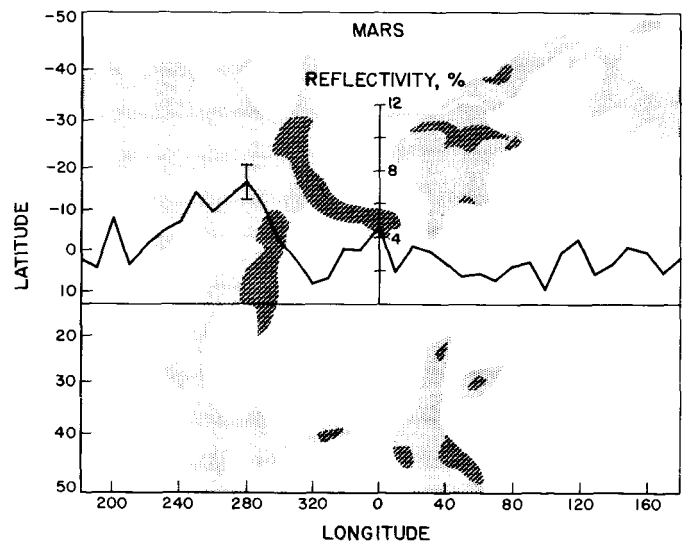


Fig. 14. Radar reflectivity of Martian thirteenth parallel

devoted to the 100-kw amplifier protective circuit and the power supply rectifier tubes. Concurrent with this program has been the documentation of the system. The contract for the transmitting system was terminated in April prior to completion of the documents by the contractor.

a. 100-kw S-band klystron amplifier. As stated in the referenced SPS, one of the major factors resulting in degraded transmitter reliability was false crowbar actions triggered by noise pulses picked up by the circuit used to measure the klystron body current. Three systems protect the klystron against high body current. A slow-acting circuit, intended primarily for gradual increases in current experienced while tuning the klystron, will shut the system down but will not trigger the crowbar. A second system will respond in milliseconds to high body current and crowbar the dc high-voltage power supply output. In a third system, which protects the tube in the event of

an actual klystron body arc, the surge of power supply current is applied to a pulse transformer in the crowbar cabinet which fires the crowbar within 5 μ sec. In the first and second systems, body current is sensed by a Hewlett-Packard 828B dc current meter and 3528A probe used as a differential ammeter. Both the anode and cathode power cables run through the same current probe with the cables arranged so that the currents in the two cables run in opposite directions. The ammeter then measures the difference between the currents in the two wires. This difference is the current which returns to ground through the klystron body rather than by the normal path to the anode. The current meter provides a voltage output which is proportional to the measured current. This voltage is sensed by the body current meters and by the crowbar logic chassis. Relay type body current meters constitute the slow-acting protective circuit; the crowbar logic chassis constitutes the fast response circuit which shuts off the high voltage when rapid transients occur (Fig. 15).

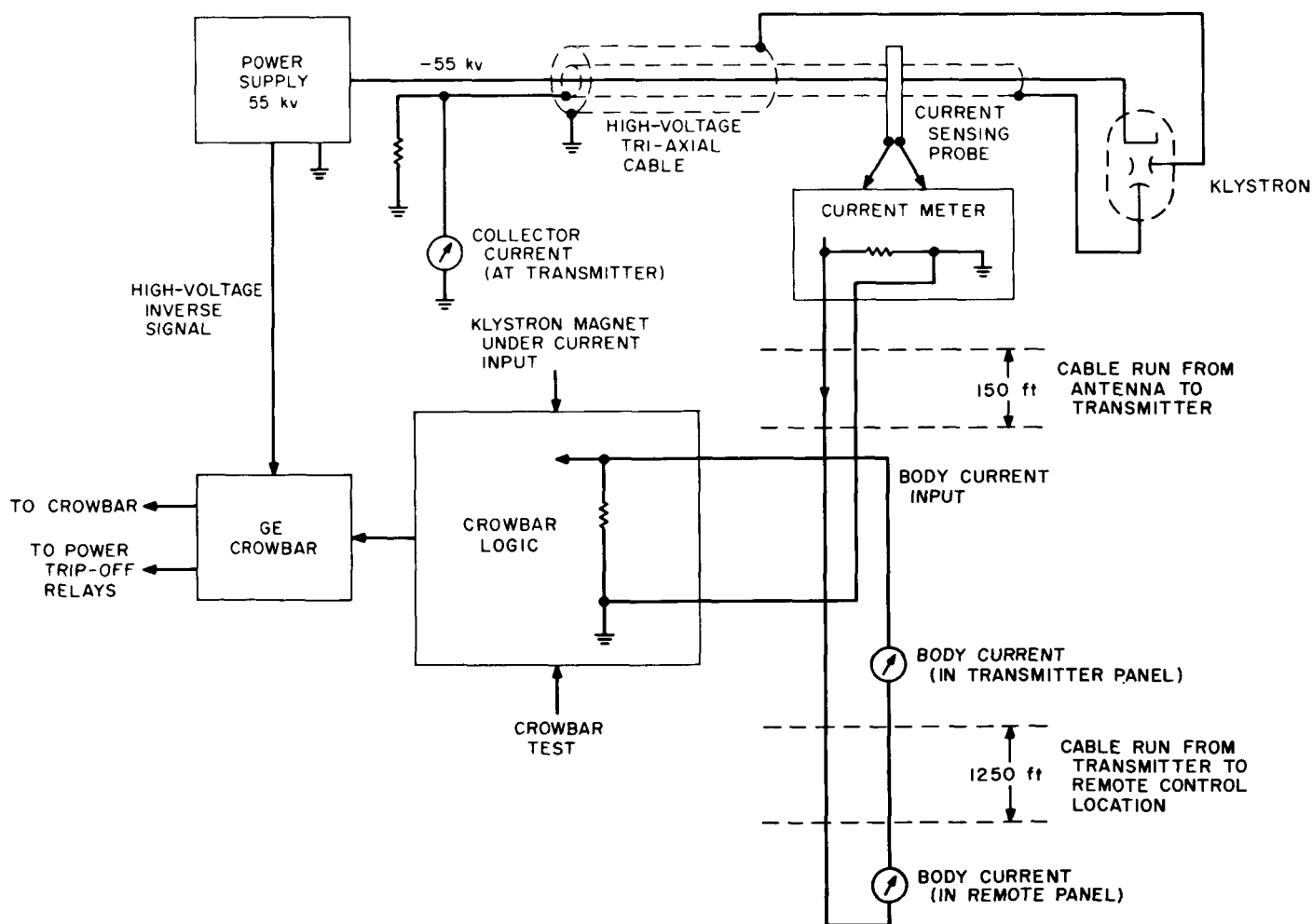


Fig. 15. Original crowbar circuit

The circuit of the dc current probe and the crowbar logic was analyzed, and the response time was calculated at over 1000 μsec . The main limitation is in the Hewlett-Packard current probe sensing unit.

Prior to analyzing the actual transient response of the crowbar circuits, the steady-state trip level of the crowbar had to be set. A nominal klystron body current was

assumed as the operating value. A second body current value was chosen to provide a margin of approximately 100% above the operating body current. This value of dc current was then sent through a temporary wire passing through the current probe (Fig. 16). The "body current" trip-adjust control was subsequently adjusted until a crowbar was obtained.

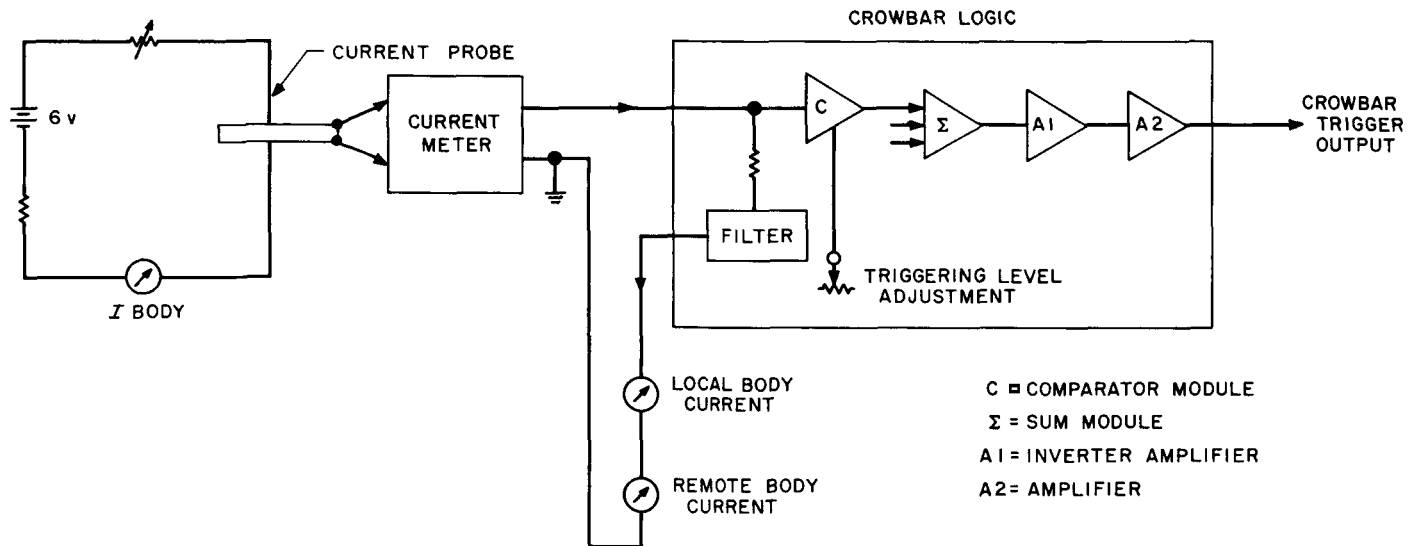


Fig. 16. DC calibration of crowbar circuit

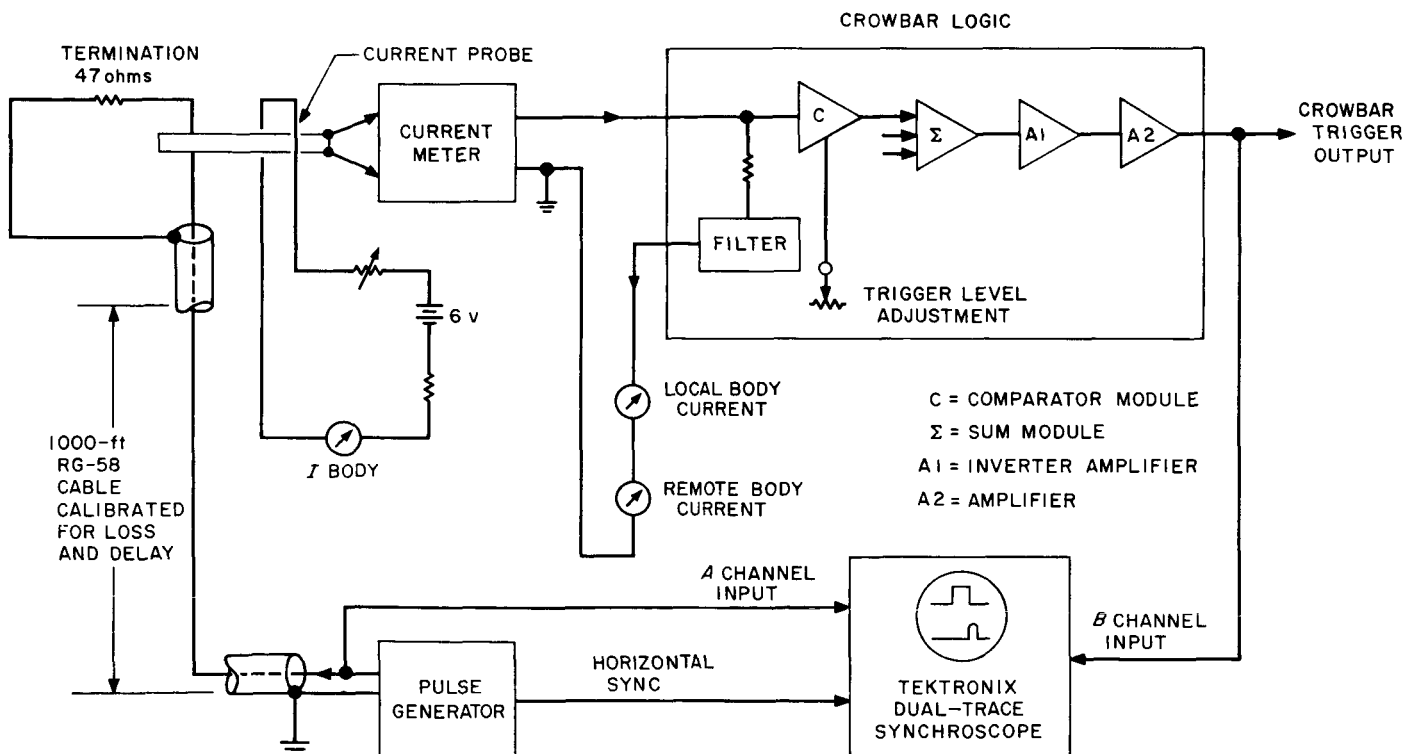


Fig. 17. Calibration of crowbar response

It was desirable to analyze the transient response of the crowbar circuit under normal operating conditions. This was provided by maintaining the crowbar logic trip level setting mentioned above and simulating the operating klystron body current with a battery and an auxiliary current loop threading the current probe (Fig. 17). A single pulse of current was fed through a wire looping through the current probe, and the corresponding crowbar logic output pulse was observed. The delay was $2,950 \mu\text{sec}$.

The following steps were taken to make the crowbar more reliable and less susceptible to false signals:

The output of the crowbar logic chassis is a relatively high impedance. This is undesirable since the crowbar logic chassis must drive a low impedance silicon-controlled rectifier, and the long cable from the crowbar logic chassis to the high-voltage power supply is susceptible to pickup. The problem was corrected by installing

an emitter follower in the crowbar logic chassis, thereby providing the low output impedance.

The crowbar logic high-frequency response was reduced to a value approaching the actual requirements of the input signal from the body current probe.

A 60-cps filter and a 400-cps filter were placed at the input to the crowbar to reduce power line pickup.

The Hewlett-Packard current probe output was sent directly to the crowbar logic chassis instead of passing through 2500 ft of wire and two body current meters as was originally the case (Fig. 18).

Shielded, twisted-pair wire was installed for the crowbar logic signal wires. In addition, the offending transmitter control panel switches were noise-suppressed.

The final effort involved placing the crowbar logic chassis in a completely shielded box containing power

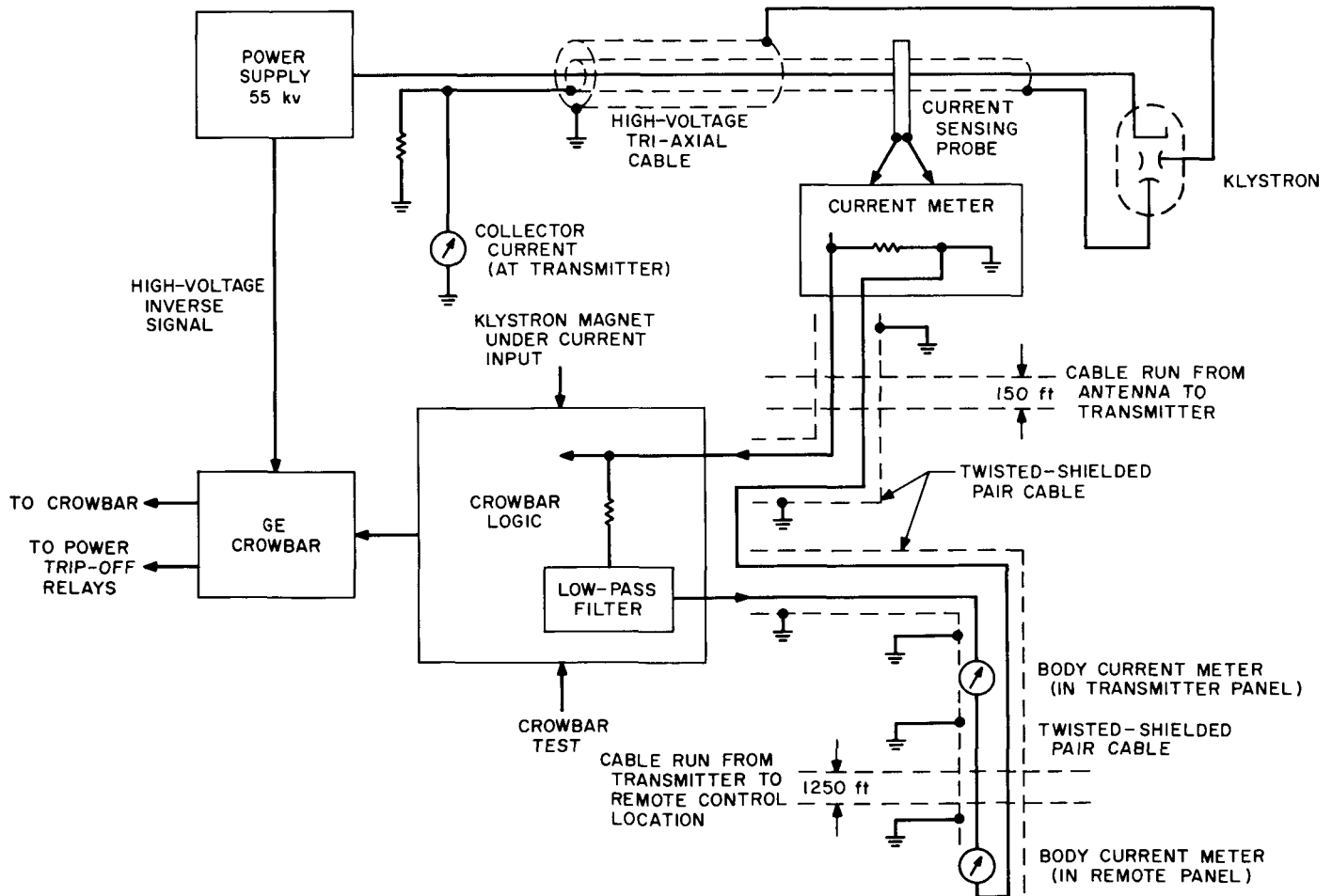


Fig. 18. Modified crowbar circuit

line noise filters and coaxial cable connectors for input and output signals (Figs. 19 and 20).

A further improvement was made to the crowbar indication circuitry. The relay on the crowbar logic would not respond to fast transients and indicate a body current crowbar. This was true even though an actual crowbar was produced. It is of vital importance to differentiate between klystron crowbars and high-voltage power supply crowbars in order to locate and correct faulty components. A transistorized multivibrator and keyed amplifier circuit was designed and installed in the crowbar logic chassis. The indicator circuit now responds to all klystron crowbars and furnishes an indication distinct from power supply crowbars.

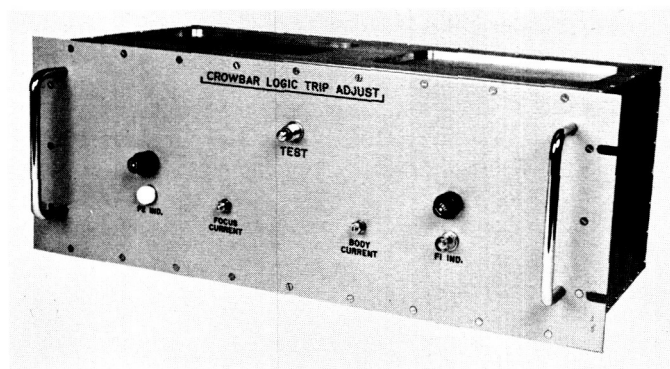


Fig. 19. Photograph of crowbar logic

b. Beam power supply. In SPS 37-22 it was stated that a set of rectifier tubes had been procured from a second source. These rectifiers were aged and tested during this reporting period. There were no internal or external arcs in connection with these rectifier tubes during the time they were in operation. The dc power output was held between 514 and 590 kw for 3 hr and 30 min without any rectifier difficulty. Since only six rectifiers were used in this test, each tube was carrying a load in excess of that required with 12 tubes in the circuit and 1,000-kw dc output.

A set of six tubes from the original source was also aged and tested during this period. Although this supplier has an improvement program underway for his rectifiers, this set tested was practically the same as those originally supplied. During the test program, there were a number of internal arcs as the "out-gassing" of the tubes occurred. This set of six tubes was operated at above 500 kw for 4 hr, but they were not free of internal arcs as were those from the second source.

c. RF switch isolation. It was reported in SPS 37-22 that a test was made to determine the noise power developed by the klystron beam without drive. In order to obtain additional information which will be needed in future planetary experiments, a test was made to determine the isolation provided by an RF switch. The test setup was as shown in Fig. 21, and the results are plotted in Fig. 22. From the curve in Fig. 22 it can be seen that

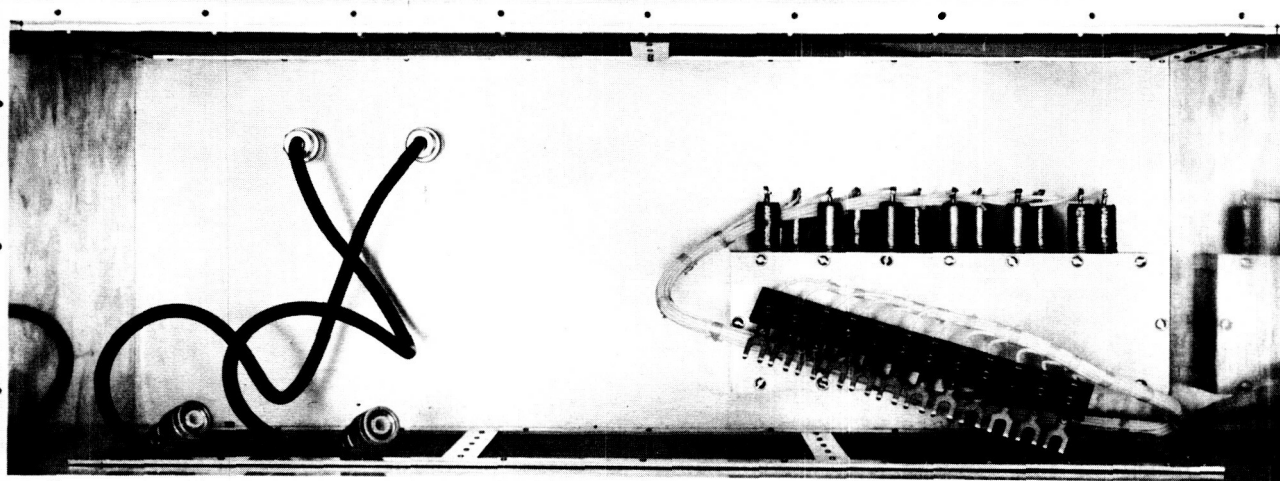


Fig. 20. Photograph of crowbar logic case

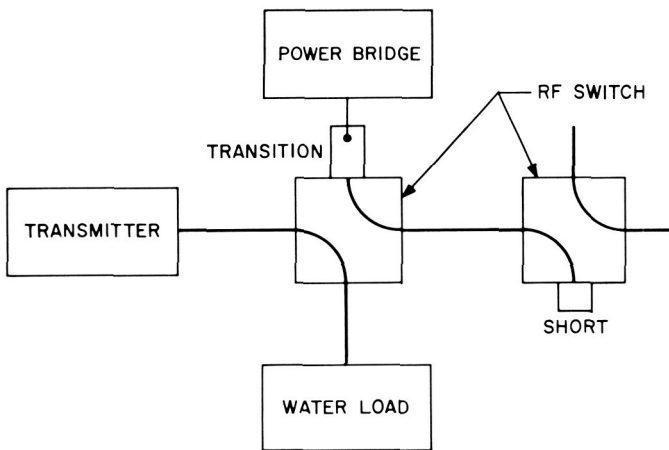


Fig. 21. Switch isolation test

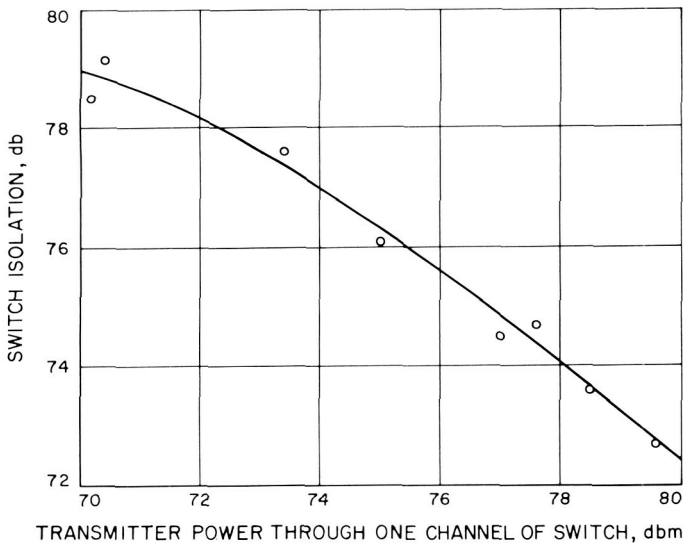


Fig. 22. RF switch isolation

the switch attenuation is tending toward approximately 80 db as the transmitter power was reduced. This correlates with the data taken on the switch in the laboratory using a low-power signal generator. The exact reason for a decrease in switch attenuation with an increase in transmitter power is not known at this time. The most logical explanation is that the switch heats under power. This results in changes in the mechanical fit of the stator and rotor, which causes reduced attenuation.

3. Mod IV Planetary Radar Exciter

A new exciter, of improved design, for use with the 100-kw S-band transmitter has been fabricated and in-

stalled at the Goldstone Venus site. Data has been taken to verify performance to the design specifications.

a. Purpose. The Mod III exciter, described in SPS 37-19, Vol. III, pp. 23-27, was originally designed for use with the 10-kw transmitter and through numerous modifications served through the first planetary work using the 100-kw transmitter. With the move of the planetary radar to the control room and a general upgrading of the system, it became desirable to replace the exciter to provide compatibility with other parts of the system, improve reliability and stability, and bring performance in line with current state-of-the-art. Most modules in the Mod III were several years old and did not conform to present designs.

b. Description. The new exciter design is based on operating experience from the Mod III and so did not differ greatly from the last block diagram of that unit. The principal improvements are:

- (1) All modules are the new low-leakage type providing leakage around the package or on any power lead less than $3 \mu\text{V}$. This has proved of prime importance in operating large systems. The Mod III module leakages were in excess of $10 \mu\text{V}$.

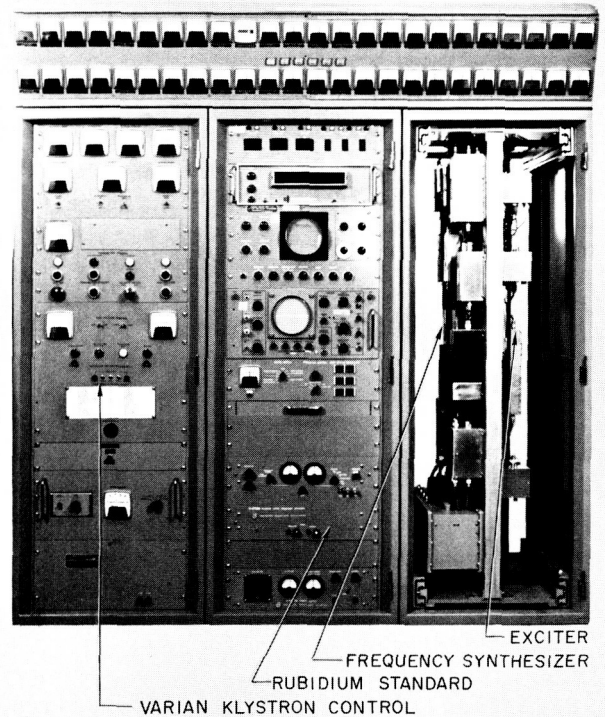


Fig. 23. Mod IV planetary radar exciter

- (2) The modules are mounted on a standard cold plate to provide temperature stabilization through water cooling.
- (3) More reliable power supplies are used.
- (4) Improved metering, protective, and data readout circuits are provided.

Fig. 23 is a photograph of the exciter together with the rubidium frequency standard, the frequency synthesizer, and the 100-kw transmitter remote controls. These systems are mounted together for operating convenience. Fig. 24 is a block diagram of the exciter. Blocked grid keying at 31.84 Mc and phase modulation at 159.2 Mc are provided as they are used in the planetary radar. In addition to the blocked grid keying, a coax relay is provided at the input to assure sufficient attenuation of the drive signal during receive periods. The signal is conducted to the antenna at 159.2 Mc, where it is multiplied to 2388 Mc and amplified to 3 w to drive the klystron. The drive requirement of the 100-kw klystron

in the present mode of operation is 100 mw so no limitations will be placed on power output by the exciter.

Bandwidth characteristics are shown in Fig. 25. The 3-db bandwidth of 6 Mc is twice the minimum requirement in this system. This measurement was made by

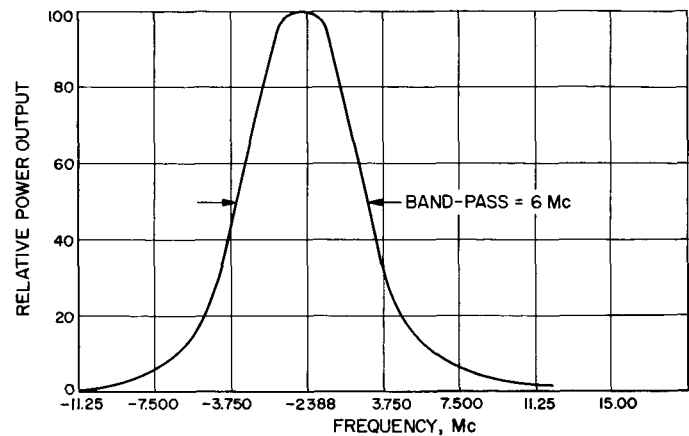


Fig. 25. Frequency exciter

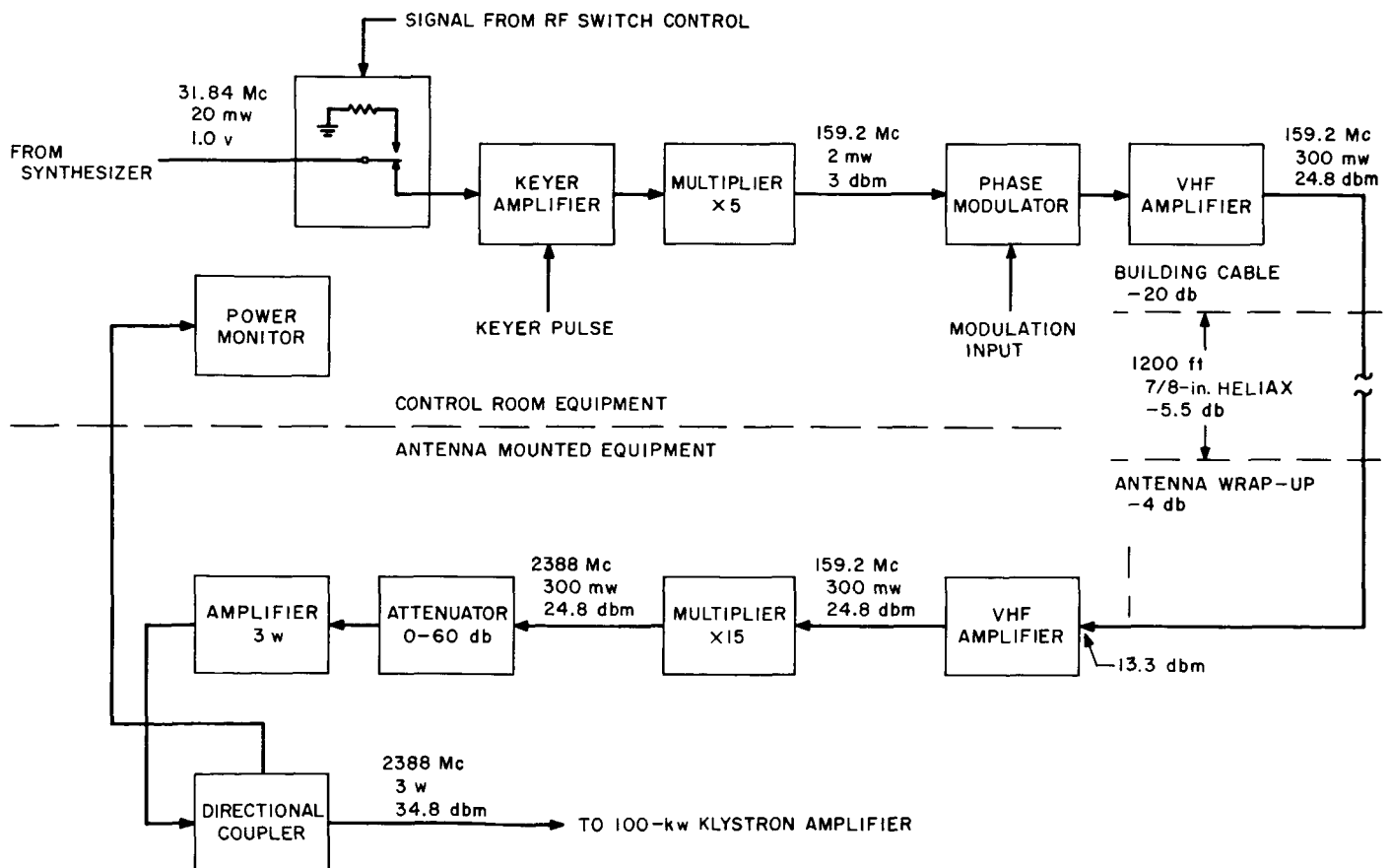


Fig. 24. Mod IV S-band exciter

injecting a signal into the $\times 5$ multiplier and measuring the power output of the 3-w amplifier.

The rms phase deviation at 2388 Mc in a 5-cycle loop was 2.7 deg. This measurement was made by feeding a strong signal into the front end mixer of the Mod IV planetary radar receiver and comparing this signal to the main VCO of the receiver. The phase deviation measured was, therefore, the rms sum of the phase deviation of the exciter and the receiver. This is well within allowable limits.

4. Mod IV Planetary Radar Receiver

a. Introduction. Further steps have been taken on the installation at the Venus site, Goldstone Tracking Station, of the Mod IV planetary radar receiver described in previous summaries (SPS 37-21 and 37-22, Vol. III). Specifi-

cally the "front end" and associated power supply were installed in the antenna feed cone, the performance of the synchronous receiver AGC system was measured for the entire receiver, and the AM spectrum analysis equipment was used to check for spurious signals in the non-synchronous receiving channels. Subsequently, the cone was removed from the antenna and placed in the cone storage area of the transmitter building to permit resurfacing of the antenna (Fig. 26). Temporary cables have been installed to allow further operation and testing of the receiver.

b. Synchronous receiver AGC system. Performance of the AGC system was determined by measurements of the static gain error and the AGC loop frequency response. The static gain error is a measure of the AGC system capability of holding the receiver output to a small change (ideally 3 db or less) over a large input signal range (desirably 100 db). To accomplish this a tracking receiver usually employs AGC on both IF amplifiers. In the present receiver configuration the 30-Mc IF preamplifier is shared by five receiving channels; hence, its gain cannot be controlled automatically by any one channel. Therefore, only the 30-Mc balanced mixer and 455-kc IF amplifier of each channel are gain controlled. The total gain of the two modules is about 100 db, which does not permit the AGC system to handle a 100-db dynamic range of signal. Fig. 27, the receiver static gain characteristics, shows that the output level is held within 3 db for an input signal change of -160 to -87 dbm. This is adequate for planetary ranging.

The frequency response of the AGC loop must be measured on a piece-wise basis since the loop gain varies

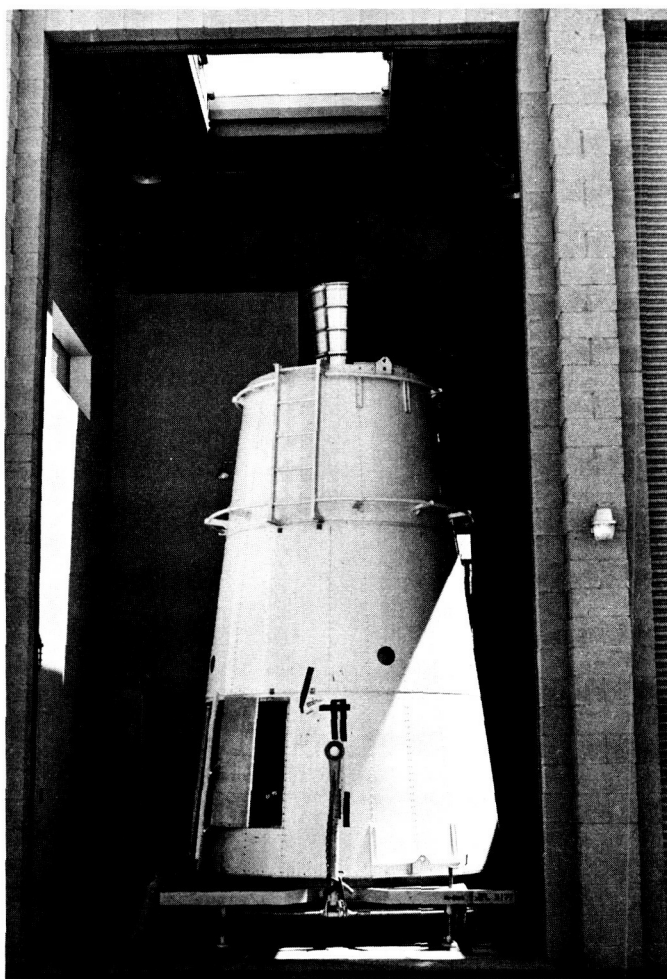


Fig. 26. Planetary radar cone in cone storage area after removal from az-el antenna

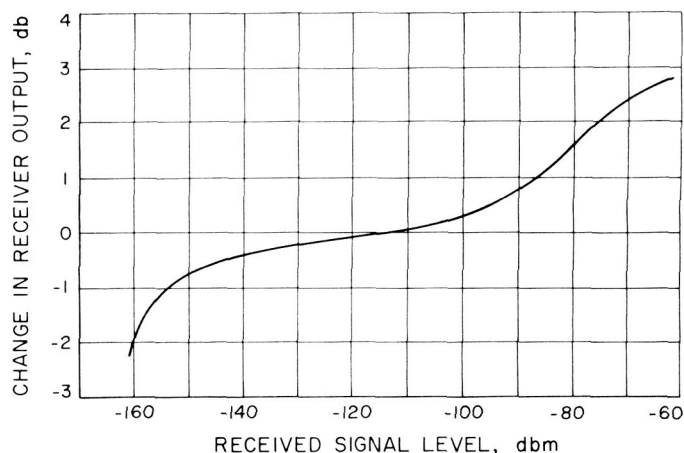


Fig. 27. Static gain control characteristics of Mod IV receiver with no AGC on 30-Mc preamplifier

with signal level but is essentially constant for small-signal changes (on the order of 3 db). The transfer function of the AGC loop is:

$$H(s) = \frac{1}{\left(\frac{1}{G} + 1\right) + \frac{\tau}{G}s} \quad (\text{Ref. 5})$$

where

G = AGC loop gain

$$= K_A K_D A$$

K_A = receiver attenuation constant

K_D = AGC detector constant

A = AGC dc amplifier gain

τ = AGC filter time constant

From this, the amplitude response can be obtained:

$$|H(\omega)| = \frac{G}{\tau} \left[\frac{1}{\left(\frac{1+G}{\tau}\right)^2 + \omega^2} \right]^{1/2}$$

The frequency response was measured by amplitude modulating the receiver input signal and recording the resultant ac component on the AGC voltage. Figs. 28 and 29 are the theoretical and measured results for signal levels of -125 and -150 dbm. Curves run at -95 and -135 dbm are similar. Only data for the $\tau = 290$ -sec filter is shown for -150 dbm; the $\tau = 10.8$ -sec filter is not normally used for weak signals.

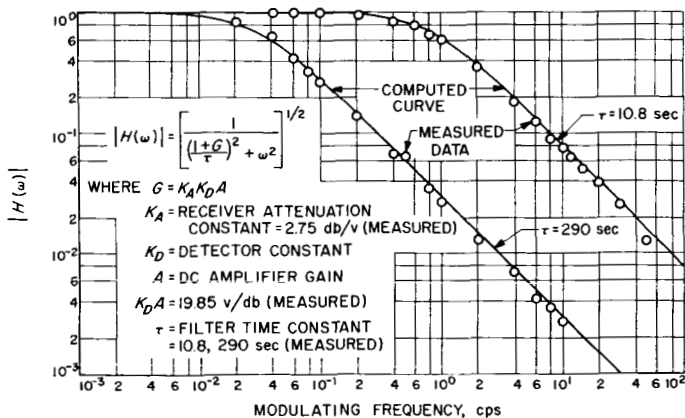


Fig. 28. AGC loop frequency response, -125-dbm signal level

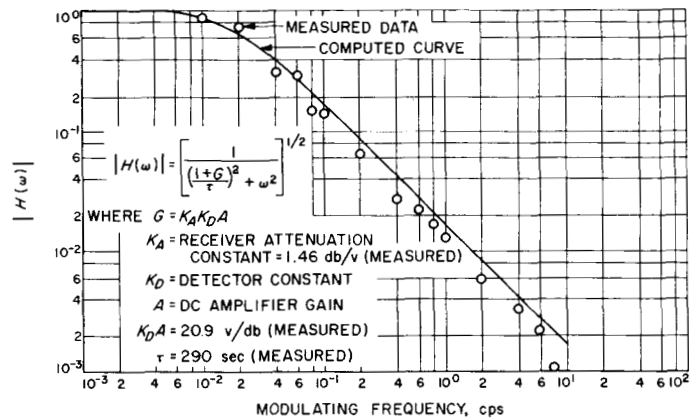


Fig. 29. AGC loop frequency response, -150-dbm signal level

c. Spurious response. The AM spectrum analysis equipment was used to detect leakage and spurious signals in the nonsynchronous receiving channels. This unit is a device for determining the power spectrum by statistical methods. Leakage at 30 Mc, equivalent to -177 dbm at the receiver input, was detected on the AGC bus of the AM channel. The leakage, introduced by a vacuum tube voltmeter monitor lead, was eliminated by filtering.

5. Phase Coherent 30-Mc Monitor

a. Introduction. The planetary ranging system measures the propagation time of the signal from the antenna to the planet and back plus the propagation time through the transmitter and receiver. The delay in the transmitter and receiver represents an error of approximately 2500 mi which must be removed by measuring the delay and subtracting it from the total measured time. In the past the delay has been measured prior to a data run. Because the delay varies due to drifts in the system, it was considered desirable to measure it during each transmitter-on time and subtract that value during the following receiver-on time. This is accomplished by monitoring the transmitter output at the face of the dish (zero range) and feeding it directly into the receiver. For practical reasons the maser and first mixer which uses the programmed local oscillator (LO) are replaced by another mixer and an LO coherent with the transmitted signal so that the calibration signal enters the ranging receiver at the 30-Mc IF. This causes a negligible error because the two front ends are similar and because, since they are broadband, either one contributes a very small portion of the total delay. The equipment to monitor the transmitted signal has been designed, constructed, tested, and is being installed. It also provides a signal to monitor the transmitted spectrum.

b. Description. This equipment provides a 30-Mc signal, which is phase coherent with the transmitted frequency, for the purpose of determining the total delay in the transmit-receive system and also for examining transmitter spurious or sidebands. The block diagram

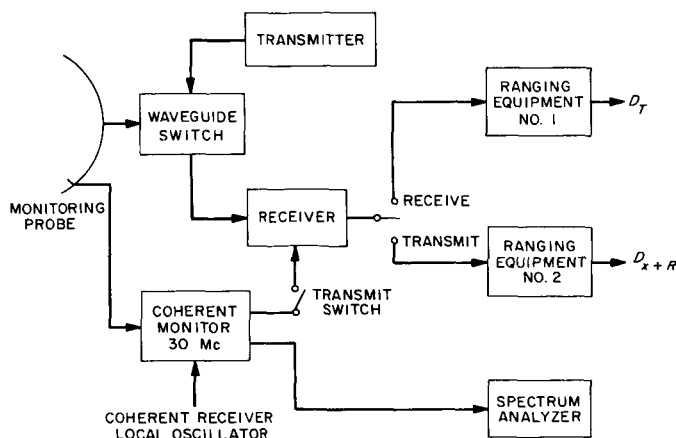


Fig. 30. System for measurement of transmitter, spurious and range zero

shown in Fig. 30 indicates how it ties in with the rest of the system. During the transmit cycle the transmitted output at the face of the dish is monitored by means of a probe and fed to the equipment for conversion to 30 Mc. This signal is fed to the input of a spectrum analyzer for the measurement of transmitter spurious signals and also to the IF section of the receiver. Ranging equipment No. 2 converts the total system delay to the equivalent zero ranging error to provide a zero calibrating signal for the main ranging equipment No. 1 during the subsequent receive cycle. Thus, true range, R_T , is $R_T = (D_T - D_{x+R})/2$ (where D_T = measured distance and D_{x+R} = zero ranging error), which may be read directly from ranging equipment No. 1.

A block diagram of the equipment is shown in Fig. 31. The 31.44-Mc signal, synthesized from the rubidium frequency standard, is fed to the main equipment located in antenna case No. 1 via an amplitude limiting amplifier in order to make up for the loss in the 1500 ft of cable run. The main equipment is housed in a metal box (Fig. 32) which is designed to afford adequate screening from antenna radiation. 700-Mc cutoff low-pass filters are included

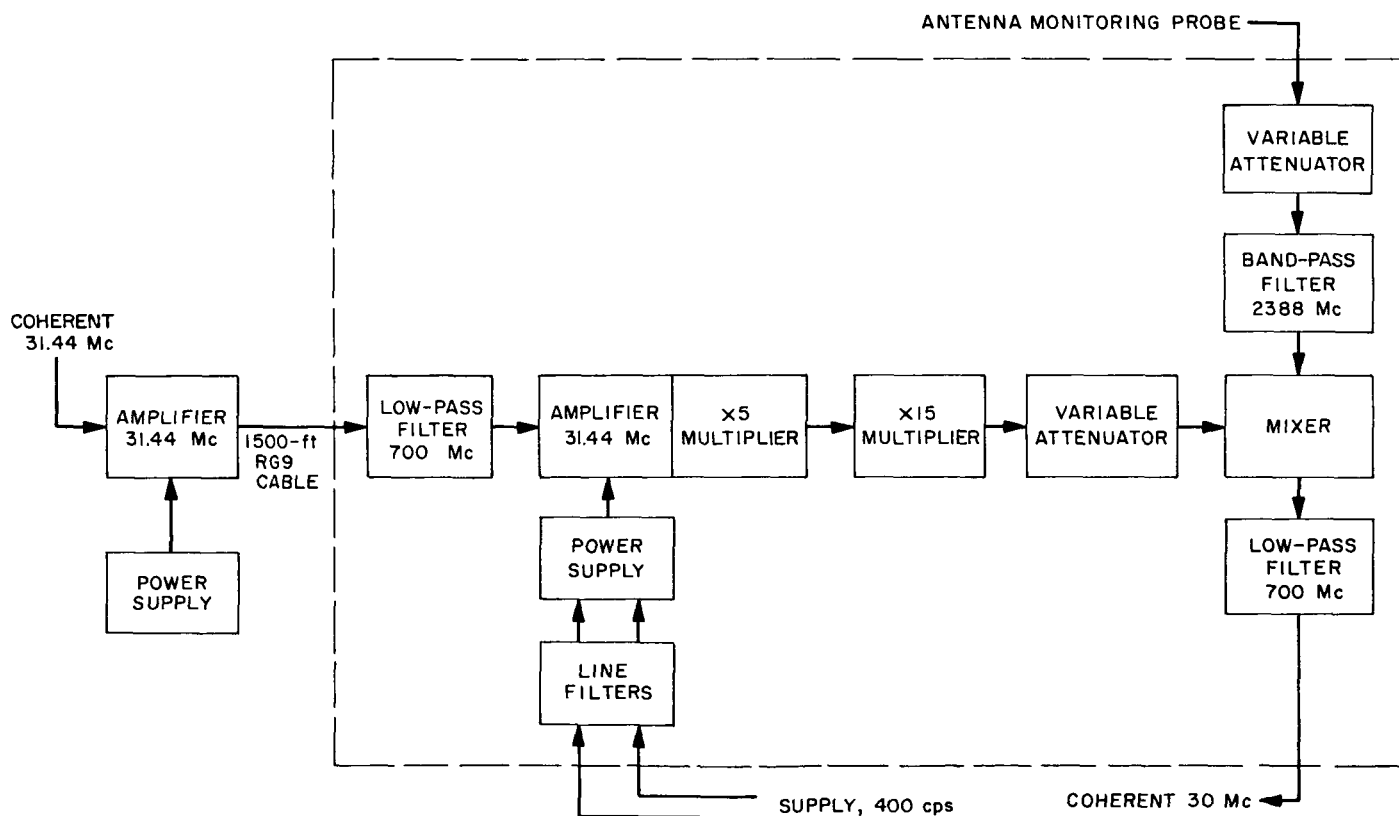


Fig. 31. Block diagram of coherent 30-Mc monitor

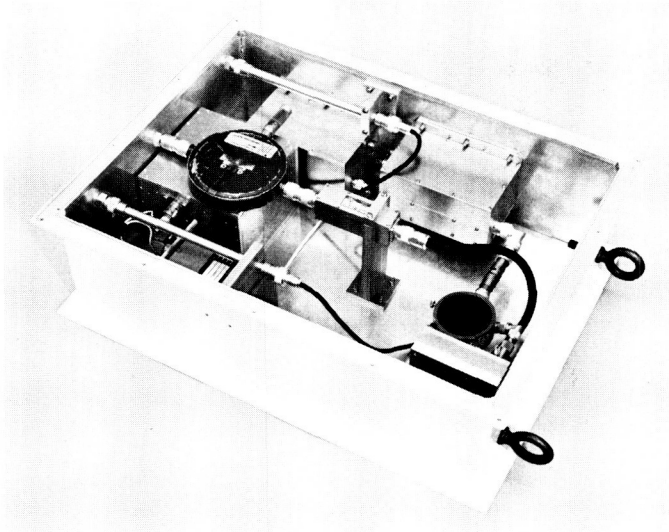


Fig. 32. Photograph of metal box

in the 31.44-Mc input and 30-Mc output lines and line filters in each of the 400-cps 115-v power lines. Referring again to Fig. 31, the 31.44-Mc input signal is further amplitude limited and amplified and frequency multiplied in three varactor stages to the receiver LO frequency of 2358 Mc. In order to minimize the generation of spurious frequency products, bandpass filters are used for matching at the output of the first $\times 5$ multiplier, and at the input and output of the second $\times 3$ multiplier stages. The

2358-Mc LO frequency so obtained is then mixed with the monitored transmitter output frequency to produce the 30-Mc phase coherent signal. Variable attenuators are provided for adjustment of the input levels to the balanced mixer, and the input from the antenna probe is filtered by means of a 2388-Mc bandpass filter.

6. Water Rotary Joint for Az-El Antenna

a. Summary. A high-capacity rotary joint is being developed to carry cooling water for the 100-kw transmitter across the azimuth axis of the 85-ft az-el antenna. In SPS 37-22, Vol. III, p. 29, the fabrication and assembly phase was discussed. This report covers the phase of testing and installation on the antenna.

b. Recent work. Considerable effort was applied in the detail design to incorporate appropriate assembly aids; equally important is the method of assembly itself. Fig. 33 depicts the component assembly. Great care was taken to prevent damage to either the stellite rotating face or the carbon-graphite stationary face. Also, all O-rings were lubricated prior to assembly to prevent rolling or creeping. With regard to the carbon face O-ring, this proved to be inadequate to prevent creeping as will be discussed later. The initial assembly and static proof testing was done by the vendor; it was proof tested at 200 psi with no visible leakage. The assembly was then shipped to JPL for dynamic testing.

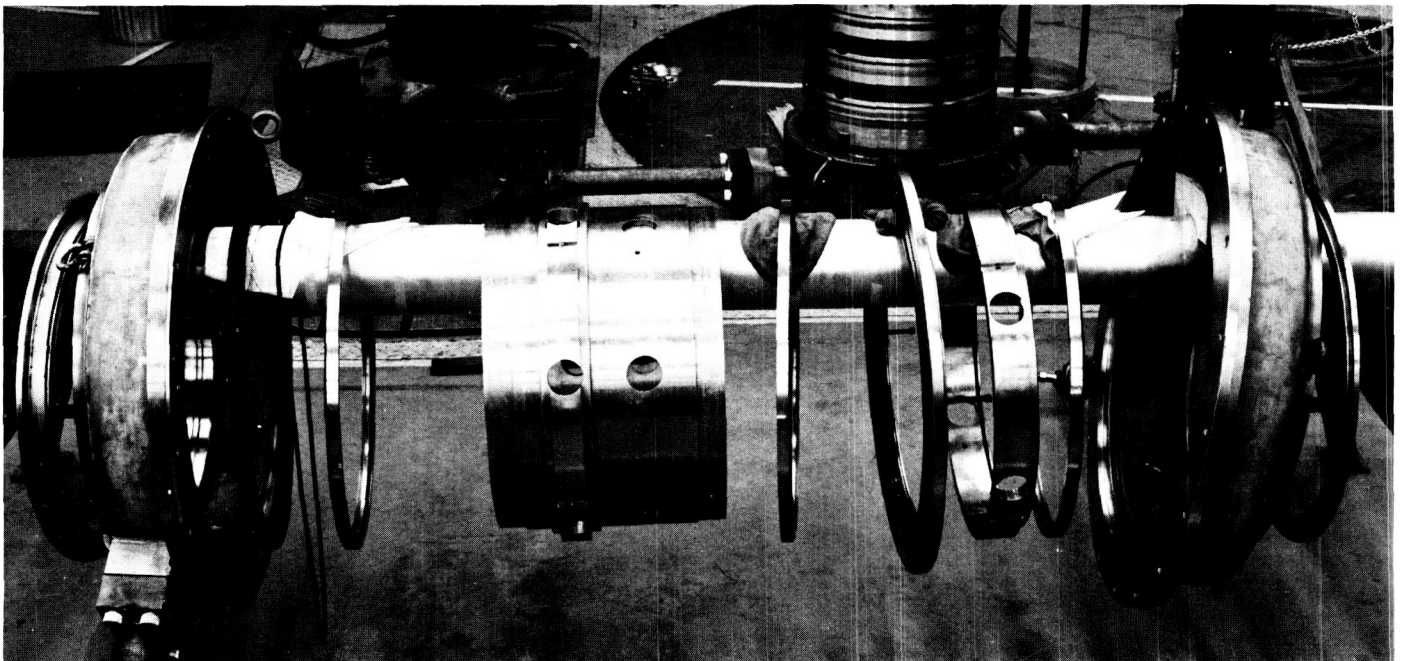


Fig. 33. Component assembly

Fig. 34 shows the dynamic test arrangement that was used. The maximum velocity of the 85-ft az-el antenna at the Venus site at Goldstone is approximately 1 rpm. In order to provide reasonable accelerated life testing, it was decided to conduct all of the dynamic testing at 1 rpm.

An accelerated life equivalent to 20 yr of operation was considered adequate from a quality assurance standpoint and acceptable in wear on the unit since the carbon-stellite combination is considered capable of more than 100 yr of life at the duty cycle of one revolution per day. (For the last 2 yr of operation of the 85-ft az-el antenna, the average total rotation per day of the azimuth axis has been approximately 360 deg.)

As a part of the dynamic testing, restraining torque measurements were made by means of a force dynamometer and the torque arm shown in Fig. 34. Torque measurements were significant in two ways:

- (1) If the seals are operating properly (i.e., self-energizing), there should be a parabolic increase in restraining torque with increase in pressure.
- (2) A maximum value was needed for the design of the floating rotational torque restraint for the actual antenna installation.

Fig. 35 is a plot of the torque-pressure relationship obtained during the tests and shows that the design is indeed self-energizing. The coefficient of friction for the carbon-stellite combination obtained from the experimental torque data is approximately 0.25. This coefficient of friction was somewhat higher than originally anticipated but,



Fig. 34. Dynamic testing

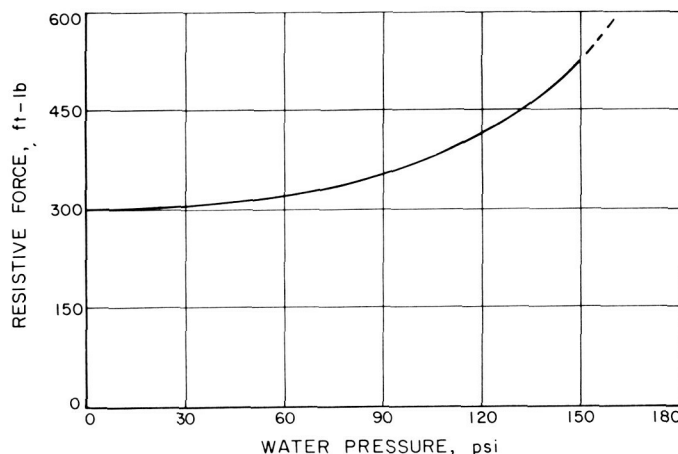


Fig. 35. Dynamic test pressure versus torque

in comparison with other face-seal type material, seems reasonable.

In the initial dynamic test after less than an hour of rotation at a duty cycle of 5 min clockwise and 5 min counter-clockwise at 1 rpm, a steady leak developed. The operating pressure was 150 psi in both cavities.

Upon disassembly an assembly error was discovered in the placement of the top felt seal. Also, proper adhesion between the stainless steel support ring and the felt had not been achieved. This allowed the felt to bunch and force the top carbon gasket from its seat, thus causing the leak. The joint was reassembled with the felt seal properly bonded and assembled. Dynamic testing was resumed with the water temperature at 72°F and system pressure at 150 psi. No leaks developed after 2 hr of cycling. The temperature was then elevated to approximately 115 deg and rotation was continued. After less than 20 min of operation, leaks appeared in both the top and bottom seal.

Disassembly and inspection was again conducted. Both the top and bottom seal appeared displaced from their seats, a condition which would permit fluid flow past the seat gaskets. It was felt that improper assembly techniques had been used, so reassembly was supervised by both JPL and the vendor. After a short period of testing the seals again leaked. At this point the most reasonable explanation was that the O-rings backing the carbon faces were snaking as a result of rotation of the carbon faces. Snaking is a differential creep or bunching of the O-ring which could force the gasket off its seat. A test, using a dry O-ring was conducted to verify this assumption. From the results of this test more adequate restraint of the carbon face was considered necessary. In addition to restraining the carbon, tests were conducted on the

O-ring gasket cross-section change due to static spring loading and hydrostatic loading. Calculations indicated that the carbon face reduced in diameter approximately 0.040 under 150-psi loading. Static loading of the O-ring cross-section indicated that the squeeze was more than adequate to compensate for the change in diameter under hydrostatic loading.

Adequate pinning of the carbon face to prevent rotation was accomplished and the dynamic pressure temperature testing was continued. A life test cycling of both temperature and pressure was conducted.

After rotating for the equivalent of 20 yr of life on the antenna, no visible leakage was observed. On this basis the water rotary joint was considered acceptable for installation and testing on the antenna. Fig. 36 shows the rotary joint installed on the antenna; tests have not yet been conducted on the antenna.

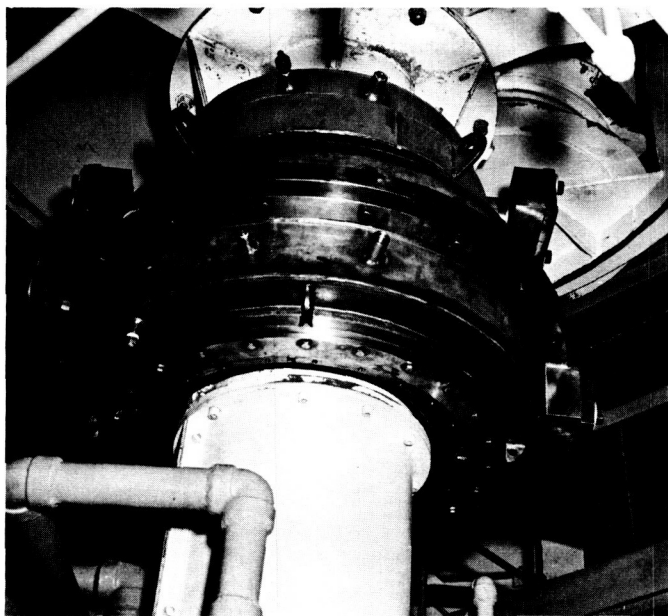


Fig. 36. Rotary joint installed

C. Lunar Radar Project

1. Relationship to Planetary Radar Project

The astronomical radar work at JPL is properly concerned with both lunar and planetary observations in support of the DSIF communications missions with lunar

and planetary spacecraft. Astronomical radar experiments are conducted to provide planned system operations for integrating state-of-the-art components and system concepts and to produce scientific data that will be useful to JPL spacecraft programs. Various circumstances have caused past efforts to be mostly devoted to the planets, but it now seems possible to devote a more appropriate portion of the effort to lunar radar work. In particular, a way has been found to use a tunneled auxiliary antenna to modify the monostatic planetary radar for lunar use.

a. Background. When the first planetary radar was set up at JPL in 1961 for the Venus radar experiment, the Moon was used as a near target to aid in calibrating the system. However, due to the limited time available, it was decided to concentrate on Venus rather than gather extensive data from the Moon. This proved to have been a wise decision, and the improvement in the accuracy with which the Astronomical Unit was known resulting from this experiment was invaluable to the *Mariner 2* flight. In any case, the radar was not really suited to lunar work because, in spite of the physical separation of the transmitter and receiver antenna by 7 mi and two ranges of mountains, the leakage signal tended to interfere with the return signal unless there was a considerable doppler shift. The returns from Venus had a considerable doppler shift except very near conjunction; those from the Moon did not.

When the second planetary radar was set up, a monostatic system, the situation changed with respect to leakage, but was even less favorable for the Moon. Since the transmitter and receiver share the same antenna, the leakage signal is large enough that, for any known form of feed system, the receiver would saturate even though it was not tuned to the transmitted frequency. In other words, even the doppler shifts encountered with the planets do not allow simultaneous operation of the transmitter and receiver. The solution was to time-share the antenna, transmitting for one round-trip signal travel time, then receiving for a round-trip time. In order to time-share the antenna, the transmitter and receiver are alternately connected to the same feed by a waveguide switching system. When the transmitter is off, the drive is turned off but the klystron beam is left on. When the receiver is off, the local oscillator (LO) is turned off and the maser connects to a cold load. The effect of the waveguide switching system is to attenuate the klystron beam noise when the receiver is on enough so that the receiver performance is not degraded, and to attenuate the transmitter power enough when the receiver is off so that the maser is not damaged. The LO being off keeps the re-

ceiver from saturating. This system works well for the planetary case where the round-trip time is several minutes. For the lunar case with round-trip times of less than 3 sec, it is not presently possible to obtain waveguide switches that operate fast enough. Even if high-speed drives could be developed for the present switches, their life would be only a fraction of a day at the high switching rates. Furthermore, electronically controlled isolators, e.g., of the ferrite type, do not have the required isolation. For these reasons, the only lunar observations that were made during the early part of the program in 1962 and 1963 were calibration runs using the output of the exciter with the klystron turned completely off. The drive on the exciter can be keyed electronically, but the maximum power is 3 w and it was usually run at a fraction of a watt. The waveguide switching was, of course, not used.

Recent experiments on the use of an auxiliary tunneled antenna (SPS 37-21, Vol. III, pp. 30-40) mounted at the apex of the 85-ft Venus site antenna indicate that there is a way of modifying the planetary radar system for lunar use. The attenuation between the two antennas approaches 90 db. If one is used for the transmitter and one for the receiver, the attenuation is not sufficient to allow simultaneous operation, but it does provide protection for the maser when the transmitter is on, and probably will provide adequate attenuation of the beam noise when the transmitter is off. An analysis of the expected signal-to-noise ratio is given in the following article for a particular system configuration.

b. Program. A Lunar Radar Project is being set up to develop a system and conduct experiments in a manner similar to that of the Planetary Radar Project. This system will employ essentially the same major equipments as the planetary radar (except for the auxiliary antenna) but will operate in a somewhat different way. Even though the smaller antenna will cause a loss in system performance of some 25 db relative to the planetary radar, the space loss is reduced by more than 80 db so that much stronger signals may be expected from the Moon. This allows for quite different signal detection and processing methods.

The initial work will be concerned with installing the auxiliary antenna and measuring the characteristics of the system. Of particular importance is the determination of the gain of the system and the isolation between the two antennas. As is pointed out in the next article, the signal-to-noise ratio of the received signal is strongly dependent on the available isolation. Another important

factor determining the performance of the system is the spectral density of the klystron beam noise. This has been measured (SPS 37-22, Vol. III, p. 17) but only for a limited set of conditions. The exact form of the system depends on the results obtained from the initial work on the antenna and klystron beam noise.

2. Optimum Transmitter Power for Klystron Drive-Keyed Radar

a. Introduction. Recent experiments with a "tunneled" auxiliary antenna mounted at the apex of the 85-ft Venus site antenna indicate that it is possible to modify the present monostatic planetary radar system for lunar use. Fig. 37 shows a simplified block diagram of the modified system. The large antenna is used for transmitting and the auxiliary for receiving. The control turns the drive on to the klystron for a round-trip signal travel time and simultaneously turns the receiver off by turning off the local oscillator (LO). For the next round-trip time the klystron drive is turned off and the LO is turned on. The system depends on the isolation between the antennas to protect the maser when the transmitter is on and to reduce the noise from the klystron beam to an acceptable level at the receiver input when the receiver is on. It is not possible to switch the klystron beam with present equipment. The performance of the system is, of course, dependent on the isolation between the antennas, i.e., how much noise leaks into the receiver. The performance also depends on the power transmitted since an increase in power transmitted yields a corresponding increase in power received, but it also causes an increase in beam noise. The analysis of the performance of the system as a function of these parameters is the subject of this article.

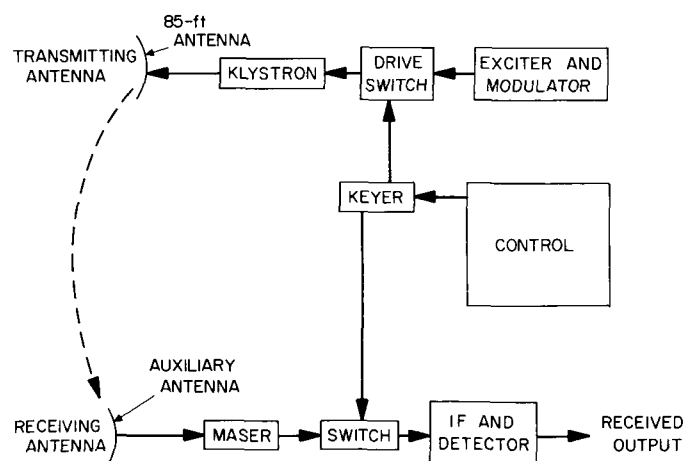


Fig. 37. Two-antenna klystron drive-keyed radar system

b. Analysis. The beam noise power increases as the klystron (carrier) output power is increased as shown in Fig. 38 (SPS 37-22, Vol. III, p. 22). The noise spectral density of the beam noise at the antenna terminal when the drive is off is approximated very closely by

$$N_k = \alpha P^x; \quad 10^4 \leq P \leq 10^5.$$

where P is the corresponding power output of the klystron with the drive on. From Fig. 38

$$\alpha = 5 \times 10^{-25}$$

and

$$x = 2.85$$

The total receiver system noise in a bandwidth, B , is

$$N = (kT + a\alpha P^x) B \quad (1)$$

for a given isolation, a , between antennas. The received signal power, given by the radar equation, is proportional to the transmitted power,

$$S = \eta \frac{G_{trans} A_{target} A_{rec}}{(4\pi R^2)^2} P = HP, \quad (2)$$

and the received signal-to-noise ratio is

$$\frac{S}{N} = \frac{H}{B} \frac{P}{kT + a\alpha P^x} \quad (3)$$

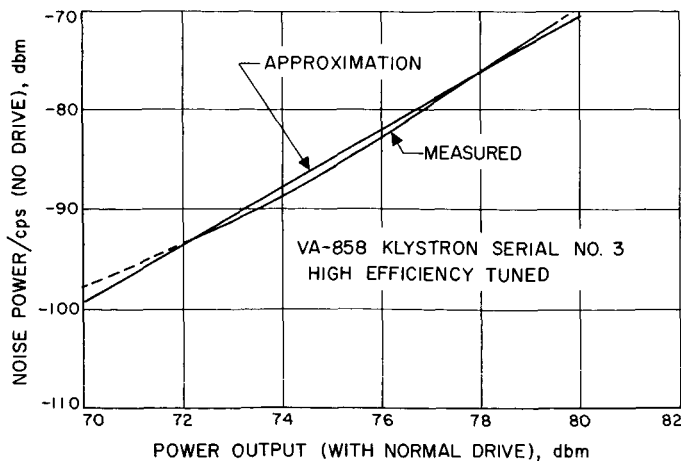


Fig. 38. Klystron noise power output with drive off, and function of carrier power output with drive on

Since $x > 1$, there is some value of P which maximizes S/N :

$$\frac{d(S/N)}{dP} = \frac{H}{B} \left(\frac{kT + a\alpha P^x - a\alpha x P^x}{(kT + a\alpha P^x)^2} \right) \quad (4)$$

This derivative is zero when $P = P_{opt}$, given by

$$P_{opt} = \left[\frac{kT}{a\alpha(x-1)} \right]^{1/x} = C_1 T^{1/x} a^{-1/x} \quad (5)$$

and the optimal signal-to-noise ratio is then

$$\begin{aligned} \left(\frac{S}{N} \right)_{opt} &= \frac{H}{B} \frac{1}{x a \alpha P_{opt}^{x-1}} \\ &= \frac{H}{B} \left(\frac{x-1}{kT} \right)^{(x-1)/x} \frac{1}{(a\alpha)^{1/x} x} \\ &= C_2 T^{(1-x)/x} a^{-1/x} \end{aligned} \quad (6)$$

As an example of the above analysis, let us compute the optimum transmitter power to be used on a two-antenna radar with the following parameters:

$$a = -90 \text{ db}$$

$$T = 100^\circ \text{K}$$

$$\alpha = 5 \times 10^{-25}$$

$$x = 2.85$$

$$k = 1.38 \times 10^{-23} \text{ w/cps (Boltzmann's constant)}$$

Then the optimum transmitter power is

$$\begin{aligned} P_{opt} &= \left[\frac{1.38 \times 10^{-23} \times 10^2}{1.85 \times 5 \times 10^{-25} \times 10^{-9}} \right]^{1/2.85} \\ &= 1.85 \times 10^4 \text{ w} \end{aligned} \quad (7)$$

Fig. 39 illustrates the optimum transmitter powers at various system temperatures for several values of isolation.

To further the example, let us assume a range-gated lunar radar echo using the following parameters:

$$G_{trans} = +53 \text{ db}$$

$$(85\text{-ft antenna})$$

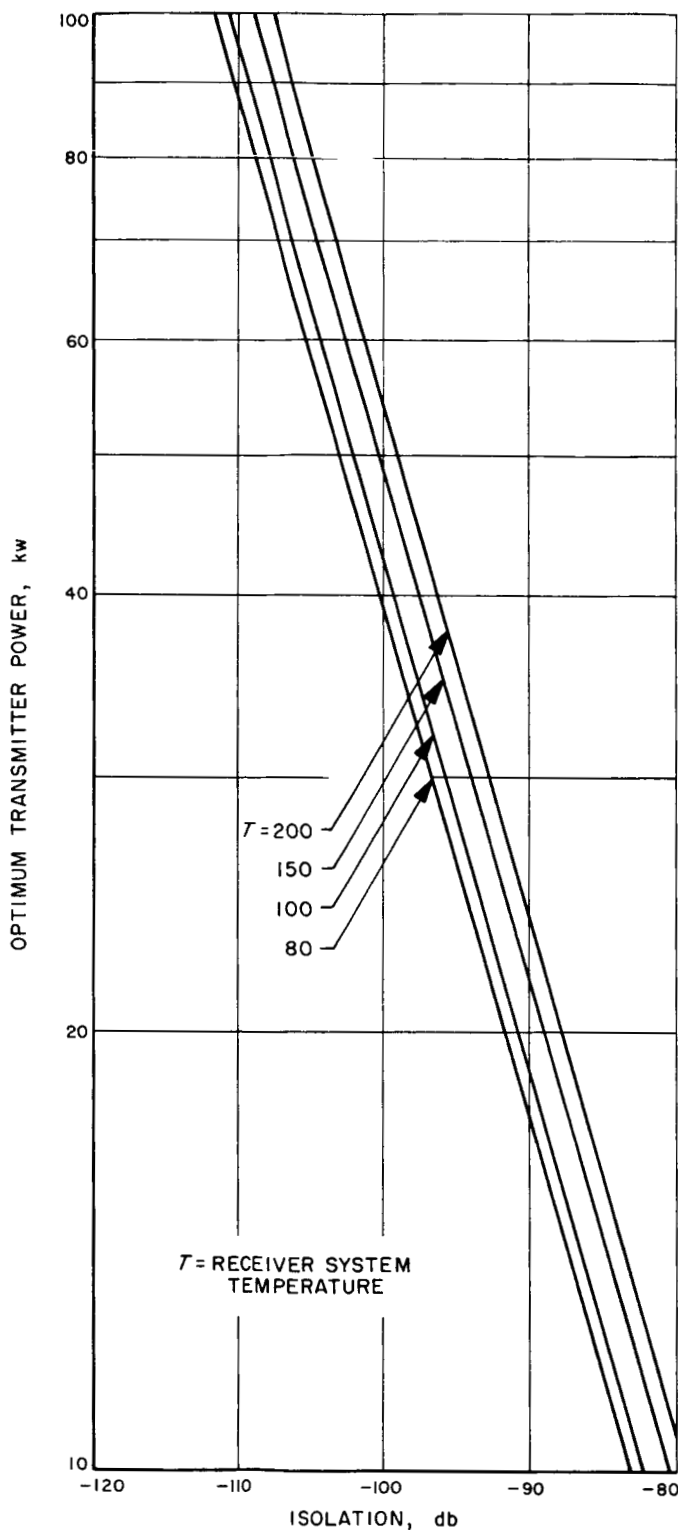


Fig. 39. Optimum transmitter power for klystron drive-keyed radar as a function of transmitter-receiver isolation

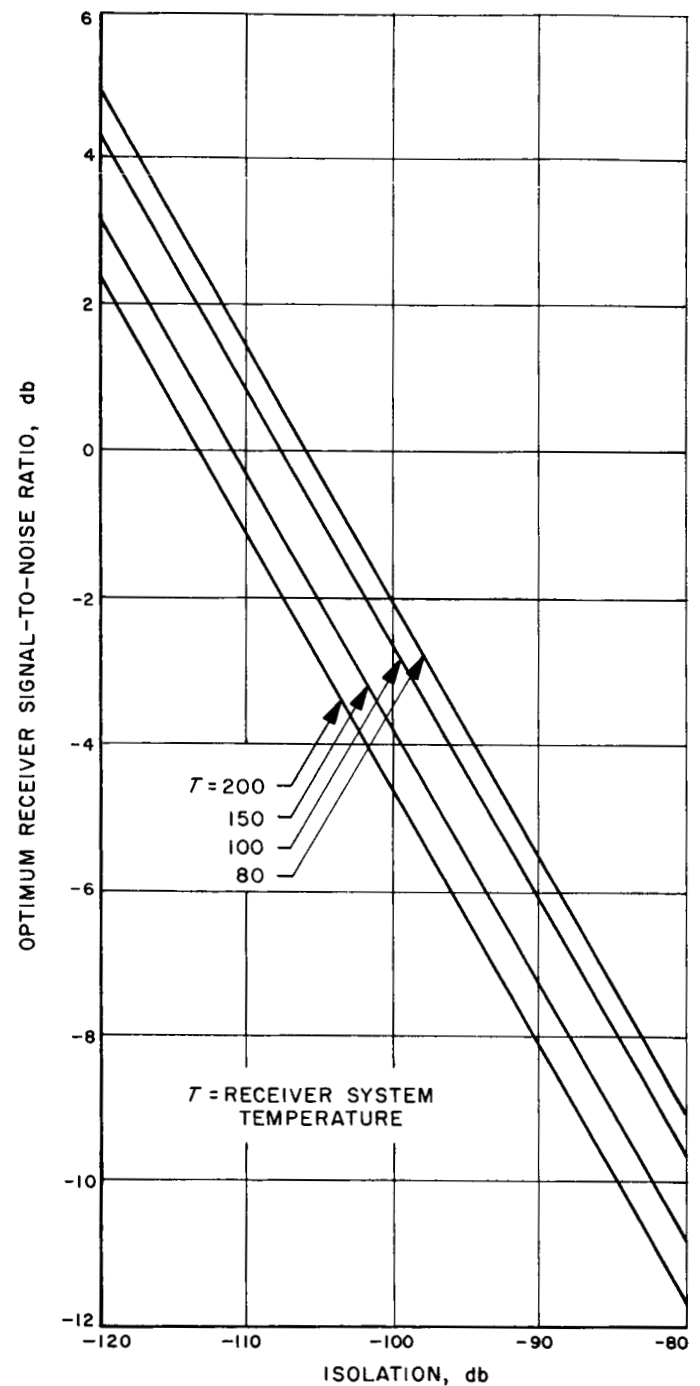


Fig. 40. Optimum received signal-to-noise ratio from a 150-m deep front cap of the Moon, as a function of transmitter-receiver isolation

$$A_{rec} = 1.25 \text{ m}^2$$

(6-ft antenna, +30-db gain)

$$A_{target} = \pi D l = 1.64 \times 10^9 \text{ m}^2$$

(effective area of 300-m deep front cap)

$D = 1738 \text{ km}$	(mean diameter)
$l = 150 \text{ m}$	(1-Mc code)
$R = 4.66 \times 10^8 \text{ m}$	(at apogee)
$\eta = 0.01$	(front cap albedo and system losses)
$B = 20 \text{ cps}$	(detection bandwidth)
$\lambda = 0.1255 \text{ m}$	(2388 Mc)
$T = 100^\circ\text{K}$	

Fig. 40 gives the optimum signal-to-noise ratio at the receiver as a function of isolation.

Fig. 41 shows the returned signal-to-noise ratio curves as a function of transmitted power for several values of isolation between antennas, to illustrate the behavior in the vicinity of the maximum. At a given system temperature, a 10-db improvement in isolation allows the transmitted power to be increased 3.51 db [Eq. (5)], and increases the signal-to-noise ratio by an equal amount, 3.51 db [Eq. (6)].

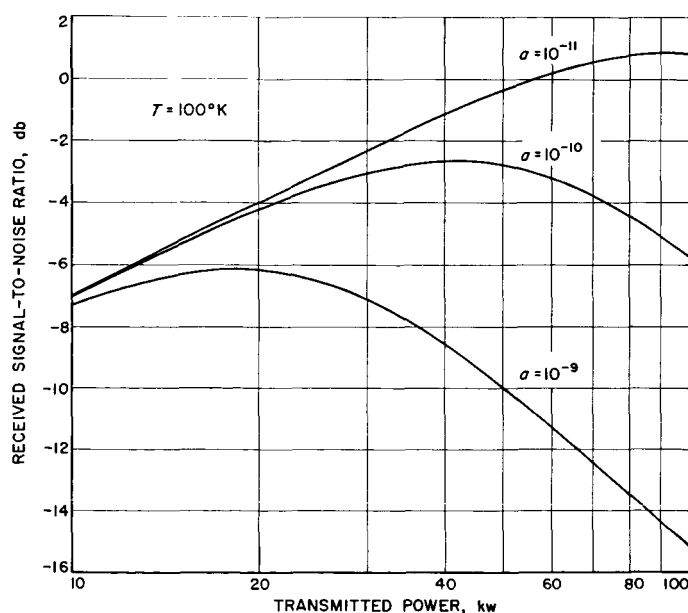


Fig. 41. Received signal-to-noise ratio from a 150-m front cap of the Moon for fixed transmitter-receiver isolation, as a function of transmitted power

D. Ranging System Development

1. Monostatic Radar

a. Résumé. Continuing effort in the problem areas (SPS 37-19, Vol. III, p. 29) associated with high-rate keying for the monostatic radar and rework of the Mod III receiver and exciter for this project are leading to a minimum field system necessary to prove feasibility of such a keyed radar. Refinements necessary for full sensitivity and satellite tracking data acquisition, such as a programmed local oscillator, receiver angle channels, and data extraction equipment are presently planned for a complete system to be operated at X-band at a later date.

b. Transmitter drive keying. With regard to the ability to key off the transmitter to a level below the receiver threshold during the receive cycle, further data has been obtained to confirm the extrapolation presented in SPS 37-19, Vol. III, Fig. 25. Specifically, a laboratory test setup, including a 3-w signal source and a calibrated receiver, was used in measuring the reduction of transmitter frequency multiplier output level as a function of multiplier input attenuation. The primary limitation of this measurement was the leakage present between the signal source and the receiver. While the system requires over 221-db transmitter turnoff capability for the previously determined 50-db UHF keying, this measurement to 140 db lends greater confidence in the extrapolated slope. See Fig. 42 for test results. Further verification will not be feasible until a low-noise, narrow-bandwidth receiver of typical leakage is available.

c. Oscillators and frequency references. The Mod III receiver and exciter were made available for this project without suitable UHF oscillators and references. Since the receiver must track full doppler shifts without aid of a programmed local oscillator, an adaptation of current designs for low phase noise oscillators is being developed to provide a stable oscillator with "wide swing" capability for use in the main receiver loop. The stable reference frequencies for the exciter and receiver will be obtained in the field from the planetary radar installation presently existing at the Venus site at Goldstone Tracking Station. The frequency synthesizer removed from the Mod III receiver and exciter is being adapted for use in system testing at the Laboratory.

d. Synchronous sideband detector. A means of rejection of spurious receiver locks to keying sidebands has been undergoing preliminary analysis and development (SPS 37-21, Vol. III, p. 81). Initial portions of this subsystem have been assembled for the monostatic radar.

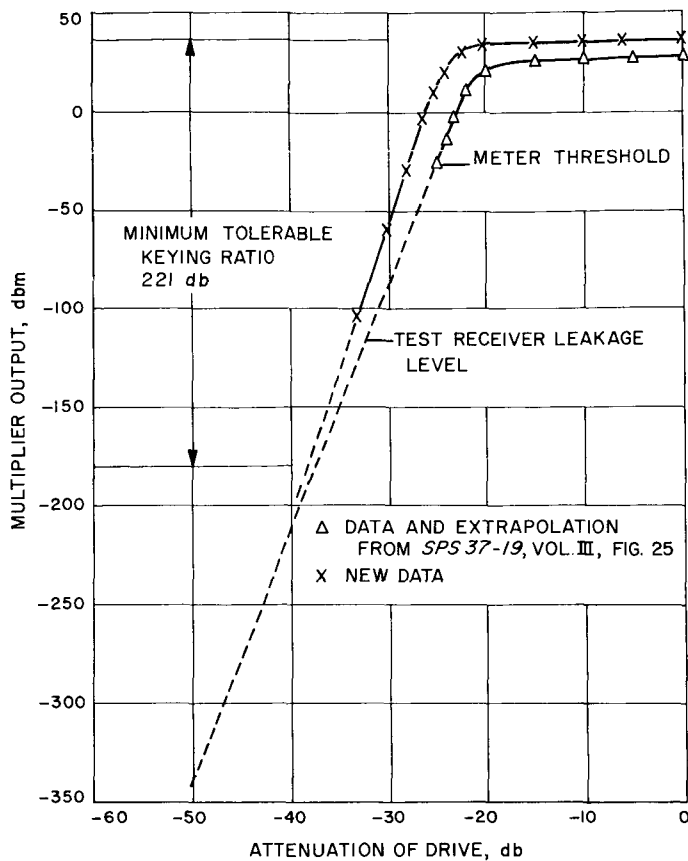


Fig. 42. Extrapolation of UHF frequency multiplier dynamic range

The operation of the synchronous detector is predicated upon the availability of a waveform equivalent to the receiver keying square wave, but delayed by 90 deg (Fig. 43). However, in the actual mechanization, this waveform must be delayed to compensate for the delay associated with the predetection filter. For typical

bandwidths, this delay, T , is of the order of 1 msec. A digital counter has been provided as a part of the keyer control to produce the compensating fixed delay (adjustable in 50- μ sec steps for optimization with a specific filter). It will be noted that, without this compensation, a 1-msec filter delay produces a phasing error of 36 deg at a keying rate of 100 cps.

While the above-mentioned filter delay appears to be adequately stable as a function of operating parameters, phase disturbances within the receiver loop as a function of keying rate cause an additional dephasing of the input signals to synchronous detector. Preliminary evidence suggests that this effect results both from imperfect phase integrity of the keyed frequency multipliers in the transmitter and receiver local oscillator and from partial tracking of the keying sidebands by the closed-loop receiver. At this time tests are incomplete, but the results emphasize the necessity of maintaining the lowest keying frequency well outside the closed-loop passband of the receiver.

2. Keyer Control for Monostatic Radar

The keyer control in a monostatic radar is the device which controls the time-sharing of the antenna between the transmitter and receiver. Its input is the estimated or measured range which is used to control the time sharing in such a way that the receiver is on only when there is a returning signal. The keyer control is designed to maximize the amount of information that is received. Previous keyers (Mod I-D Ranging System, SPS 37-15, Vol. III and Venus Radar System, SPS 37-21, Vol. III) have required an output to control the receiver and the negative of that output to control the transmitter. The

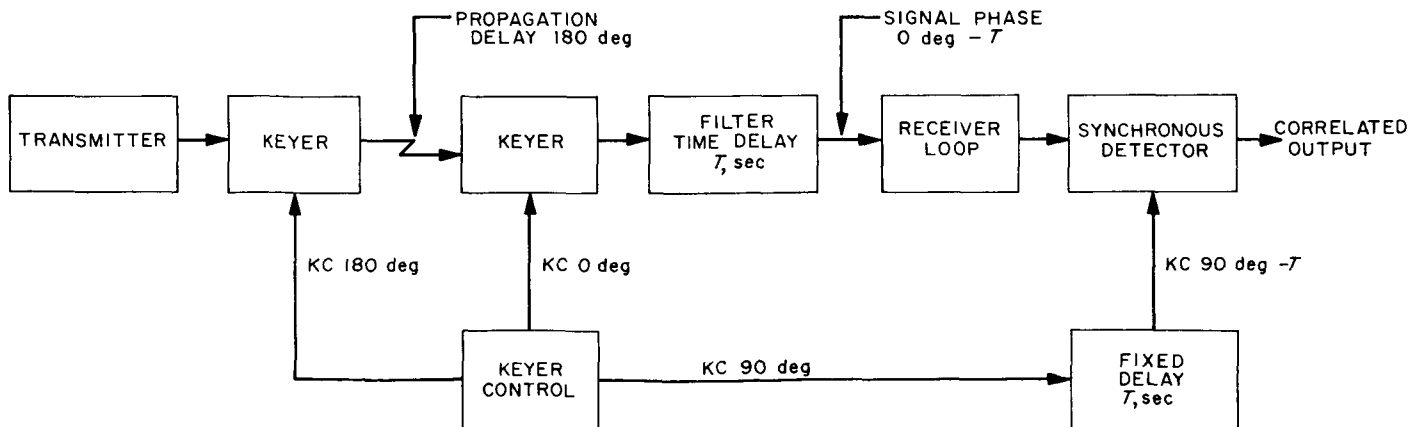


Fig. 43. Keyer control phase relationships

special anti-sideband locking device employed in the monostatic radar (SPS 37-21, Vol. III) requires a third output which, ideally, lags the receiver output in phase by 90 deg. Practically, the phase lag must be increased beyond 90 deg to allow for the delay in the receiver. The receiver delay can be determined only by experiment. A keyer control has been built and tested which provides the necessary three outputs and which has the delay of the third output, relative to the other two, adjustable over a limited range.

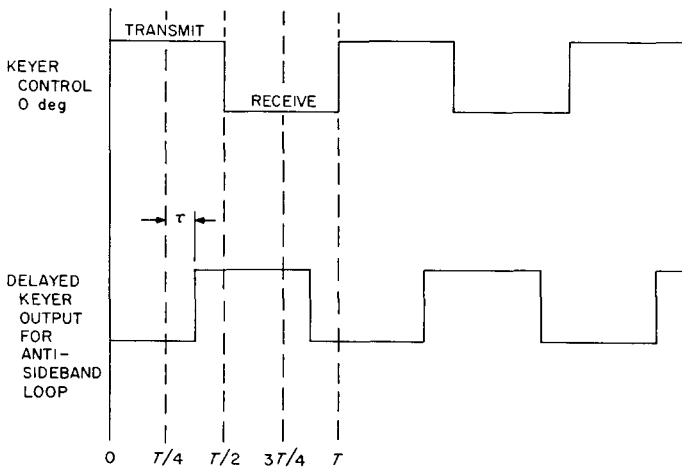


Fig. 44. Keyer control output signals

a. Description of the keyer. The relationship of the auxiliary output to the primary output of the keyer is shown in Fig. 44. The additional time delay, τ , which is due mostly to the delay in the second IF amplifier seems, from preliminary measurements, to be relatively constant at 1 or 2 msec. Additional measurements are being made to establish the value of τ precisely. These measurements are best made by comparing the performance for various values of τ , hence the requirement for a keyer control with an adjustable time delay.

At this writing definitive conclusions regarding the optimum value of τ have not been reached. The remainder of this article is devoted to a description of the keyer control designed to assist in the experimental work.

Fig. 45 shows the keyer control designed to provide conventional as well as delayed outputs. The range number is entered into the range accumulator via a subtractor. The output of the range accumulator is fed back into the subtractor so that the number is continually circulating. Upon each pass through the subtractor a constant, called a countdown number, is subtracted from the range. When the range has been completely counted down, the number in the range accumulator becomes negative, activating the negative detector. A new range number is then entered into the range accumulator, and the process

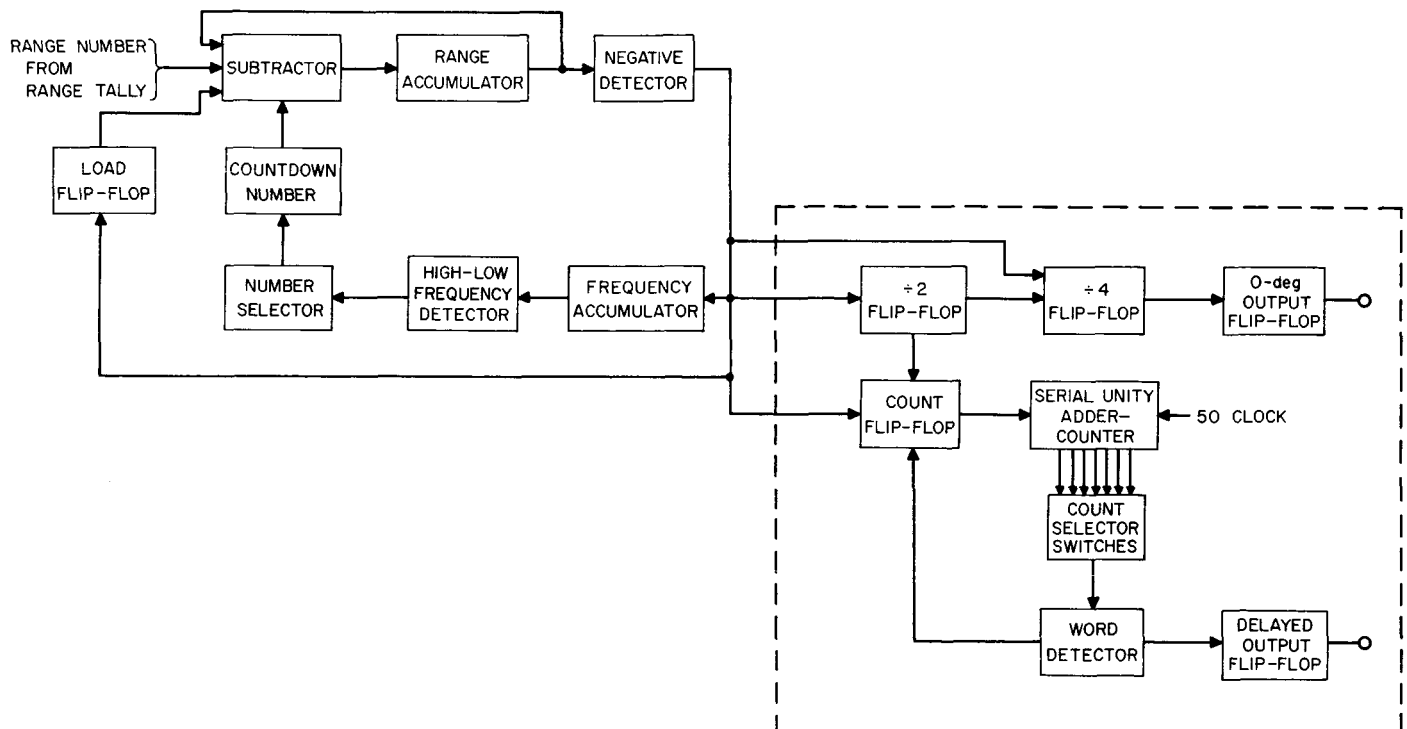


Fig. 45. Keyer control block diagram

is repeated. The rate at which the negative detector fires is constantly monitored by a frequency accumulator and a high-low frequency detector. If the negative detector frequency, which is proportional to the keying frequency, passes beyond the bounds prescribed by the system design, the countdown number is adjusted. Enlarging the countdown number increases the countdown rate and results in a higher keying frequency, while decreasing the number has the converse effect. A more thorough discussion of this conventional section of the keyer control may be found in SPS 37-15, Vol. III.

Those modifications to the keyer control which provide an adjustable, delayed output are enclosed by dotted lines in Fig. 45. The output from the negative detector enters a series of two flip-flops. The first divides the negative detector frequency by two, and the second causes it to be divided by four. The results of these divisions are shown in Fig. 46. Two divide flip-flops are necessary to establish the quadrature relationship for the delayed keyer signal. The second flip-flop ($\div 4$) is taken as the reference and is used to drive the 0-deg output flip-flop directly.

Each time that the negative detector fires, and the divide-by-two flip-flop is in the zero position, a counter is started. This is equivalent to starting the counter at the 90-deg point relative to the reference. The counter advances at 50- μ sec intervals until a preset number has been reached. At this time the serial unity adder word

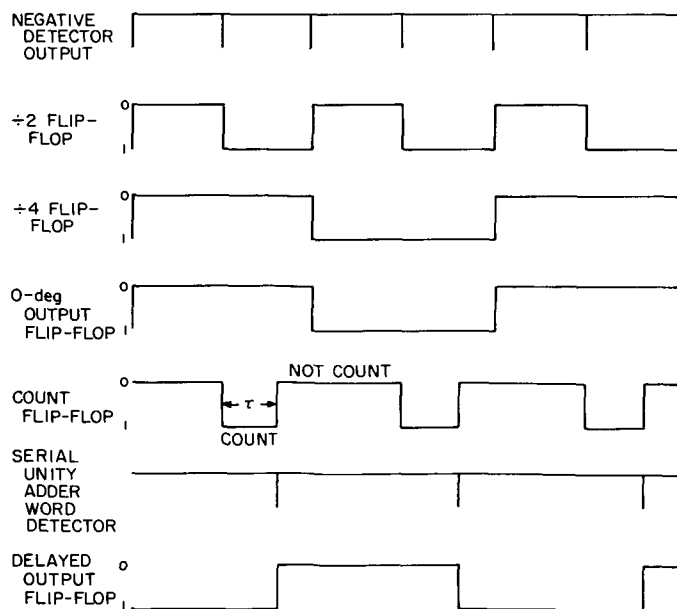


Fig. 46. Timing chart

detector is energized and causes the counter to be reset and the delayed output flip-flop to be complemented. A bank of switches allows the count interval, and hence τ to be selected by the operator.

A laboratory model was constructed which provided delays ranging from $\tau = 0$ to $\tau = 25.6$ msec in 50- μ sec steps. The delayed output is constrained to phase shifts of not more than 180 deg, because a single counter is used both to set and to reset the delayed output flip-flop. A slightly more versatile, but larger, machine could embody two counters: one to set and the other to reset the flip-flop. Splitting the load in this manner would allow phase shifts of up to 360 deg, which may be necessary at higher keying rates.

E. S-Band Implementation for DSIF

1. TWM for DSIF

a. Summary. We plan to equip the DSIF with traveling wave masers (TWM's) in closed cycle refrigerators (CCR) as part of the S-band implementation program. A total of six systems will be required which involves a large fabrication program. Because of the large number of systems involved we will subcontract various portions of the task to commercial engineering firms; system integration will be performed at JPL. Work on an experimental prototype TWM has been reported in previous issues of this summary.

b. Recent work. In order to facilitate the reporting of the progress on this project the total effort will be divided into 11 tasks as follows:

(1) *Technical problems.* Various problems associated with the TWM will be discussed in this section.

A common observation in the operation of maser pre-amplifiers has been the generation of spurious signals when the maser pump-klystron is tuned to some particular frequency. This spurious signal generally causes no problems since it can be eliminated by properly tuning the klystron. However, an understanding of the mechanism by which the signal is generated is of great importance if one is to operate masers with confidence.

It has been found that the mysterious signal is generated in the mixer of the receiver through harmonic mixing. The n th harmonic of the receiver local oscillator can beat with the m th harmonic of the pump-klystron in the mixer and produce the difference frequency Δf :

$$\Delta f = nf_{Lo} - mf_p$$

where

f_{Lo} = local oscillator frequency

f_p = maser pump frequency

Clearly if Δf is within the passband of the receiver IF amplifier, a signal will be observed. It is to be noted that, even if the local oscillator generated no harmonics, the inherent nonlinear property of the mixer can produce harmonic mixing. The phenomenon observed is certainly not new; however, it is interesting to note that in recent developmental testing we discovered that the eleventh harmonic of the S-band local oscillator was mixing with the second harmonic of the KU band pump klystron to produce an interference. Fortunately, with an understanding of the problem it is a simple matter to tune the klystron to an optimum frequency.

(2) *Closed cycle refrigerator (CCR)*. As a result of the continuing successful performance of the prototype A. D. Little Cryodyne, it is planned to use this CCR for the operational TWM system. Even better performance is expected with a few improvements to be incorporated in the new CCR's. In particular, a set of gears used to produce a squarewave drive on a set of pistons will be eliminated in favor of a low-speed induction motor drive.

Soft-solder joints caused leak problems in the prototype CCR; the troublesome joining methods for critical joints are being eliminated. The external appearance and dimensions of the refrigerator will be similar to the prototype.

(3) *TWM structure*. This structure consists of a comb structure, active ruby material, and passive ferrite material. The performance specifications for the TWM were given in SPS 37-22, Vol. III.

The Airborne Instruments Laboratory and Microwave Electronics Corporation have demonstrated capabilities in this particular area and were invited to submit proposals to fabricate these devices. A contract will be negotiated in the near future for the initial three units and a spare.

(4) *Microwave head*. The transmission line assembly which carries signal and pump powers into the maser structure is referred to as the microwave head. This is a crucial component in the entire assembly since low electrical losses are required concomitantly with very high thermal insulation for cryogenic reasons. In addition, the transmission lines must all be vacuum tight for operation in the CCR.

Four of these units were recently fabricated using stainless steel tubing for coaxial lines and Teflon as insulator. The coaxial lines were plated with copper and gold to minimize electrical losses while retaining the high thermal resistivity of stainless steel. All units were checked out to have input and output VSWR's of 1.10 or better, and the signal input line had an insertion loss of about 0.10 db. Since a great portion of the line will operate at temperatures well below ambient value, the effective noise temperature contribution of the line will be only 3 to 4°K.

(5) *Magnet assembly*. The magnet assembly is regarded as an integral part of the TWM structure; it is expected that the same manufacturer will be asked to fabricate both units.

Although TWM's have been operated in superconducting magnets in various laboratories, it does not appear advisable at present to attempt to use these in field operational masers. Experience has shown that permanent magnets with trim coils are adequate and very reliable.

A principal requirement for a good magnet is temperature compensation for good stability; or, alternatively, the magnet may be kept at constant temperature. We plan to pursue the latter in the DSIF TWM system.

(6) *Pump assembly*. The TWM pump assembly consists of a VA 246 Varian klystron (pre-tuned at the factory to 12.7 Gc), a ferrite isolator, a remotely controlled waveguide switch, a manually controlled variable attenuator, and a directional coupler with a detector mount for monitoring the klystron output.

Tests have indicated that the VA 246 is sufficiently stable so that only temperature regulation of the klystron is required. This is readily achieved by controlling the temperature of the waveguide flange which also serves as heat-sink for the klystron. Another attractive feature of the VA 246 is that no oil bath is required; this, coupled with the factory pretuning, will greatly simplify the maintenance of the pump package in the field.

In order to reduce detuning effects during calibration tests, a waveguide switch is used to divert power from the TWM. This permits continuous operation of the klystron for optimum stability.

The manually controlled attenuator will be used to set the pump power for saturated operation of the TWM without overloading the CCR.

(7) *Monitor receiver.* Standard DSIF S-band receiver modules have been tested for use in the monitor receiver for the TWM subsystem and found to be completely adequate. It is mandatory to use the best available power supplies to achieve the required stability.

(8) *Control rack.* The control rack will contain virtually all the components required to operate the TWM and CCR. Wiring of the racks has begun and components have been ordered.

The TWM control panel and the CCR control panel have been designed and are being fabricated.

(9) *Monitor rack.* The monitor rack will contain the equipment necessary to measure the electrical performance of the TWM. Wiring of the racks has started and practically all components have been ordered.

A switching panel and a detector panel have been designed and are being fabricated.

(10) *TWM package.* The approximate configuration and dimensions for the cone-mounted equipment have been submitted to the microwave subsystem group for integration into a quarter-scale model of the cassegrain cone.

In order to facilitate final packaging of the TWM assembly it is planned to fabricate a full scale model of the assembly. A few of the components have been fabricated for the mock-up and assembly will begin shortly.

(11) *Prototype system field testing.* Various versions of a prototype S-band TWM and CCR have been tested at Goldstone, e.g., 10-kw diplexing tests. To aid the DSIF development program a 2.4-Gc version of the TWM and the original prototype CCR will be used in the next planetary-lunar radar experiment series at the Goldstone Venus site. The installation of the equipment on the 85-ft az-el antenna is nearly complete. The TWM unit was recently tested with the CCR in the laboratory before shipment to Goldstone; its performance as tuned for

use in the radar receiver was: 38-db gain, 12-Mc bandwidth, $\approx 10^\circ\text{K}$ noise temperature.

2. S-Band Acquisition Aid for the DSIF

a. Summary. An acquisition aid is being designed for the DSIF 85-ft antennas at S-band. The design concept is discussed.

b. Recent work. The basic purpose of an acquisition aid system is to provide a reliable means of acquiring a spacecraft in a poorly defined orbit with the 85-ft antennas at the DSIF Stations, as soon as possible after line of sight visibility of the spacecraft. Such a system, operating at L-band, has been utilized in support of *Ranger* and *Mariner A* missions. As described in *SPS 37-14*, Vol. I, April 1, 1962, this L-band system consisted of a small, low-gain monopulse antenna mounted on, and boresighted with, the 85-ft antenna, together with the necessary receiver and servo system switching circuitry. Using this system, rough automatic tracking was achieved shortly after appearance of the spacecraft, and switchover to the main 85-ft monopulse tracking was accomplished shortly thereafter.

With the impending conversion of the DSIF to S-band, a requirement has arisen for an S-band acquisition aid system, and it is planned to utilize the same general approach as that employed at L-band. A prototype S-band acquisition antenna (SAA) has been described previously (*SPS 37-20*, Vol. II, March 31, 1963, pp. 15-17). This SAA is a multimode, single horn monopulse antenna similar to that which will be used as the DSIF feedhorn in the main 85-ft, S-band cassegrainian feed system. The SAA will be right-hand circularly polarized, have a full half power beamwidth of approximately 16 deg, and have the capability of simultaneous low noise reception at 2295 Mc and higher power (10 kw, CW) transmission at 2113 Mc. It will be mounted in the main antenna backup structure, approximately halfway out to the antenna rim, and with its aperture (approximately 2 ft²) near the surface of the main antenna. Associated equipment, also to be mounted in this region includes a diplexer, filters, and manually operable switches to change the SAA sense of polarization.

Because of the extremely small beamwidth of the main antenna at S-band (approximately 0.3 deg), and the anticipated rough tracking with the SAA due to ground multipath effects, a dual receiver will be utilized with the S-band system. A complete three-channel receiver will be used in conjunction with the main antenna simultaneously with the SAA subsystem three-channel receiver.

In this way, it will be possible to display to the operator both the main antenna and SAA alignment at all times. Under these conditions it is felt that the operator will always be able to effect rapid and completely reliable antenna switchover.

Detailed system design is presently being carried out for the acquisition aid system and related equipment. The principal construction will be done under subcontract to a commercial engineering firm; negotiations to establish the contract are in progress.

References

1. Hogg, D. C., *Journal of Applied Physics*, Vol. 30, p. 1417, September 1959.
2. *MIT Radiation Laboratory Series*, Vol. 18, p. 440.
3. Silver, S., "Microwave Antenna Theory and Design," *MIT Radiation Laboratory Series*, Vol. 12, pp. 423-425, McGraw-Hill Book Company, New York, N. Y., 1949.
4. "Radar Exploration of Venus: Goldstone Observatory Report for October-December 1962," Technical Report No. 32-396, Jet Propulsion Laboratory, Pasadena, California, to be published.
5. Victor, W. K., and Brockman, M. H., "The Application of Linear Servo Theory to the Design of AGC Loops," External Publication No. 386, Jet Propulsion Laboratory, Pasadena, California.

V. Advanced Antenna System

A. Synopsis

The Advanced Antenna System (AAS) will be a 210-ft diameter, fully steerable paraboloid. It is being designed for operational use at the DSIF Stations at the DSIF S-band frequencies (2.1 to 2.3 Gc).

The principal element of the first AAS, which we term the Contractor Furnished System (CFS), includes the reflector, alidade, pedestal, foundation and drive system. It has been under contract to the Rohr Corporation since mid-June of this year. Engineering design on all phases of the CFS is underway at the contractor's facility and at his several subcontractors. Work on the second element of the AAS, which includes site facilities and utilities, is now underway; architect and engineering requirements for the road to the AAS site (the Mars site at Goldstone) have been prepared; detailed specifications for the on-site power generating equipment are being finalized.

Supporting engineering studies at JPL and under sub-contract are continuing. This report includes discussions of: modifications to the rms optical path length error computer program; modifications to the use of the STAIR program for more versatility in calculating reflector distortion from wind loads; additions to the computer analysis of AAS type hydrostatic bearings; techniques for analyzing the deflection of the hydrostatic bearing runner and its support; and basic techniques for dynamic analysis.

B. Supporting Studies

1. Computer Studies

a. Root mean square program.

Summary. The root mean square (rms) program has been developed for calculation of the rms error in optical path length of an imperfect antenna reflector. Originally the calculation did not consider the noncoincidence of the apparent point of RF wave emission (apparent feed) and the focal point of the paraboloidal antenna reflector. Recent computer studies have shown that motion of the apparent feed contributes significantly to the rms value, displacement along the axis of revolution yielding a larger rms value than an equal displacement perpendicular to the axis of revolution.

Recent work. The computer studies were performed considering 961 points on a perfect paraboloid of 210-ft diameter and a focal-length-to-diameter ratio of 0.4235. Since all paths of ray propagation passing a far field point are parallel and of equal length as measured from the perfect paraboloid focal-feed point, it was assumed that the rays reflected from the paraboloid, with a given apparent feed deviation from the focal point, were also parallel. The path length errors (λ) of the rays emitted by the apparent feed point were calculated by mathematically placing a plane in space perpendicular to the ray reflected from the paraboloid vertex and adding the vector lengths from apparent feed to reflector point (i)

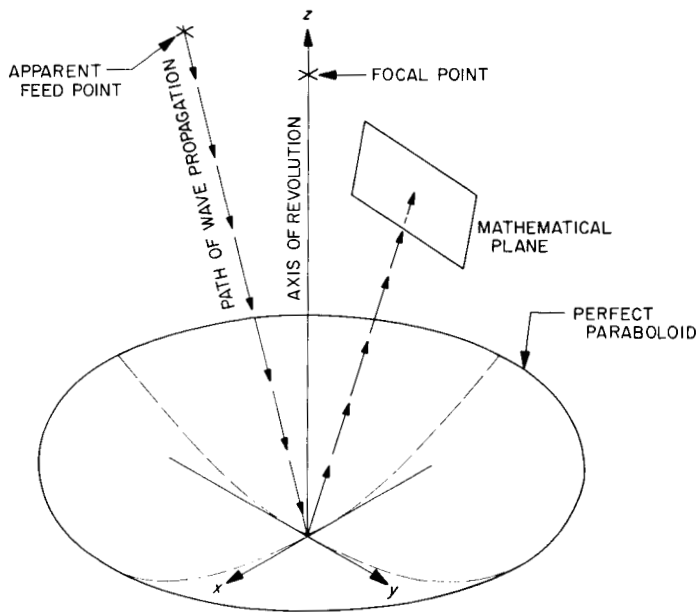


Fig. 1. Geometry for distorted reflector calculations

and from the reflector point (i) to the mathematic plane and then comparing this sum to the standard used to set the mathematic plane. The geometry is shown in Fig. 1. The rms of lambda was calculated using the following formula:

$$rms = \left(\frac{\sum_{i=1}^n A_i \lambda_i}{\sum_{i=1}^n A_i} \right)^{1/2}$$

where

A_i = reflector area associated with the i th path

λ_i = i th path length error

Comparison of the curves of Figs. 2 and 3 shows the relative importance of parallel and perpendicular motion of the apparent feed and its effect on the rms value. The curves of Figs. 3 through 7 show the rms variation as a function of the apparent feed motion perpendicular to the axis of revolution at a fixed feed offset along the axis of revolution.

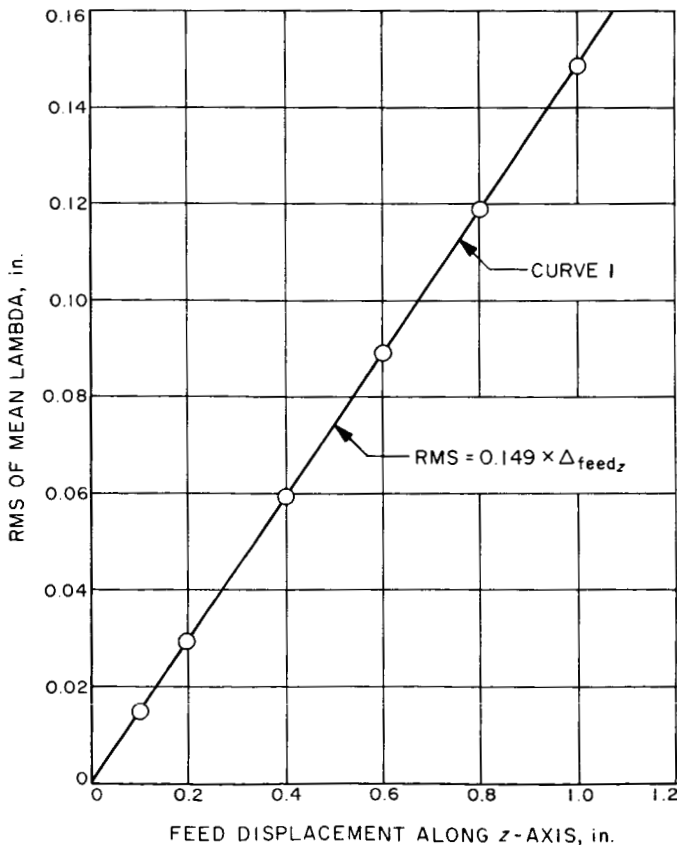


Fig. 2. Rms of mean lambda versus feed displacement along z-axis

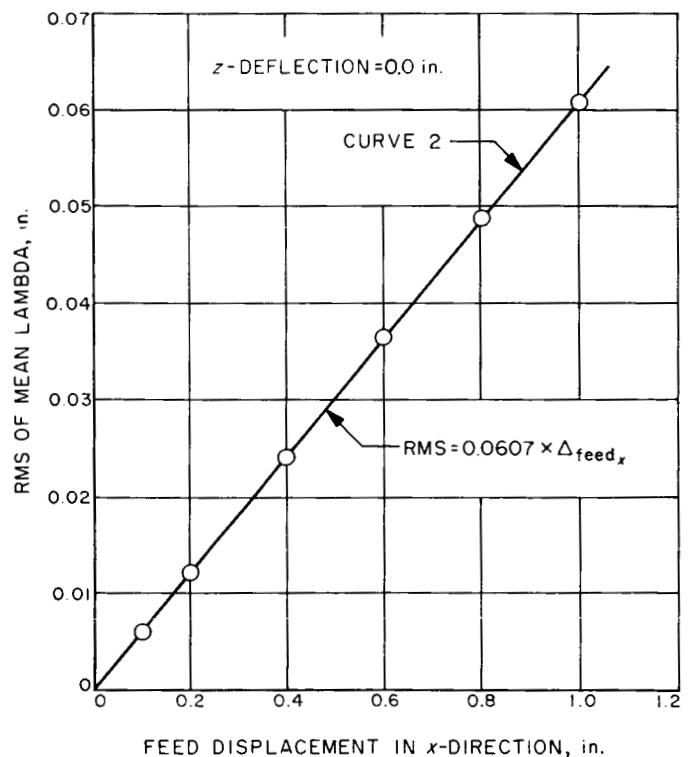


Fig. 3. Rms of mean lambda versus feed displacement in x-direction; z-deflection = 0.0 in.

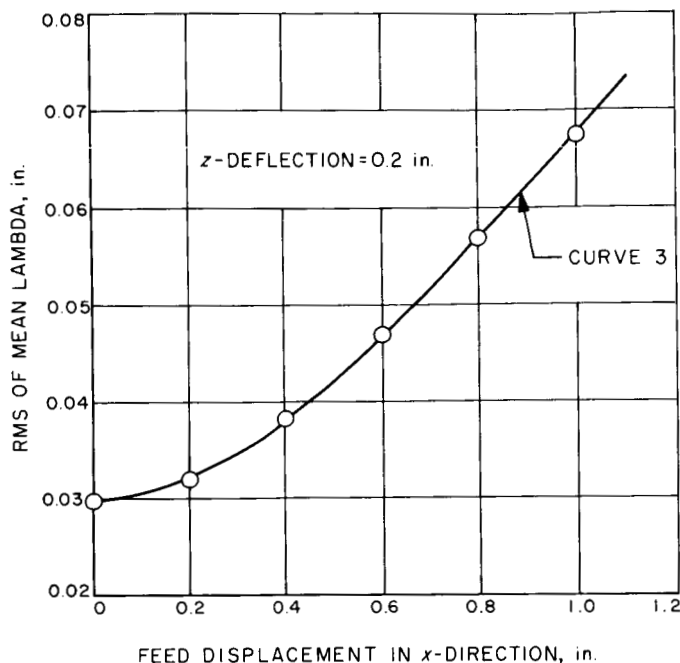


Fig. 4. Rms of mean lambda versus feed displacement in x -direction: z -deflection = 0.2 in.

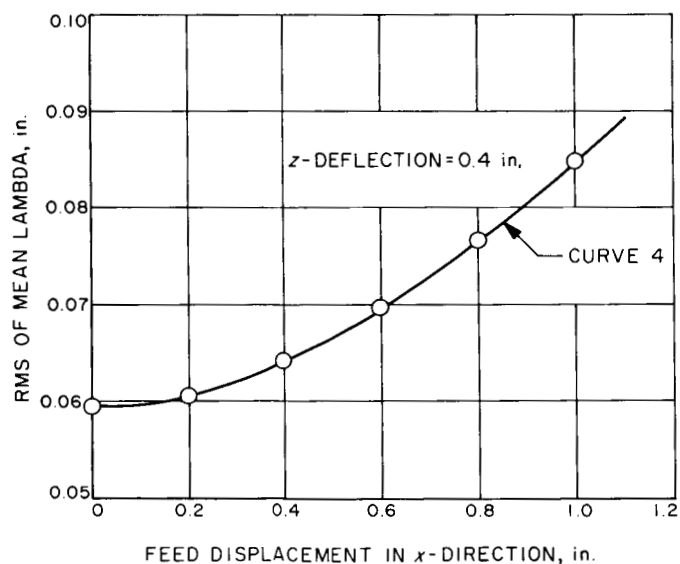


Fig. 5. Rms of mean lambda versus feed displacement in x -direction: z -deflection = 0.4 in.

In light of the above results, the rms program is being modified to calculate a rms of one-half the path length errors as seen from the apparent feed.

b. Wind loads.

Summary. The techniques for using large digital computers to calculate structural deflection in large antennas

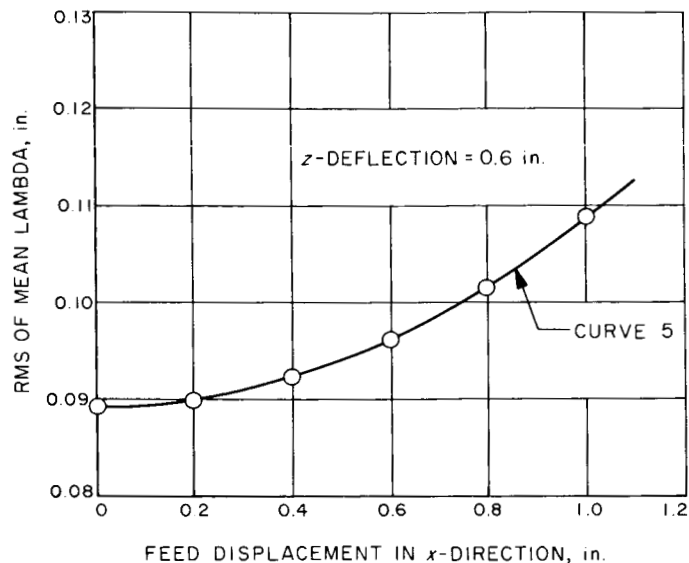


Fig. 6. Rms of mean lambda versus feed displacement in x -direction: z -deflection = 0.6 in.

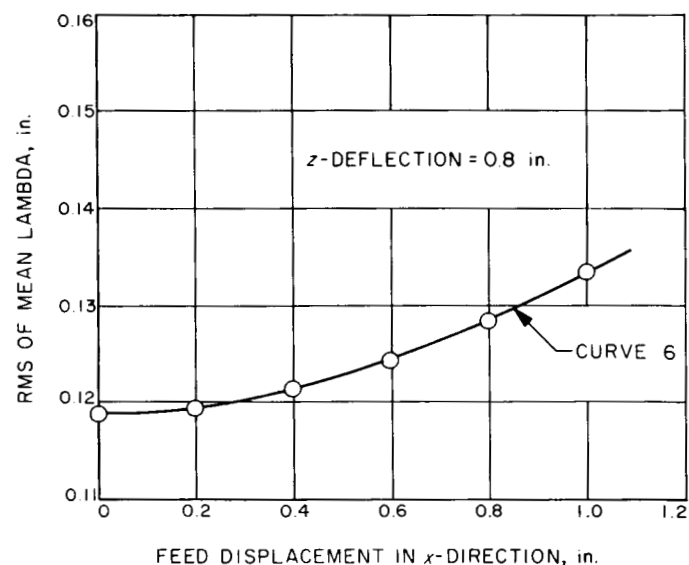


Fig. 7. Rms of mean lambda versus feed displacement in x -direction: z -deflection = 0.8 in.

have been studied in relation to the AAS and the other antennas in the DSIF. In SPS 37-17, Vol. III, a method was described for calculating the joint deflections and bar stresses of the reflector structure caused by wind loads using the STAIR computer program; the method used one-quarter of the 210-ft dish structure. The previous analysis was limited to wind directions either parallel or at right angle (90 deg) to the elevation axis. In other words, the wind direction was parallel to a plane of

symmetry of the structure which resulted in wind loads symmetrical about the planes of symmetry.

A computation method, for calculating the joint deflections and bar stresses of a reflector structure from an unsymmetrical wind load using the Structural Analysis Interpretive Routine (STAIR) computer program and only one-quarter of the structure, has been developed.

Recent work. The computation for joint deflections and bar stresses increases in complexity for a wind direction at an angle to the planes of symmetries. If only a one-quarter section is available for computer analysis, four separate computer runs are required with appropriate restraints on the joints in the cutting planes of symmetries. In order to simplify the computation, a digital computer program has been coded to compute the four load inputs. Another simple program has been coded to sum the four computer outputs into the one output required.

Given a reflector structure assembly which is symmetrical separately about the x and y coordinate axes as shown in Fig. 8, a wind load (F_1 , F_2 , F_3 , and F_4 which are not equal to each other) is considered to be applied to points P_1 , P_2 , P_3 , and P_4 . The four loading points must be symmetrically located separately to the two axes. Since the wind loads act at right angles to the surface, the directions of the force vectors at the points P_1 , P_2 , P_3 , and P_4 will also be symmetrical to the axes and intersect at one point on the z -axis.

With only one-quarter of the reflector structure (quadrant 1) available for computer analysis, the restraint conditions on the joints in the x and y cutting planes will determine the loading to be used. Fig. 9 shows the equivalences between a loading on a one-quarter section and on the whole structure as determined by the restraint conditions (Ref. 1). Since the directions of the force vectors in the four quadrants are symmetrical, the magnitudes of the forces can be added directly without using components.

The principle of superposition is applied in the summation of forces shown in Fig. 9. For example in (a) Fig. 9, a load $F_3/4$ applied in the third quadrant appears as an equal load $F_3/4$ in all quadrants. Thus, all four forces applied separately to each quadrant will appear in the first quadrant as

$$FSS = \frac{F_1}{4} + \frac{F_2}{4} + \frac{F_3}{4} + \frac{F_4}{4}$$

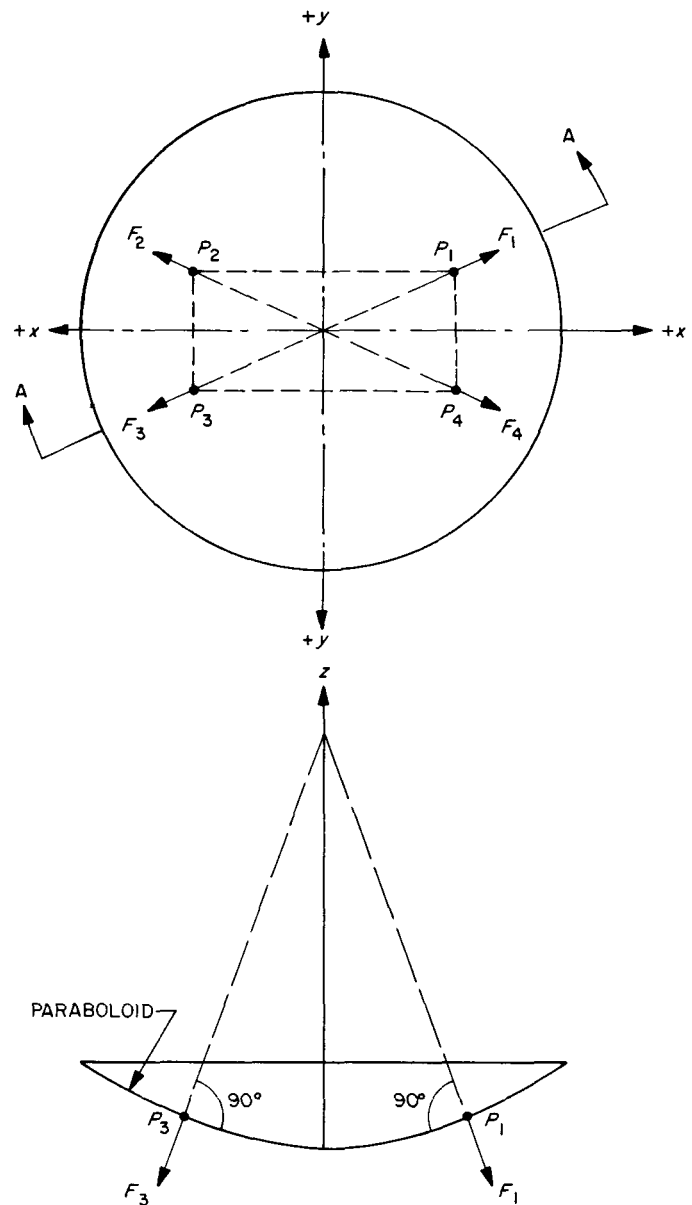


Fig. 8. Symmetrical reflector diagram

Similarly, in (c) of Fig. 9, where the restraints are symmetric in the y -plane and antisymmetric in the x -plane, a $+F_3/4$ force applied in the third quadrant appears as a $-F_3/4$ force in the first quadrant and the resulting sum

$$FAS = \frac{F_1}{4} + \frac{F_2}{4} - \frac{F_3}{4} - \frac{F_4}{4}$$

The resulting four equations provide the necessary loads for the four computer runs, FSS , FSA , FAS , and FAA :

$$FSS = \frac{F_1}{4} + \frac{F_2}{4} + \frac{F_3}{4} + \frac{F_4}{4}$$

$$FSA = \frac{F_1}{4} - \frac{F_2}{4} - \frac{F_3}{4} + \frac{F_4}{4}$$

$$FAS = \frac{F_1}{4} + \frac{F_2}{4} - \frac{F_3}{4} - \frac{F_4}{4}$$

$$FAA = \frac{F_1}{4} - \frac{F_2}{4} + \frac{F_3}{4} - \frac{F_4}{4}$$

The above equations reduce by addition and subtraction to:

$$F_1 = FSS + FSA + FAS + FAA$$

= first quadrant solution

$$F_2 = FSS - FSA + FAS - FAA$$

= second quadrant solution

$$F_3 = FSS - FSA - FAS + FAA$$

= third quadrant solution

$$F_4 = FSS + FSA - FAS - FAA$$

= fourth quadrant solution

Finally, the computation carried out for the wind loads on the four symmetrically located points P_1 , P_2 , P_3 , and P_4 can be applied to any number of four symmetrically

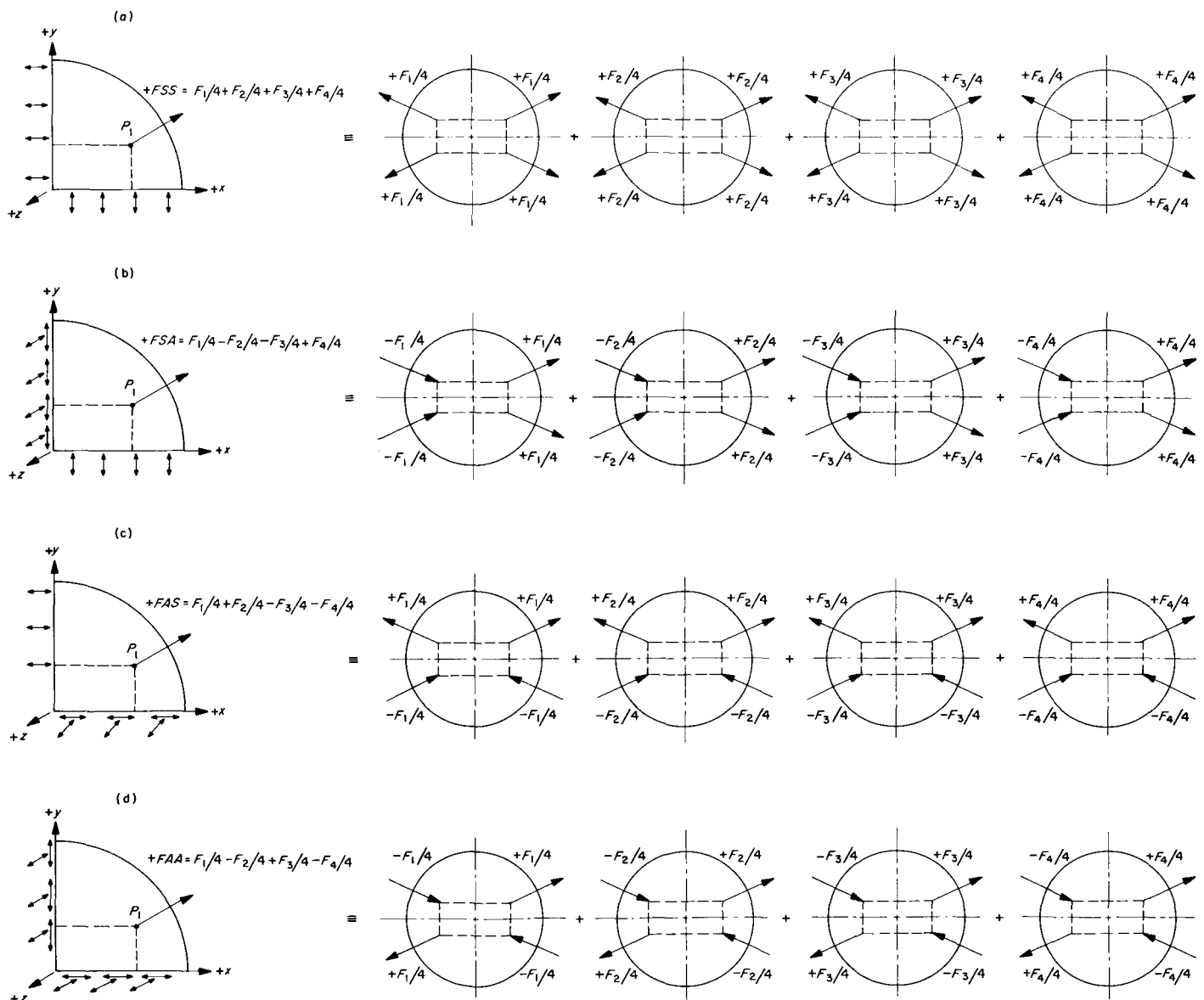


Fig. 9. Reflector section loading and constraint diagrams

located points. The computational technique has been applied to a test problem and will be reported in the following issue of SPS.

2. Progress in Hydrostatic Bearing Analysis Program

a. Summary. Analytical studies applicable to the AAS hydrostatic bearing are being conducted. Recent work on the Franklin Institute Hydrostatic Bearing Computer Program has been centered on debugging program revisions and in further analysis of the deflection characteristics of the runner on an elastic foundation.

b. Recent work.

Computer program revisions. Program revisions, made by The Franklin Institute, include the following:

- (1) The number of iterations available in the solution of Reynolds' equation has been increased from 300 to 1,000, making the use of the smaller available grid meshes practical, if their use is required by the pad configuration.
- (2) A nonhomogeneous term, representing the velocity of the bearing along the runner, has been included in the Reynolds equation. This term is significant when the velocity term is large and when the pad and runner are not parallel. In effect, it adds the characteristics of a hydrodynamic bearing to the hydrostatic bearing.

The revised program is now running satisfactorily and is being used in the design of the AAS by the contractor (Rohr Corp.). In addition, a series of runs is being prepared from which the effects of tilt, runner deflection, and velocity on bearing design can be summarized.

Deflection analysis. Work on the problem of the deflection of the runner on an elastic foundation has been carried on by JPL and the Franklin Institute. The problem centers on the use of a foundation modulus, K , in the elementary theory equation given by Hetenyi (Ref. 2). The theory considers the deflection and moments of a beam on a semi-infinite elastic foundation under a concentrated load in the form

$$y = \frac{P\lambda}{2K} e^{-\lambda x} (\cos \lambda x + \sin \lambda x) \quad (1a)$$

$$M = -\frac{P}{4\lambda EI} e^{-\lambda x} (\cos \lambda x + \sin \lambda x) \quad (1b)$$

where

$$\lambda = \sqrt[4]{K/4EI}$$

y = deflection of a point which is a distance x from the load point

M = bending moment in the beam at x

P = concentrated load applied to the beam

EI = flexural rigidity of the beam

K = foundation modulus, force per unit deflection at the point of application of a load on the foundation.

The solution is based on the assumption that the deflection at any point on the foundation is due to the load at that point only and is completely independent of the load at other points. This assumption is useful in obtaining a simple mathematical solution to the flexure equation. In a real continuous foundation this assumption is not valid because continuity requires that a load at one point must cause deflections at adjacent points as well as at the load point. Hence, the required K cannot be obtained directly from ordinary elasticity relations.

M. A. Biot (Ref. 3) developed an approach based on the theory of elasticity in which the basic load is a cosine function, and an actual load is represented as a Fourier integral. For the simple case of a concentrated load, he derives equations for the moments and deflections as follows:

$$M(x) = \frac{Pa}{\pi} \int_0^\infty \frac{\alpha \cos[\alpha(x/a)]}{\alpha^3 + 1} d\alpha \quad (2a)$$

$$y(x) = \frac{Pa^3}{\pi EI} \int_0^{x/a} \int_0^{z/a} \int_0^\infty \frac{\alpha \cos(\alpha \xi)}{\alpha^3 + 1} d\alpha d\xi d\zeta \quad (2b)$$

where

$$a = [EI/E_f b]^{1/2}$$

E_f = Young's modulus for the foundation

b = one-half the width of the beam

α, ξ = variables of integration

These equations cannot be integrated in closed form but must be solved numerically. Biot calculated the moments in dimensionless form (M/Pa) and notes that the elementary theory will give the same moment under

the load point as the exact theory, if in the elementary theory K is taken as

$$K = 0.710 [b/a] E_f \quad (3)$$

The Biot theory cannot be solved for absolute deflections as these are infinite in common with most deflection problems in a semi-infinite body. However, it can be solved for relative displacements, and this has been done both by Biot in his paper and by JPL and The Franklin Institute on the JPL 1620 computer. The curves obtained from the Biot solution and from the elementary theory using Biot's value for K are plotted on Fig. 10. On these curves the ordinate, $w/[Pa^3/EI]$, is taken as zero at the load point and the abscissa is in dimensionless form (x/a). In this case w is the deflection of a point (x/a) measured from the deflected point under the load; y , as used

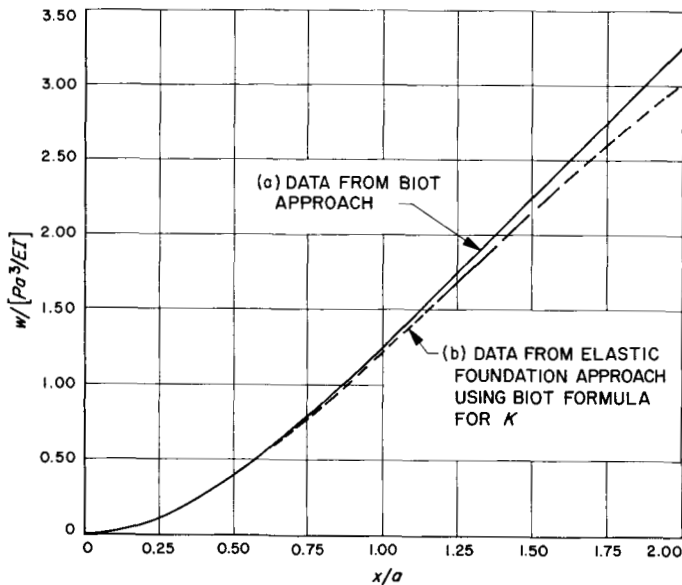


Fig. 10. Comparison of calculated deflections: (a) Biot's approach using theory of elasticity and Fourier integral for concentrated load, (b) beam on elastic foundation theory using K developed by Biot

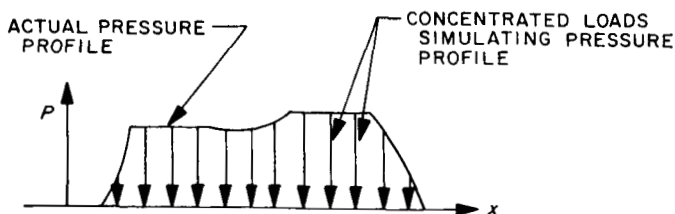


Fig. 11. Typical pressure distribution under hydrostatic bearing pad

previously, is absolute deflection. There is very good correlation in the vicinity of the load, with gradual deterioration as the distance from the load increases.

The actual pressure distribution under the hydrostatic bearing is continuous but not uniform. The deflections will be calculated by the superposition of a series of concentrated loads representing the actual continuous load as shown in Fig. 11. For this case, a more accurate representation of the true deflection curve than that obtained from the elementary theory, but without the complexity of Eq. (2b), is desirable. Several approaches are being considered:

- (1) Modifying the elementary solution in the form

$$\left[\frac{w}{Pa^3/EI} \right] = C_1 \left[1 - e^{-C_2(x/a)} \left(\cos \left[C_2 \left(\frac{x}{a} \right) \right] + \sin \left[C_2 \left(\frac{x}{a} \right) \right] \right) \right] \quad (4)$$

In this equation, w will be zero at the load point and C_1 and C_2 can be chosen to make the deflection curve match the character of the curve from the Biot theory at two selected points. For example, choosing $C_1 = 0.457$ and $C_2 = 0.668$ in Eq. (4) matches the absolute deflection at the load point to that obtained from the elementary solution and the relative deflection at $(x/a) = 1.5$ to that of the Biot theory. This result is given in Table 1, Column 1;

Table 1. Comparison of relative pad deflections using various methods of calculation

x/a	Column 1 ^a	Column 2 ^b	Column 3 ^c	Column 4 ^d	Column 5 ^e
0	0	0	0	0	0
0.25	0.01143	0.011153	0.01092	0.01079	0.01079
0.50	0.0406	0.039733	0.03868	0.03851	0.03868
0.75	0.0808	0.079683	0.07792	0.0774	0.07799
1.00	0.1325	0.126128	0.1243	0.1230	0.1243
1.25	0.1815	0.175159	0.1744	0.1700	0.1742
1.50	0.2252	0.223851	0.2253	0.2171	0.2253
1.75	0.2701	0.270701	0.2757	0.2620	0.2758
2.00	0.312	0.312643	0.3244	0.3030	0.3244
2.25		0.350497			

^a w calculated from modified elementary equation, JPL approach.

^b w calculated from modified elementary theory, Franklin Institute approach.

^c w calculated from polynomial.

^d w calculated from elementary theory with K evaluated by Biot method.

^e w calculated from exact theory.

it may be compared with the Biot theory solution, Table 1, Column 5.

- (2) V. Castelli of The Franklin Institute has proposed an evaluation of $C_1 = 0.472$ and $C_2 = 0.6484$ based on equal bending moment at the load point and equal relative displacement ($w/[Pa^3/EI]$) at $(x/a) = 1.5$ for the exact and the modified elementary solutions. Results of this calculation technique are shown in Table 1, Column 2.
- (3) The exact deflection curve can be matched at five selected points, for positive (x/a) values, with an eighth degree polynomial. Taking the points $(x/a) = 0, 0.5, 1.0, 1.5,$ and 2.0 the polynomial is

$$\left[\frac{Pa^3}{EI} \right] = 0.00206x^8 + 0.01778x^6 - 0.06002x^7 + 0.16861x^2 \quad (5)$$

Results of this calculation technique are shown in Table 1, Column 3.

Of the three methods, the polynomial gives the best match to the exact solution deflection curve for (x/a) ranging from 0 to 2.0. For (x/a) less than 1.0, the results from the elementary solution equation, using the method for evaluation K proposed by Biot, are satisfactory. (See Table 1, Column 4.)

3. The Structural Dynamics Problem in the Advanced Antenna System Design

a. Summary. We have been developing techniques for the analysis of the dynamics of the AAS and the other large antennas of the DSIF. Over the past year we have reported in this journal the tests and their interpretations of the dynamics of the 85- and 30-ft az-el antennas at Goldstone. In this issue we discuss the current state of our analysis techniques.

Background.

Purposes of dynamic analysis. The purposes of the structural dynamics analysis in the design of the AAS are twofold:

- (1) To provide a representative dynamic model of the system from which dynamic characteristics, in the form of transfer functions, can be obtained for use in the servo system design.
- (2) To provide an insight into the relationship of the structural configuration and detail design to the system dynamic characteristics, and a method of

analyzing changes in design to achieve an optimum structure.

The design process is one of repetition and refinement. The dynamic analysis serves as a means of communication between structural, mechanical, and servo design efforts during this process.

Servo requirements in structural dynamic analysis. The dynamic analysis model must display the motions of the antenna at points which are important in the servo system design. These include the driving points where commands or disturbances can enter the system, and pick-off points where position, rate, or acceleration indications are taken off.

The AAS is being designed to operate in three different modes, each using a different point for generating a position error signal. In addition, in each mode, motor rate signals will be used in inner servo loops, and motor accelerations may be used, depending on the final servo system design. The three operating modes are:

- (1) RF auto track mode, in which the antenna position error is generated by a simultaneous lobing antenna feed and an angle tracking receiver. In the auto track mode the master equatorial is slaved to the reflector structure giving precision position read-outs in ha-dec coordinates.
- (2) A precision pointing mode in which the antenna position error is generated in an optical link between the antenna intermediate reference surface and an independent master equatorial system. The master equatorial moves in ha-dec coordinates and provides a precise pointing command for the antenna. The intermediate reference surface is mounted on the antenna reflector structure and is a best representation of the RF beam position. The dynamic model must define the intermediate reference surface position.
- (3) A low-accuracy analog steering mode in which the antenna position is taken from the final drive gears and compared with an analog command signal to generate a position error signal.

The torque input points include the azimuth and elevation drives and the wind loads on the structure. The drive inputs are taken as the servo-valve flow rates while the wind load must be reduced to forces acting on specified points in the structural systems. The dynamic analysis must produce transfer functions from the drive points to the various pick-off points.

Wind and motion conditions require a servo bandwidth of about 0.2 cps for the AAS, and a basic system requirement is that driving forces within this bandwidth must not excite the structural resonances. Structural resonant frequencies under 1.0 cps are of very serious concern; frequencies over perhaps 3 cps are of little consequence to the servo design. Accordingly, the essential dynamic analysis should predict the lower frequencies with good accuracy, while the higher frequencies may be ignored.

Structural dynamics influence in structural design. Three requirements which the final antenna structure must meet are:

- (1) The reflector structure must be sufficiently stiff to maintain surface accuracy in the operational winds at all attitudes.
- (2) The supporting structure must be sufficiently stiff to support a reflector of the required weight with lowest natural frequencies compatible with the necessary pointing accuracy.
- (3) The over-all structure must be reasonably economical.

The structure dynamic analysis helps to meet these requirements in the design phase by determining the natural frequencies for a particular design, identifying areas of weakness which require design rework, and providing a relatively direct method of approaching an optimum design by studying parameter variations.

To be useful in the design effort the dynamic analysis must be carried out in sufficient detail to be sure that all of the problems are included in the model. A model involving only 4 or 5 deg of freedom is not likely to show the system in enough detail to assure that potential problems are identified; an analysis of all the detail of the structure would be excessively expensive.

b. Present work. The method described below is being applied to the AAS analysis because the information required to use it is practically obtainable, and the transfer functions desired for the servo design can be produced directly.

For purposes of analysis, the structure is divided into a lower part, including the pedestal, alidade, and drives, and an upper part including all of the parts which move in elevation. The lower part is represented by a lumped mass system, with mass points for the pedestal, the bottom of the alidade, and the top of the alidade. The struc-

ture falls naturally into this grouping, and the necessary stiffnesses and masses are easily calculated.

The upper part is represented by the generalized masses and stiffnesses obtained from the JPL Stiff-Eig Program. By taking advantage of the symmetry about a vertical plane through the reflector axis, and assuming symmetry about the plane containing the reflector and elevation axes, the structure can be analyzed in quarters with symmetric and antisymmetric boundaries. There are four possible combinations of boundaries as shown in Fig. 10. The two combinations with symmetry about the vertical axis relate to elevation motion and the two with antisymmetric boundaries relate to azimuth motion. For the present, the azimuth and elevation models are considered to be independent.

The Stiff-Eig Program produces generalized stiffness and mass matrices and model columns for the lowest six frequencies of the structure analyzed. The four boundary combinations analyzed yield data based on 24 resonant frequencies of which 12 apply to the azimuth model and 12 to the elevation model.

The Stiff-Eig output data of interest is as follows:

$[\phi_{ur}]$ = matrix of r modal columns defining u points in the structure.

$[M_r]$ = generalized mass matrix of order r , defined by the relationship

$$[M_r] = [\phi_{ur}]^T [M] [\phi_{ur}] \quad (1)$$

$[M]$ = mass matrix in inertial coordinates;

$[K_r]$ = generalized stiffness matrix of order r , defined by the relationship

$$[K_r] = [\phi_{ur}]^T [K] [\phi_{ur}] \quad (2)$$

where $[K]$ = stiffness matrix in inertial coordinates, and the superscript T defines the transpose of the matrix. The inertial coordinates and the generalized coordinates are related by the equation

$$\{y_u\} = [\phi_{ur}] \{p_r\} \quad (3)$$

where p_r is the amplitude of the r th mode and y_u is the displacement of the u th point.

$[K_{cu}]$ = matrix formed by the reactions at the constrained points c , due to a unit displacement at the u th unrestrained point with the other normally free points restrained.

To combine the lower part in inertial coordinates with the upper part in generalized coordinates, we assume for the moment that we can write the equations for the entire system in inertial coordinates in the form

$$\begin{bmatrix} A & B & 0 \\ B^T & C & D \\ 0 & D^T & E \end{bmatrix} \begin{Bmatrix} y_i \\ y_c \\ y_u \end{Bmatrix} = \{0\} \quad (4)$$

in which

[A] is the dynamic matrix of the lower system with the displacements y_c constrained

[B] is the matrix of the stiffness coefficients formed by the reactions on points i due to unit displacements of individual points c while the other points c are restrained

$[B]^T$ is the transpose of [B]

[C] is the dynamic matrix of the masses with displacements common to the upper and lower systems, with the normally unrestrained displacements in these system restrained

[D] is the matrix formed by the reactions at the constrained points c due to a unit displacement at the u th unrestrained point, with the other normally free points also restrained. This is $[K_{cu}]$ obtained from the Stiff-Eig Program.

y_i is the i th unrestrained displacement of the lower part

y_c is the displacement of the points c common to the upper and lower parts and considered restrained in the analysis of the upper part

y_u as before, is the displacement of the u th unrestrained point in the upper part

Expanding Eq. (4) gives

$$[A] \{y_i\} + [B] \{y_c\} = \{0\} \quad (5a)$$

which represents the equilibrium equations for the unrestrained masses of the lower part,

$$[B]^T \{y_i\} + [C] \{y_c\} + [D] \{y_u\} = \{0\} \quad (5b)$$

which represents the equilibrium equations for the masses at the points connecting the upper and lower parts, and

$$[D]^T \{y_c\} + [E] \{y_u\} = \{0\} \quad (5c)$$

which represents the equilibrium equations of the unrestrained mass points in the upper part.

The matrices A, B, B^T and C are obtained by the conventional methods of writing equilibrium equations for lumped mass systems. D is the matrix obtained from the Stiff-Eig Program as $[K_{cu}]$ and must also be reflected when constructing C. E is at the moment not attainable and because of the complexity of the backup and reflector structure would be of very high order.

A transformation of Eq. (4) is now constructed based on Eqs. (1), (2), and (3). It is noted that if E could be written it would be of the form

$$[[M] s^2 + [K]] \{\bar{y}_u\} = \{0\} \quad (6)$$

where s is the LaPlace operator, based on restraints at the common coordinates y_c . Replacing $\{y_u\}$ by $[\phi_{ur}] \{p_r\}$, and premultiplying by $[\phi_{ur}]^T$ gives

$$[\phi_{ur}]^T [[M] s^2 + [K]] [\phi_{ur}] \{\bar{p}_r\} = \{0\} \quad (7)$$

and

$$[s^2 \bar{M}_r] + [\bar{K}_r] \{\bar{p}_r\} = \{0\} \quad (8)$$

This is the generalized form in which the Stiff-Eig results are given. To accomplish this transformation within Eq. (4), we pre- and post-multiply Eq. (4) as follows:

$$\begin{bmatrix} I & 0 & 0 \\ 0 & I & 0 \\ 0 & 0 & \phi_{ur}^T \end{bmatrix} \begin{bmatrix} A & B & 0 \\ B^T & C & D \\ 0 & D^T & E \end{bmatrix} \begin{bmatrix} I & 0 & 0 \\ 0 & I & 0 \\ 0 & 0 & \phi_{ur} \end{bmatrix} \begin{Bmatrix} \bar{y}_i \\ \bar{y}_c \\ \bar{p}_r \end{Bmatrix} = \{0\} \quad (9)$$

giving

$$\begin{bmatrix} A & B & 0 \\ B^T & C & D \\ 0 & D^T & E' \end{bmatrix} \begin{Bmatrix} \bar{y}_i \\ \bar{y}_c \\ \bar{p}_r \end{Bmatrix} = \{0\} \quad (10)$$

where

$$[D'] = [K_{cu}] [\phi_{ur}] \quad (11a)$$

$$[E'] = [\phi_{ur}]^T [E] [\phi_{ur}] \quad (11b)$$

E' is obtainable from the Stiff-Eig Program in the form

$$[E'] = [M_r] s^2 + [K_r] \quad (12)$$

For forcing functions, F_i , applied on the drives in the lower part, the following nonhomogeneous equation pertains

$$\begin{bmatrix} A & B & 0 \\ B^T & C & D' \\ 0 & D'^T & E' \end{bmatrix} \begin{Bmatrix} y_i \\ y_c \\ p_r \end{Bmatrix} = \begin{Bmatrix} F_i \\ 0 \\ 0 \end{Bmatrix} \quad (13)$$

Eq. (13) can be solved for transfer functions to points on the lower structure or to modal amplitudes, p_r by Cramer's rule in the form

$$\frac{\bar{p}_r(s)}{\bar{F}(s)} \text{ or } \frac{\bar{y}_i(s)}{\bar{F}(s)} = K \frac{\prod_j (s^2 + z_j^2)}{\prod_k (s^2 + p_k^2)} \quad (14)$$

where z_j and p_k are the zeros and poles of the transfer function.

Transfer functions to displacements y_u , on the tipping parts, can be obtained by building up y_u from the mode shapes ϕ_{ur} and the modal amplitudes p_r using Eq. (3) re-expressed for a particular y_u as

$$y_u = \sum_r \phi_{ur} p_r.$$

Combining this with Eq. (14) gives

$$\frac{\bar{y}_u(s)}{\bar{F}(s)} = \sum_r \frac{\phi_{ur} [\prod_j (s^2 + z_j^2)]_r}{[\prod_k (s^2 + p_k^2)]} \quad (14a)$$

It is noted that the denominators for each p_r or y_u [Eqs. (14) and (14a)] are identical. The numerator of (14a) can be expanded into a single polynomial which can be factored to give the transfer function zeros. The transfer function to y_u then is

$$\frac{\bar{y}_u(s)}{\bar{F}(s)} = \frac{\prod_m (s^2 + z_m^2)}{\prod_k (s^2 + p_k^2)} \quad (14b)$$

In an alternate approach, we choose r points of interest, where r is the number of modes considered necessary to define the motions of the upper part. The modal matrix $\{y_u\}$ is then shortened to $\{y_r\}$ and Eq. (3) becomes

$$\{y_r\} = [\phi_{rr}] \{p_r\} \quad (15)$$

and hence

$$\{p_r\} = [\phi_{rr}]^{-1} \{y_r\} \quad (16)$$

$[\phi_{rr}]$, being square, can be inverted.

Eq. (13) is now operated on to eliminate the $\{p_r\}$ coordinates by retracing the steps of Eq. (9) in the form

$$\begin{bmatrix} I & 0 & 0 \\ 0 & I & 0 \\ 0 & 0 & [\phi_{rr}^{-1}]^T \end{bmatrix} \begin{bmatrix} A & B & 0 \\ B^T & C & D' \\ 0 & D'^T & E' \end{bmatrix} \begin{bmatrix} I & 0 & 0 \\ 0 & I & 0 \\ 0 & 0 & \phi_{rr}^{-1} \end{bmatrix} \begin{Bmatrix} y_i \\ y_c \\ y_r \end{Bmatrix} = \begin{Bmatrix} F_i \\ 0 \\ 0 \end{Bmatrix} \quad (17)$$

giving

$$\begin{bmatrix} A & B & 0 \\ B^T & C & D'' \\ 0 & D''^T & E'' \end{bmatrix} \begin{Bmatrix} y_i \\ y_c \\ y_r \end{Bmatrix} = \begin{Bmatrix} F_i \\ 0 \\ 0 \end{Bmatrix} \quad (18)$$

where

$$[D''] = [K_{cu}] [\phi_{ur}] [\phi_{rr}]^{-1} \quad (19a)$$

$$[E''] = [\phi_{rr}^{-1}]^T [E'] [\phi_{rr}]^{-1} \quad (19b)$$

Eq. (18) is now of a reasonable order (perhaps 20); its components are all available, and it can be solved for any of the transfer functions of interest in the form

$$\frac{\bar{y}_i(s)}{\bar{F}(s)} = \frac{K \prod_m (s^2 + z_m^2)}{\prod_n (s^2 + p_n^2)} \quad (21)$$

The required structural information is available from the modal columns of Eq. (18) for the lower structure and from the Stiff-Eig modal columns for the upper structure.

The necessary mechanization for carrying out the solution is now being developed. Test cases for relatively simple systems are being run.

In addition, a simplified version of a method of combining several systems in generalized coordinates by requiring compatibility at the connecting points is being considered. This approach was developed for the JPL Structure and Mechanics Division by Professor Hurty of U.C.L.A. for application to analysis of spacecraft structures and is now being programmed for computer calculation in a most general form. For application to the antenna problem, a reduced and specialized program may be practical.

References

1. Newell, J. S., "The Use of Symmetric and Anti-Symmetric Loadings," *IAS Journal*, p. 235, 1939.
2. Hetenyi, M., "Beams on Elastic Foundation," p. 15, University of Michigan Press.
3. Biot, M. A., "Bending of an Infinite Beam on an Elastic Foundation," *Transactions of the American Society of Mechanical Engineers*, 59, A1-7, March 1937.